Astroteilchenphysik

Search for Relativistic Magnetic Monopoles with the IceCube 40-String Detector

DISSERTATION

zur Erlangung des Doktorgrades
doctor rerum naturalium
(Dr. rer. nat.)

Bergische · Universität · Wuppertal · 1972 ·

Fachbereich C – Mathematik und Naturwissenschaften

Der Fachgruppe Physik vorgelegt von

Jonas Posselt

im

Oktober 2013

Die Dissertation kann wie folgt zitiert werden:

urn:nbn:de:hbz:468-20131212-124903-6
[http://nbn-resolving.de/urn/resolver.pl?urn=urn%3Anbn%3Ade%3Ahbz%3A468-20131212-124903-6]

Contents

List of Figures

List of Tables

Abbreviations

ADC	Analog Digital Converter
AHA	Additionally Heterogeneous Absorption
AMANDA	Antarctic Muon and Neutrino Detector Array
ATWD	Analog Transient Waveform Digitizer
CORSIKA	Cosmic Ray Simulations for Kascade
CR	Cosmic Ray
DAQ	Data Acquisition
DOM	Digital Optical Module
DOM MB	DOM Mainboard
DOR	DOM Readout
DSB	DOMHub Service Board
EHE	Extremely High Energy
FPGA	Field-Programmable Gate Array
GPS	Global Positioning System
GUT	Grand Unified Theories
HC DOM	High Charge DOM
HLC	Hard Local Coincidence
HLD	High Light Density
HV	High Voltage
IC22	22-string IceCube Detector
IC40	40-string IceCube Detector
ICL	IceCube Laboratory
LD	Light Density
LF	LineFit
LLD	Low Light Density
MACRO	Monopole Astrophysics and Cosmic Ray Observatory
MChit	Monte Carlo hit
MMC	Muon Monte Carlo

MPE	Multi Photo-Electron
MRF	Model Rejection Factor
MRP	Model Rejection Potential
NC/CC	Neutral/Charged Current
Nch	Number of DOMs (Channels)
NHF	No-Hit Fraction
NPE	Number of Photo-Electrons
PDF	Probability Density Function
PE	Photo-Electron
PMF	Probability Mass Function
PMT	Photomultiplier Tube
PORTIA	PORTable Impulse Analyzer
RAPcal	Active Pulsing Calibration
SLC	Soft Local Coincidence
SMT	Simple Majority Trigger
SPE	Single Photo-Electron
SPICE	South Pole Ice
SQUID	Superconducting Quantum Interference Device
SSB	Spontaneous Symmetry Breaking
ULEE	Ultra Low Energy Event
UTC	Coordinated Universal Time

1 Introduction

The knowledge of magnetism dates back at least several thousand years, but for the most part of history remained without a theory to explain its behavior and was often confused with static electricity. The first recorded observation of a magnetic phenomenon is attributed to Thales of Miletus (625 BC - 547 BC), who described the attraction of iron to loadstone [1]. However, it was not until 1600 when William Gilbert published the first investigation of magnetism, which can be called scientific in a modern sense [2]. The basic laws of electricity and magnetism were not discovered until the 19^{th} century. These laws were ultimately combined into a unified theory [3, 4], which is now called classical electrodynamics.

A striking feature of the laws of classical electrodynamics is the absence of isolated *magnetic charges*. However, this is based on empirical observations showing that isolated electric charges in nature, whereas magnetic charges are only observed as dipoles. There is no obvious intrinsic reason for this asymmetry since the fundamental equations of the theory could easily accommodate magnetic charges. In fact, the theory would even become invariant under a duality transformation exchanging electric and magnetic quantities. Magnetic charge could also be carried by real particles analog to electrically charged particles. The first to openly hypothesize the existence of such magnetic monopoles was Pierre Curie in 1894 [5].

In 1931 Paul Dirac proved that magnetic monopoles are consistent with quantum mechanics if both electric and magnetic charge are quantized [6]. By that time no other theoretical explanation for the observed quantization of electric charge was known. Hence magnetic monopoles offered an elegant solution. An alternative explanation for the charge quantization was discovered in 1974 with the concept of unified gauge theories. If the gauge group of electromagnetism is embedded in a non-abelian gauge group, then charge quantization follows for group theoretic reasons [7, 8]. However, the necessary conditions to have a quantized electric charge are also sufficient for the existence of magnetic monopoles, which are therefore mandatory in such a theory.

The properties of these monopoles are unique and calculable for a given unification model, but may vary significantly between models. Most models predict the monopole mass to be extremely large, though. This leaves them beyond the creation and detection capabilities of any existing or foreseeable particle accelerator[1]. While this may seem discouraging for experimental physicists, the early universe provided enough energy to create magnetic monopoles in abundance. Since monopoles are predicted to be stable due to topological reasons, some should have survived until the present.

So far, no experimental proof for the existence of magnetic monopoles has been found. Current constraints on the monopole flux are of the order 10^{-16} $\mathrm{cm}^{-2}\mathrm{sr}^{-1}\mathrm{s}^{-1}$ or lower (see Section 2.6). Therefore extremely large detectors are required to either detect a monopole or improve existing flux limits. The IceCube neutrino observatory is such a detector. IceCube was constructed as a Cherenkov telescope to detect the faint light from relativistic particles like neutrino-induced muons, utilizing the large volume of natural glacial ice at the South Pole. Magnetic monopoles could be detected by IceCube if their velocity exceeds the Cherenkov threshold of ice or if secondary particles, produced by monopole-matter interactions, are energetic enough to emit Cherenkov radiation.

This thesis concerns the search for relativistic magnetic monopoles using data taken in 2008/2009 with the partially completed IceCube detector. The outline of this work is as follows: Chapter 2 provides the theoretical background of magnetic monopoles and their interaction with with matter. Chapter 3 introduces the IceCube detector, followed by a description of the signatures of both signal and background events in Chapter 4. In Chapter 5 an overview of the simulated data used for the analysis and its generation is given. Chapters 6 and 7 then summarize the variables and cut conditions applied in the analysis. Systematic uncertainties are discussed in Chapter 8. The final results are presented in Chapter 9 followed by some concluding remarks in Chapter 10.

---

[1] Alternate theories may allow monopoles to appear in a mass range accessible to accelerators. See for example the MoEDAL experiment [9] at the Large Hadron Collider

2 Magnetic Monopoles

Magnetic Monopoles are hypothetical particles that carry a magnetic charge, i.e. they appear as isolated magnets with only one pole. Though such monopoles have never been observed, they are consistent with our current knowledge of particle physics. Many theories that go beyond the Standard Model like Grand Unification, Kaluza-Klein or String theories even predict the existence of magnetic monopoles [10, 11]. This chapter briefly summarizes the theoretical description of magnetic monopoles as well as their creation and interaction with conventional matter loosely guided by its historical development. Formulas in these sections are in Gaussian CGS units unless noted otherwise. Finally an overview of current limits on the monopole flux is given.

2.1 Monopoles in Classical Electrodynamics

The fundamental quantities of classical electrodynamic are the electric and magnetic fields $\vec{E}$ and $\vec{B}$. Interaction and generation of these fields are described by Maxwell's equations [3, 4]. In the presence of matter the differential form of Maxwell's equations is given by [12]

$$\vec{\nabla} \cdot \vec{D} = 4\pi\rho_e \tag{2.1a}$$

$$\vec{\nabla} \cdot \vec{B} = 0 \tag{2.1b}$$

$$\vec{\nabla} \times \vec{H} - \frac{1}{c}\frac{\partial \vec{D}}{\partial t} = \frac{4\pi}{c}\vec{j}_e \tag{2.1c}$$

$$-\vec{\nabla} \times \vec{E} - \frac{1}{c}\frac{\partial \vec{B}}{\partial t} = \vec{0}. \tag{2.1d}$$

where ρ_e and $\vec{j}_e$ are the electric charge and current densities and c is the speed of light in vacuum. The fields $\vec{D}$ and $\vec{H}$ are defined by

$$\vec{D} = \epsilon\vec{E} \text{ and } \vec{B} = \mu\vec{H}, \tag{2.2}$$

with ϵ and μ being the permittivity and permeability of the medium.

Many electromagnetic quantities are symmetric in electric and magnetic fields, e.g. the electromagnetic energy density $u \propto \vec{E} \cdot \vec{D} + \vec{B} \cdot \vec{H}$ [13]. However, Maxwell's equations contain only electrical source terms. This striking asymmetry is by definition since neither magnetic monopoles nor magnetic currents have ever been observed in nature. Substituting Equations (2.1b) and (2.1d) with [14]

$$\vec{\nabla} \cdot \vec{B} = 4\pi\rho_m \tag{2.3}$$

$$-\vec{\nabla} \times \vec{E} - \frac{1}{c}\frac{\partial \vec{B}}{\partial t} = \frac{4\pi}{c}\vec{j}_m, \tag{2.4}$$

where ρ_m and $\vec{j}_m$ denote the magnetic charge and current densities, cancels the asymmetry. These generalized Maxwell's equations are invariant under the duality transformation [15]

$$\begin{gathered}\left(\vec{E},\vec{H}\right) \longmapsto \left(\vec{H},-\vec{E}\right),\ \left(\vec{D},\vec{B}\right) \longmapsto \left(\vec{B},-\vec{D}\right)\\ (\rho_e,\rho_m) \longmapsto (\rho_m,-\rho_e),\ \left(\vec{j}_e,\vec{j}_m\right) \longmapsto \left(\vec{j}_m,-\vec{j}_e\right)\\ (\epsilon,\mu) \longmapsto (\mu,\epsilon)\,.\end{gathered} \tag{2.5}$$

The generalized Lorentz force for particles with electric charge q_e, magnetic charge q_m and velocity $\vec{v}$ takes the form [14]

$$\vec{F} = q_e\left(\vec{E} + \frac{\vec{v}}{c} \times \vec{B}\right) + q_m\left(\vec{B} - \frac{\vec{v}}{c} \times \vec{E}\right). \tag{2.6}$$

While classical electrodynamics can be easily adapted to include magnetic monopoles, it allows no inference about their nature. For symmetry reasons the fields generated by electric and magnetic charges would look very similar [16]. A static magnetic charge located at the origin would give rise to a typical radial field with $1/r^2$ dependency:

$$\vec{B} = q_m\frac{\vec{e_r}}{r^2}, \tag{2.7}$$

with $\vec{e_r}$ being the radial unit vector. A magnetic charge moving with velocity $\vec{v}$ would also induce an electric field of the form

$$\vec{E} = q_m\frac{\vec{v} \times \vec{e_r}}{r^2}. \tag{2.8}$$

This symmetry has the convenient effect that the descriptions of electromagnetic phenomena remain largely form-invariant when magnetic instead of electric charges are considered. An illustration of the field configurations generated by electric and magnetic monopoles is shown in Figure 2.1.

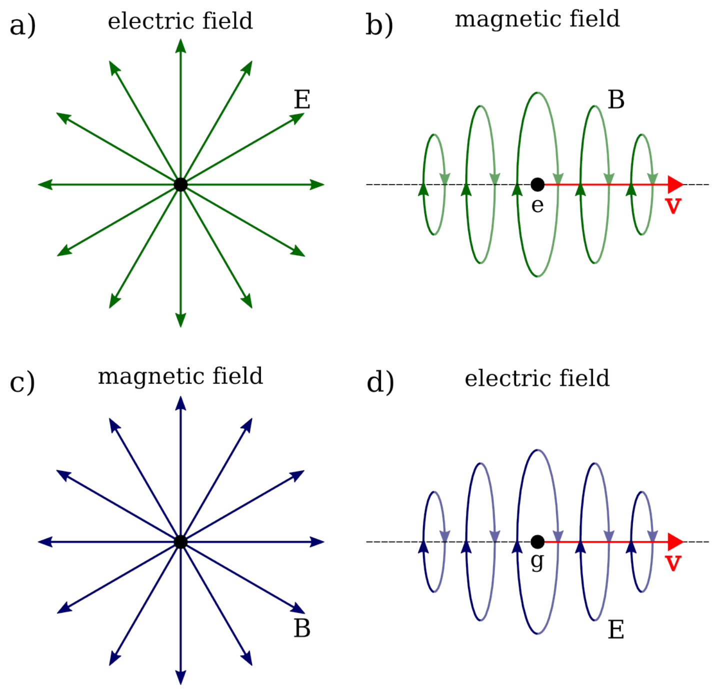

Figure 2.1: The electromagnetic fields generated by electric and magnetic monopoles. An electric monopole has a static, radial electric field E (a) and induces a circular magnetic field B when in motion (b). For magnetic monopoles the field configuration (c and d) is the same with the exception that E and B have been interchanged.

2.2 The Dirac Monopole

In quantum theory the electromagnetic interaction is described by the scalar potential ϕ and the vector potential $\vec{A}$, which are connected to the fields by [17]

$$\vec{E} = -\vec{\nabla}\phi - \frac{\partial \vec{A}}{\partial t} \tag{2.9}$$

$$\vec{B} = \vec{\nabla} \times \vec{A}. \tag{2.10}$$

Phenomena like the Aharonov-Bohm effect [18] show that these potentials are not just mathematical tools but have physical meaning. However, Equation (2.10) yields the identity $\vec{\nabla} \cdot \vec{B} = 0$, in contradiction with Equation (2.3) and the notion of magnetic monopoles.

In 1931 Dirac argued that this contradiction can be avoided if a monopole is envisioned as the end of an infinitesimally thin solenoid extending to infinity [6], as illustrated in Figure 2.2. The magnetic flux of this solenoid, called Dirac string, would ensure validity of Maxwell's equations, whereas the configuration would classically appear like an isolated magnetic charge. The vector potential for such a configuration is well defined everywhere except at the position of the string. In order for this line singularity to be invisible, e.g. in an Aharonov-Bohm like experiment, Dirac derived the condition [19]

$$q_e q_m = N\frac{\hbar c}{2},\, N \in \mathbb{Z}. \tag{2.11}$$

An alternate monopole theory [20, 21] which avoids the use of potentials with line singularities was shown to be equivalent to Dirac's theory [22].

Equation (2.11) implies that if at least one magnetic monopole exists in the universe all electric and magnetic charge must be quantized. Since quantum theory offers no explanation for the observed charge quantization, this is seen as one of the most attractive features of Dirac's monopole theory. The elementary magnetic charge g_D (Dirac charge) can be derived by substituting q_e in (2.11) with the elementary electric charge e:

$$g_D = \min(q_m) = \frac{e}{2\alpha} \approx 68.5e, \tag{2.12}$$

with $N = 1$ and $\alpha = e^2/\hbar c$ the fine structure constant.

While Dirac's monopole is consistent with quantum mechanics, magnetic charge is still inserted into the theory *by hand*. Consequently, many physical quantities of a monopole, like its mass, remain free parameters within this theory.

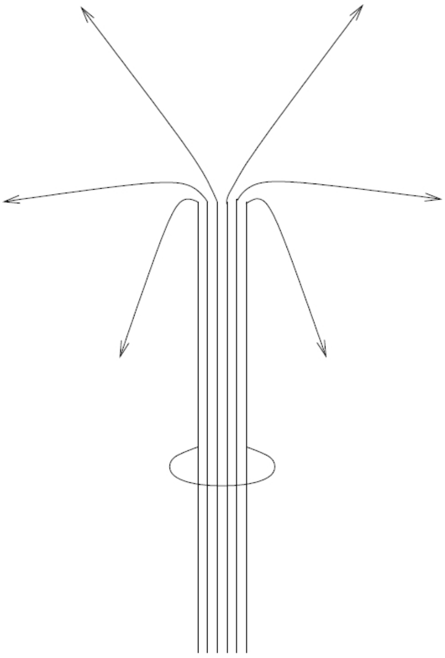

Figure 2.2: Magnetic field lines at the end of a semi infinite solenoid [10]. The solenoid is undetectable in an Aharonov Bohm like experiment, if Dirac's quantization condition is fulfilled.

2.3 The 't Hooft/Polyakov Monopole

In 1974 't Hooft and Polyakov discovered that the existence of magnetic monopoles follows from general principles in theories that unify the fundamental interactions (except gravity) [23, 24]. Such a Grand Unified Theory (GUT) [8, 25] is defined by a simple non-abelian gauge group G with only one coupling constant. Below a certain energy scale Λ_{GUT} the gauge group is spontaneously broken to that of the Standard Model of particle physics [26]:

$$G \longrightarrow H_{\mathrm{n}} \longrightarrow \ldots \longrightarrow H_1 \longrightarrow H_0 \tag{2.13}$$

with

$$\begin{aligned} H_1 &= \mathrm{SU}(3)_{\mathrm{color}} \otimes [\mathrm{SU}(2) \otimes \mathrm{U}(1)]_{\mathrm{electroweak}} \\ H_0 &= \mathrm{SU}(3) \otimes \mathrm{U}(1)_{\mathrm{EM}}. \end{aligned}$$

This ensures that the electromagnetic $\mathrm{U}(1)_{\mathrm{EM}}$ gauge group is compact resulting in a quantized electric charge. However, a (compact) U(1) appearing as a subgroup of a larger non-abelian gauge group is sufficient for the existence of magnetic monopoles [16]. Hence, magnetic monopoles are a generic prediction of grand unification. They appear as topological solitons, i.e. stable finite energy solutions of the field equations, which behave like particles in the classical theory.

GUT monopoles have a complicated inner structure as illustrated in Figure 2.3. In the central region, with a radius of order $\hbar c \Lambda_{\mathsf{GUT}}^{-1}$, the vacuum respects the full symmetry of the unified gauge group G (false vacuum). Outside this region, where the *true* vacuum is approached asymptotically, are shell like clouds of virtual gauge bosons and elementary particles. The radial magnetic field of the monopole solution arises from the configuration of the gauge field with no need to introduce magnetic charge *by hand*. The stability of this configuration and therefore the conservation of magnetic charge follows from a topological argument [26] (see Section 2.4.1). Curiously, this topological conservation law is quite different from electric charge conservation, which follows from Noether's theorem [28]. Also remarkably is that the GUT monopole charge is quantized exactly as demanded by Dirac's quantization condition (2.11).

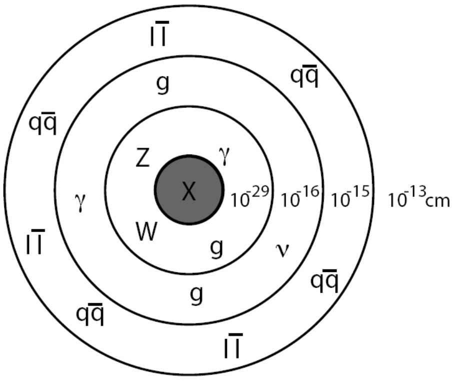

Figure 2.3: Schematic structure of a GUT monopole [27]. The central region with radius $\hbar c \Lambda_{\mathsf{GUT}}^{-1}$ ($\mathcal{O}(10^{-29})$ cm for most GUT models) contains a GUT symmetric vacuum (labeled X).

The properties, like mass and charge, of a GUT monopole are unique and calculable for a given GUT model. Exact values may vary significantly between different models. The monopole mass M is related to the unification energy scale by

$$Mc^2 \gtrsim \frac{\Lambda_{\mathsf{GUT}}}{\alpha_{\mathsf{GUT}}}, \tag{2.14}$$

Model	Mass [GeV/c^2]	Charge	Ref.
SU(5)	10^{17}	g_D	[29, 30]
SO(10)	$> 10^{16}$ and $10^{10} - 10^{16}$	g_D and $2g_D$	[31, 10]
SU(15)	10^8	n/s	[32, 33, 34]
Superstring	10^{16}	$3g_D$	[35]
SUSY	$\geq 10^7$	$\geq 2g_D$	[36, 37]

Table 2.1: Monopole masses for several GUT models

where α_{GUT} is the running coupling constant renormalized at the energy scale Λ_{GUT} [10]. An overview of some GUT models and their predicted monopole mass is given in Table 2.1. In general, GUT monopoles are too heavy to be produced in any existing or foreseeable accelerator. Only the extremely hot universe, shortly after the *Big Bang*, may have provided enough energy to produce monopoles in significant numbers.

2.4 Creation and Acceleration

2.4.1 Monopole Creation in the early Universe

In Grand Unification the original gauge symmetry is restored at temperatures exceeding the unification energy scale Λ_{GUT}. According to the hot Big Bang theory this condition must have been fulfilled at some time in the early universe [38]. While expanding and cooling, the Universe undergoes a series of phase transitions, associated with the GUT Higgs field ϕ, spontaneously breaking the GUT symmetry.

If ϕ has at least three components, monopoles can be produced in two ways: 1.) as monopole-antimonopole pairs in energetic particle collisions; 2.) as topological defects through the Kibble mechanism [39] during the spontaneous symmetry breaking (SSB). SSB is driven by ϕ acquiring a non-zero vacuum expectation value $\langle\phi\rangle$, given by the minimum of the potential $V(\phi)$. Since this minimum is degenerated, causally disconnected domains are expected to take on different vacuum configurations during a phase transition. These domains grow with further evolution of the Universe and eventually come in contact. The vacuum configuration of the Higgs field will tend to interpolate between two domains, which are in

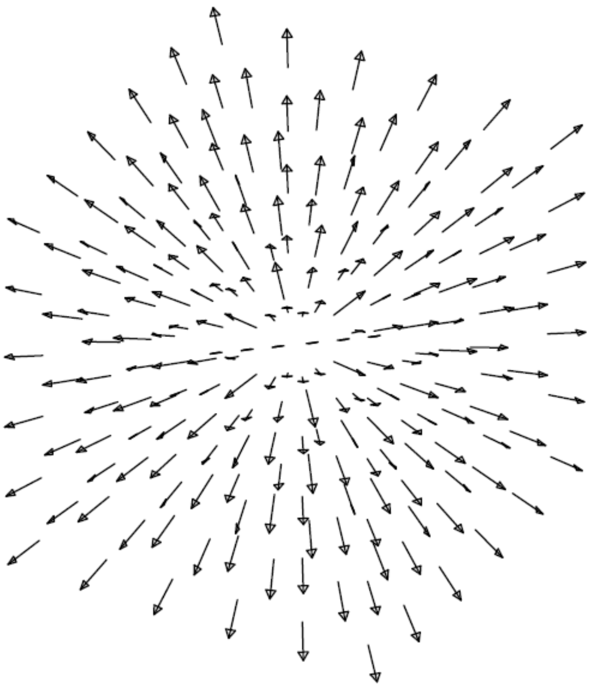

Figure 2.4: The hedgehog configuration of the Higgs field in the 't Hooft-Polyakov monopole solution. This configuration cannot be turned continuously into the uniform vacuum state, so it is topologically stable. Since the field must be continuous, it cannot be in the vacuum state at the origin. Instead there is a localized lump of energy (in other words, a particle) at the origin. From [16].

contact. When several domains coalesce, the field can form a hedgehog configuration (see Figure 2.4). This configuration is stable since it can not be continuously deformed into an arbitrary vacuum state [2] [16]. Figure 2.5 illustrates the process for a two component Higgs field. If the unbroken symmetry is spherical and the broken symmetry contains an U(1) subgroup (see Eq. 2.13), such configurations appear as magnetic monopoles. Many GUT models with an 4-dimensional Higgs field also predict the existence of *dyons*, particles with both electric and magnetic charge, besides magnetic monopoles [40].

The number of magnetic monopoles created from direct pair production

---

[2] i.e. the manifold of the ϕ states that minimize $V(\phi)$ is not simply connected.

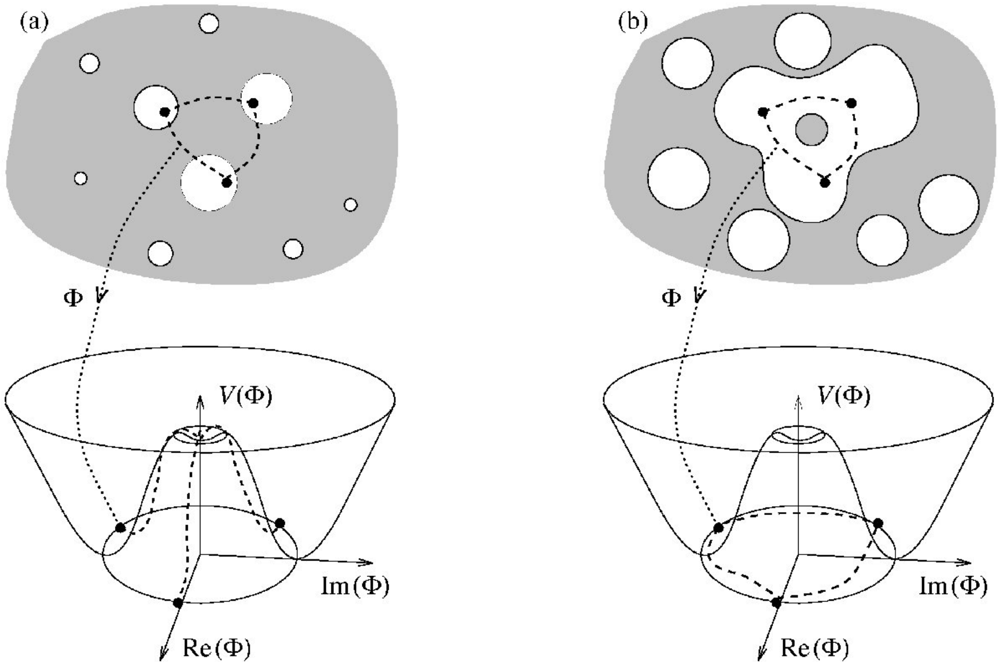

Figure 2.5: Formation of topological defects through the Kibble mechanism [41]. At a phase transition bubbles of the new phase form where the Higgs field has a non zero vacuum expectation value (a). As the bubbles grow they collide and merge (b). If the expectation values of the merging bubbles are widely distributed around the vacuum manifold a topological defect forms.

is intrinsically small because monopoles can not exist until SSB occurs and their mass is large compared to average thermal energy at that time [42]. The Kibble mechanism, on the other hand, predicts roughly one monopole to be produced per causal domain. The resulting monopole mass density exceeds the observed mass density of the Universe by several orders of magnitude [43]. This contradiction is referred to as the *monopole problem.* Several possible solutions have been suggested [44]. An attractive and widely accepted one is the inflation scenario. It assumes the early Universe experienced an inflationary phase, i.e. a phase of exponential expansion. This would dilute the monopole density to an acceptable value. Unfortunately, predictions from this scenario are not firm, ranging from less than one monopole in the observable Universe [42] to fluxes close to current limits [45, 46, 47]. Therefore the monopole problem is still missing a conclusive explanation.

2.4.2 Acceleration Mechanisms

As relics of the early universe, magnetic monopoles are expected to have a negligible velocity dispersion and their velocity relative to us should be $\mathcal{O}(10^{-3})$c due to the orbital velocity of the sun in our galaxy. However, monopoles can gain additional kinetic energy through acceleration in gravitational and magnetic fields. Due to their large mass, the gravitational acceleration of monopoles is limited to velocities of about 10^{-2}c [48].

The acceleration of magnetic monopoles along magnetic field lines follows from the generalized Lorentz force law (see Eq. (2.6)) and is analog to the acceleration of electric charges in electric fields. The kinetic energy gained by a monopole of charge g traversing a magnetic field B with coherence length L is [49]

$$E_{\text{kin}} = g \int\limits_{\text{path}} \vec{B} \cdot d\vec{\ell} \sim gBL. \tag{2.15}$$

In the magnetic field of our galaxy for instance with $B \approx 3 \cdot 10^{-6}$ G and $L \approx 300$ pc a monopole with one Dirac charge can gain up to $6 \cdot 10^{10}$ GeV. Table 2.2 list the properties of the magnetic field of several cosmic environments, which act as monopole accelerators. Also listed is the kinetic energy a minimally charged magnetic monopole gains in a single transit through such an environment. The largest energies, about 10^{15} GeV, are typically obtained in fields with the longest coherence length. Additionally, a relic monopole should encounter several of these environments during the lifetime of the Universe, allowing even higher energies. This can be approximated by an additional factor $\sqrt{n}$ in (2.15), where $n \approx 100$ is the number of traversed domains in a random walk [49]. Hence, monopoles with masses up to 10^{15} GeV/c^2 may reach relativistic velocities.

2.5 Monopole-Matter Interaction

The possibility to detect magnetic monopoles relies on their interaction with matter and the related energy loss. For GUT monopoles the complete picture of their interaction with matter is quite complicated since all forces of the Standard Model, i.e. weak, strong and electromagnetic interaction,

Accelerator	B [μG]	L [Mpc]	E_{kin} [GeV]	Ref.
normal galaxies	3-10	10^{-2}	$(0.3\text{-}1) \cdot 10^{12}$	[50]
star-burst galaxies	10-50	10^{-3}	$(1.7\text{-}8) \cdot 10^{11}$	[51]
AGN jets	~ 100	$10^{-4}\text{-}10^{-2}$	$1.7 \cdot (10^{11}\text{-}10^{13})$	[52]
galaxy clusters	5-30	$10^{-4}\text{-}1$	$3 \cdot 10^{9}\text{-}5 \cdot 10^{14}$	[53]
extragal. sheets	0.1-1.0	1-30	$1.7 \cdot 10^{13}\text{-}5 \cdot 10^{14}$	[54]
radio galaxy lobes	$10^{-5}\text{-}10^{-4}$	10^{-1}	$10^{14}\text{-}10^{15}$	[55]

Table 2.2: Estimated magnetic field strength and coherence length for several astrophysical environments, and the associated kinetic energies a minimally charged monopole gains in a single transit through these regions. Adapted from [49].

contribute [49]. The electromagnetic interaction may dominate, due to the large magnetic coupling constant $\alpha_{\text{m}} = g_{\text{D}}^2/\hbar c \approx 34.25$ [56] and long range field. The weak and strong interactions are not well understood, and while the weak energy loss is expected to be negligible strong interaction losses may be comparable to the electromagnetic loss [49]. Lacking reliable knowledge, contributions to the total energy loss from strong interactions will be neglected in this analysis.

2.5.1 Electromagnetic Energy Loss

The electromagnetic energy loss of magnetic monopoles moving through matter with energy E can be roughly divided in collisional and radiative processes. The radiative processes, including direct pair-production, photo-nuclear interactions and emission of bremsstrahlung, dominate for Lorentz factors $\gamma = E/(Mc^2) \gtrsim 10^4$ (with M the mass of the monopole) [49]. The energy loss due to radiative processes is negligible for most GUT models since the large mass of the monopoles prevents them from reaching such ultra-relativistic energies (i.e. $\gamma \gg 1$). A comparison of radiative and collisional energy loss in air for a 100 TeV monopole is shown in Figure 2.6.

The energy loss due to collisions with atomic electrons, resulting in excitation or ionization of the atoms, is well understood and reported [57, 58]. In first approximation, a monopole with magnetic charge g and velocity βc only interacts with matter through its induced electric field $E \propto g\beta$ (see

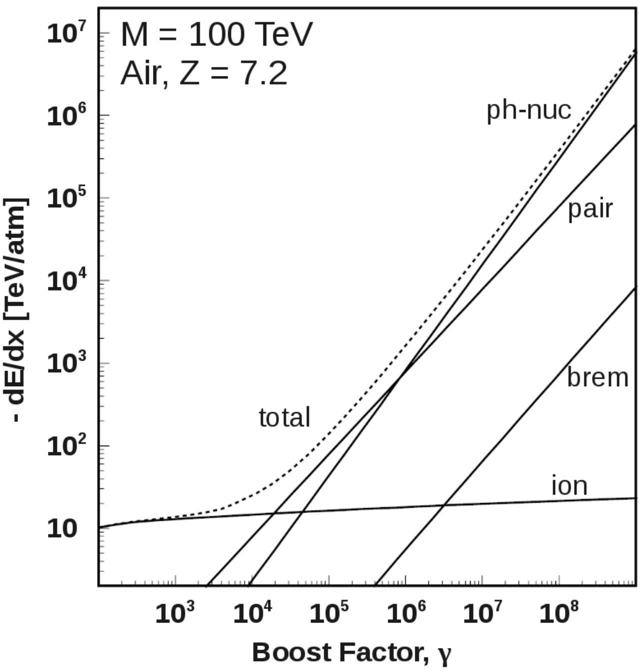

Figure 2.6: Energy loss of a 100 TeV monopole in air [49]. For $\gamma > 10^4$ radiative processes like photo-nuclear interaction and direct pair-production dominate. Bremsstrahlung is suppressed due to the large mass of the monopole.

Eq. (2.8)). The collisional energy loss should therefore be about $g\beta/ze$ times larger than for a particle with electric charge ze and the same velocity [59]. For a monopole with one Dirac charge and $\beta \approx 1$ this amounts to a factor of ~ 4700 compared to a unit electric charge.

A more detailed description of the energy loss dE per unit length dx is given by

$$\frac{dE}{dx} = \frac{4\pi n_e g^2 e^2}{m_e c^2} \cdot \left[\ln\left(\frac{2 m_e c^2 \beta^2 \gamma^2}{I}\right) - \frac{K(|g|)}{2} - \frac{1+\delta}{2} - B(|g|) \right], \quad (2.16)$$

which is the Bethe-Bloch formula modified for magnetic monopoles [60]. Here n_e is the electron density, m_e is the electron mass, I is the mean ionization energy of the medium, δ is the density correction [61], B is the Bloch correction for monopoles and K is the KYG cross-section correction

[62]. In comparison to the Bethe-Bloch formula for electrical charged particles Equation (2.16) is missing a factor β^{-1}. The reason for this is that the interaction in mainly mediated by the induced electric field of a monopole, which is proportional to its velocity (see Eq. (2.8)). As a consequence the collisional energy loss for monopoles does not feature a rise towards lower velocities as shown in Figure 2.7.

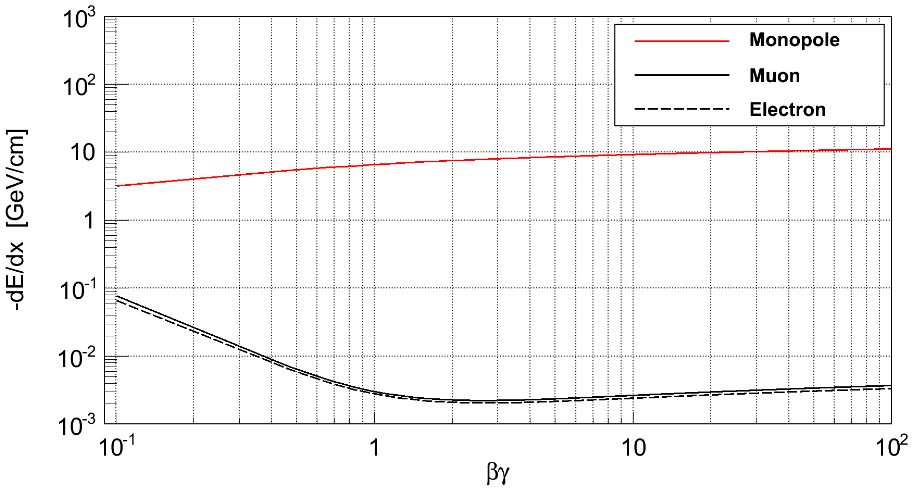

Figure 2.7: The collisional energy loss per unit path length for magnetic monopole with minimal charge. Also shown are the energy losses for muons and electrons. The characteristic increase of the energy loss towards lower velocities for electric particles is not present for monopoles.

The Bethe-Bloch formula above is valid for the velocity range where other energy loss processes can be neglected. The upper bound of $\gamma \lesssim 100$ is given by radiative losses becoming significant [58]. For velocities below $\beta \approx 0.1$ the detailed properties of the stopping medium need to be taken into account and interactions with the magnetic field of the monopole become relevant [57]. At even lower velocities ($\beta \lesssim 10^{-4}$) monopoles cannot excite atoms anymore and lose energy only in elastic collisions with atoms or with nuclei.

2.5.2 Cherenkov Radiation

When a charged particle passes through a dielectric medium, it disrupts the local electromagnetic field in the material. Whether the particle charge is electric or magnetic in nature, the atoms of the medium will become polarized and return to equilibrium by emitting photons. If the velocity of the particle exceeds the phase velocity of light in the medium, the photons are emitted coherently as so called *Cherenkov radiation* [63]. The orientation of the light front relative to the direction of the charged particle follows from Huygens' principle and is shown in Figure 2.8:

$$\cos\Theta_c = \frac{1}{\beta n} \tag{2.17}$$

where n is the refractive index of the medium.

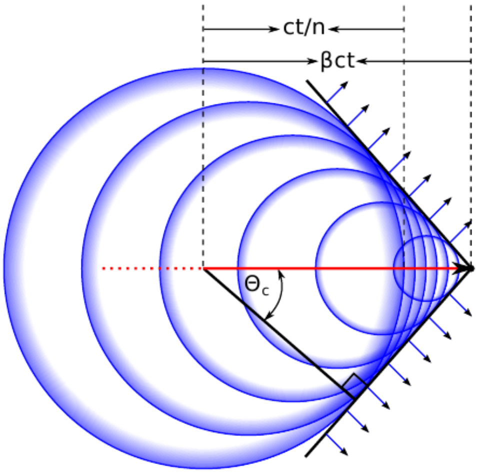

Figure 2.8: Huygens construction of the Cherenkov light cone [64].

The energy loss dE due to emission of Cherenkov radiation per unit path length dx and angular frequency $d\omega$ for magnetic monopoles is given by

$$\frac{dE}{dx} = \frac{g^2 n^2}{c^2}\left(1 - \frac{1}{\beta^2 n^2}\right)\omega\, d\omega. \tag{2.18}$$

This is the Frank-Tamm formula [65] adapted for magnetic monopoles. Additionally the relation $n^2 = \epsilon\mu \approx \epsilon$ for the permittivity ϵ and permeability μ has been used, which holds true for most materials. The effective substitution rule applied here is therefore

$$ze \mapsto gn. \tag{2.19}$$

Thus, a minimally charged monopole generates $(g_D n/e)^2$ times more Cherenkov radiation compared to an electrically charged particle with the same velocity. For $n = 1$ this is about a factor of 4700. However, the geometry and frequency spectrum of the Cherenkov radiation from magnetic monopoles remain unchanged [66].

2.5.3 Catalysis of Nucleon Decay

Any GUT model necessarily violates baryon number conservation [67]. Since the unified gauge symmetry is restored in the innermost core of a GUT monopole, they may catalyze the decay of nucleons (Figure 2.9) mediated by the exchange of a GUT gauge boson, as was shown by Rubakov [68, 69] and Callan [70, 71]. The catalysis cross section depends on the monopole velocity and takes the form

$$\sigma_{\text{cat}} = \frac{\sigma_0}{\beta}, \tag{2.20}$$

where σ_0 is roughly of the order of 1 µb [72].

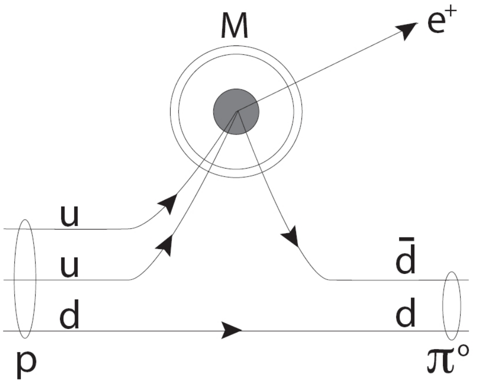

Figure 2.9: A possible nucleon decay process that could be catalyzed by GUT monopoles. The reaction is mediated by a heavy gauge boson associated with the unbroken GUT gauge group that does not conserve the baryon number. From [73].

Equation (2.20) should be understood as an order of magnitude estimate. The exact properties of the cross section depend on the monopole structure and may be suppressed by several orders of magnitude in certain heavier elements [74]. Additionally, the gauge boson mediated nucleon decay is not a general property of GUTs[3] [36, 37, 75, 76] and may not even be present in the model studied by Rubakov and Callan [77]. Despite these theoretical difficulties the possibility of such a conspicuous signature has been of great interest for monopole searches, because it permits the detection of extremely heavy and thus slow moving monopoles [78].

2.6 Monopole Flux Limits

Theoretical estimates for the number density of GUT monopoles strongly depend on the GUT model and the cosmological development of the Universe. The most reliable limits on the monopole flux are therefore not dependent on specific models and follow indirectly from cosmological considerations and astrophysical observations. However, magnetic monopoles have also been searched for directly and indirectly using different search techniques. With no confirmed detection, the limits reported by the various searches have become progressively more stringent over time and today supersede most astrophysical limits.

2.6.1 Cosmological and Astrophysical Limits

Astronomical observations indicate that the mass density of the Universe is approximately equal to the critical density [79]. Since only a fraction of this density can be attributed to magnetic monopoles, the average monopole flux is constrained to a level of

$$\langle\Phi\rangle \lesssim 10^5 \frac{\beta}{M_{17}}\ \mathrm{cm^{-2}sr^{-1}s^{-1}}, \tag{2.21}$$

assuming adiabatic expansion of the universe and a uniform monopole distribution [48]. Here, M_{17} denotes the monopole mass in units of 10^{17} GeV/c^2. The mass dependent flux limit for several monopole velocities is shown in Figure 2.10.

---

[3] Nucleon decay can still proceed through Higgs exchange, as well as via higher dimension operators [36].

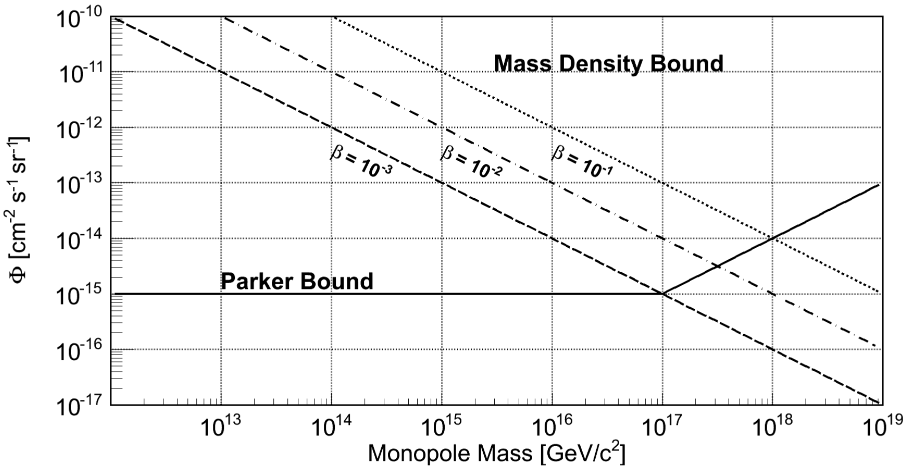

Figure 2.10: Limits on the flux of magnetic monopoles derived from astrophysical observations. The Parker bound is based on the survival of the galactic magnetic field in the presence of a monopole flux. Another bound is given by the fact that the monopole mass density must be smaller than the mass density of the universe. This limit depends on the average monopole velocity that ties the flux to the density.

Another limit on the monopole flux can be derived from the survival of the galactic magnetic field. This field of $B \approx 3 \cdot 10^{-10}$ T is believed to be (re-)generated by the dynamo effect of the galaxy with time constant of $\mathcal{O}(10^8\mathrm{y})$. However, magnetic monopoles are accelerated by magnetic fields. This energy transfer to the monopoles would eventually deplete the field strength if the monopole flux is large enough. For an initial monopole velocity of 10^{-3}c an upper limit is given by

$$\Phi \leq \begin{cases} 10^{-15}\ \mathrm{cm}^{-2}\mathrm{sr}^{-1}\mathrm{s}^{-1} \text{ for } M < 10^{17}\ \mathrm{GeV}/c^2 \\ M_{17} \cdot 10^{-15}\ \mathrm{cm}^{-2}\mathrm{sr}^{-1}\mathrm{s}^{-1} \text{ for } M \geq 10^{17}\ \mathrm{GeV}/c^2 \end{cases} \tag{2.22}$$

This limit, called the *Parker Bound* [80], is also shown in Figure 2.10. The limit is essentially divided in two region: For monopole masses below 10^{17} GeV/c^2 the monopoles are easily deflected by the galactic magnetic field. The limit then only depends on the properties of the magnetic field. For masses $> 10^{17}$ GeV/c^2 monopoles will only be slightly deflected, thus giving higher significance to the monopole parameters. The transition between the two regions depends on the initial monopole velocity and is shifted to lower masses as the velocity increases.

Astrophysical observations allow even more stringent limits on the monopole flux for GUT models that predict monopoles to catalyze nucleon decay (see Section 2.5.3). Monopoles, gravitationally captured by neutron stars, would heat up the star and produce observable ultraviolet and X-ray radiation. Since such emissions have not been detected yet, the monopole flux for catalyzing monopoles is constrained to $\Phi \leq 10^{-21}\ \mathrm{cm}^{-2}\mathrm{sr}^{-1}\mathrm{s}^{-1}$ [81, 82].

2.6.2 Experimental Searches

Experimental searches for magnetic monopoles, relativistic or non-relativistic, are commonly based on one of the two following detection methods [67]. The induction method uses Superconducting Quantum Interference Devices (SQUID) to detect the change in current on the super-conducting coil caused by a passing monopole. This method can be used to detect monopoles in matter or cosmic rays but is restricted to relatively small detectors due to background from changes in the Earth's magnetic field. A promising, yet unconfirmed, event candidate for a magnetic monopole was recorded in 1982 by an induction experiment [83].

The second detection method exploits the electromagnetic energy loss of monopoles in matter. This approach is quite versatile since it allows to search for monopoles in very unusual ways. For example, incident cosmic ray monopoles may have been absorbed in bulk materials like moon rock [86], meteorites [87] or ancient mica [88] over a exposure time of order million years leaving microscopic yet detectable tracks. Additionally, searching for signatures from electromagnetic interaction often allows to exploit detector setups designed for different purposes like the detection of cosmic rays. The limits reported by monopole searches usually consider particles with only (minimal) magnetic charge, though most experiments are also sensitive to dyons (see Section 2.4.1).

Perhaps the most comprehensive search for magnetic monopoles has been performed by the Monopole Astrophysics and Cosmic Ray Observatory (MACRO) at the Gran Sasso underground laboratory. It utilized liquid scintillator, limited stream tubes and nuclear track detectors with an effective area of about $10^4\ \mathrm{m}^2$. A complete description can be found in [89].

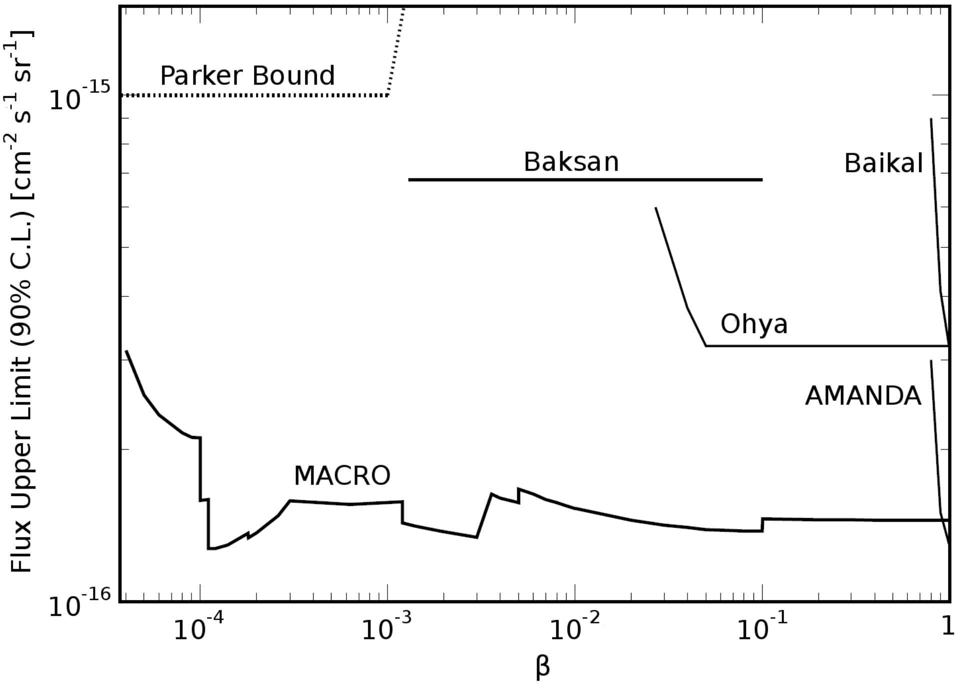

Figure 2.11: Limits on the flux of magnetic monopoles set the MACRO experiment. The rather complicated structure results from the combination of several different analyses using the various sub-detectors of the observatory. Also shown are limits set by the Ohya [84] and Baksan [85] experiments.

The velocity-dependent limits from this experiment are shown in Figure 2.11.

Flux limits for relativistic monopoles also have been obtained by neutrino telescopes like AMANDA-II [90], Baikal-NT200 [91], ANTARES [92] and IceCube [93]. These limits are shown in Figure 2.12 and supersede astrophysical limits as well as the MACRO results for $\beta \gtrsim 0.6$. At ultra-relativistic velocities the most stringent flux limits have been reported by the RICE [94] and ANITA-II [95] balloon based experiments. They obtained flux limits as low as 10^{-19} cm^{-2}sr^{-1}s^{-1} for monopoles with $10^7 \lesssim \gamma \lesssim 10^{12}$ and $10^9 \lesssim \gamma \lesssim 10^{13}$ respectively. Additionally, searches for slow monopoles ($\beta < 0.1$), based on the catalysis of nucleon decay, have been performed with the Soudan [96], MACRO [97], Baikal [98] and other experiments. The resulting flux limits are $(6 \cdot 10^{-17})$-$(9 \cdot 10^{-14})$ cm^{-2}sr^{-1}s^{-1} depending on the value of the catalysis cross sections [67].

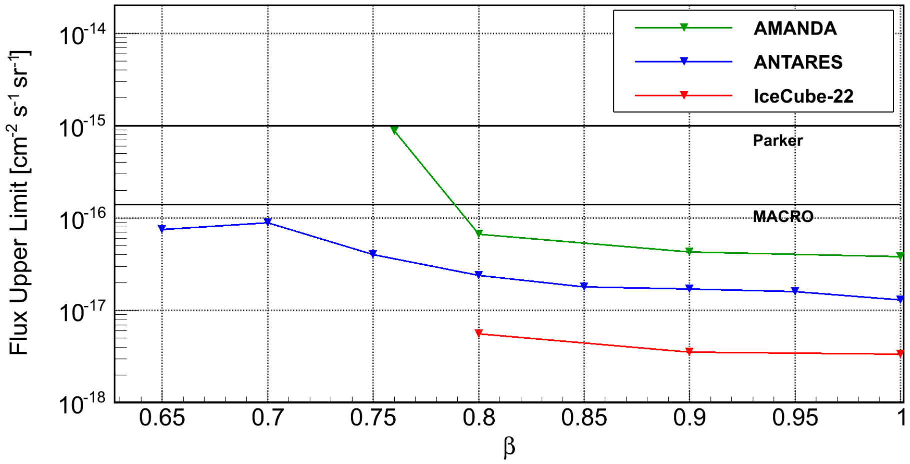

Figure 2.12: Limits on the flux of magnetic monopoles set by searches performed with neutrino telescopes. Also shown are the limit from the MACRO experiment and the Parker bound.

3 IceCube

IceCube is a cubic kilometer scale high-energy neutrino observatory located at the Amundsen-Scott South Pole Station in Antarctica [99]. Its main goal is to map the high-energy neutrino sky, which is expected to include both a diffuse neutrino flux and point sources [100]. The detector design allows to observe and study neutrinos with energies from several 100 GeV up to the EeV range. This chapter describes the scientific motivation for such a detector as well as its detection principle, structural design, data acquisition and calibration.

3.1 Motivation

One of the open questions of astrophysics is the origin of cosmic rays (CRs) at the highest energies (see Section 4.2.1). Candidates are extremely energetic cosmic environments, such as Active Galactic Nuclei, Gamma Ray Bursts and radio lobes of FR II galaxies [101]. Tracing the sources of CRs over galactic or cosmic distances is difficult, though. Protons, the main component of CRs, with energies below 10^{19} eV are deflected by galactic magnetic fields and lose all directional information. At higher energies, the travel in straight lines but the flux is suppressed due to interactions with photons from the cosmic microwave background (see Section 4.2.1).

When cosmic rays are accelerated, a fraction of the particles will interact with the ambient matter present in the source. This *astrophysical beam dump* results in the production of pions, which decay into high energy photons ($\pi^0 \rightarrow \gamma\gamma$) and neutrinos ($\pi^\pm \rightarrow \mu^\pm\nu_\mu$, $\mu^\pm \rightarrow e^\pm\nu_e$). Since both photons and neutrinos do not possess charge, they are unaffected by magnetic fields and point straight back to their source. High energy photons may, however, interact with the cosmic microwave background via pair production ($\gamma\gamma \rightarrow e^+e^-$). Hence, the probability to observe high energy photons decreases with distance to the source. Neutrinos, on the

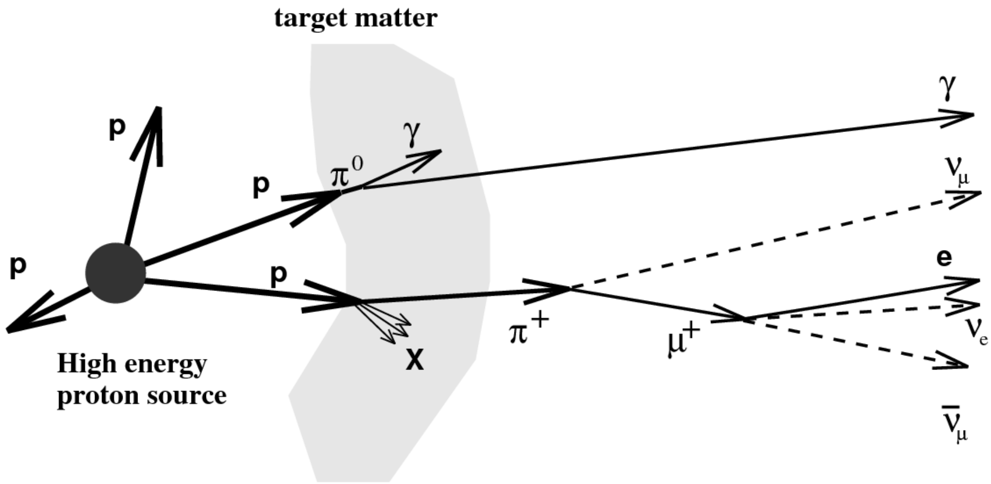

Figure 3.1: Principle of an astrophysical beam dump [102].

other hand, can escape from a source region that appears opaque to other particles and propagate undisturbed over cosmic distances because of their low interaction probability. This makes them ideal messengers to probe cosmic ray accelerators. A schematic illustration of an astrophysical beam dump is shown in Figure 3.1.

3.2 Detection Principle

Neutrinos can not be observed directly since they possess no electric charge and interact with matter only through the weak force. Hence, neutrino telescopes aim to detect the Cherenkov light (see Section 2.5.2) emitted by secondary particles produced in rare such interactions. At neutrino energies above 10 GeV the most important interaction in matter is deep inelastic scattering with a nucleus [103]. This can either occur in a neutral current (NC) interaction, mediated by a Z^0 boson, or in a charged current (CC) interaction, in which a $W^\pm$ boson is exchanged. The interaction results in a hadronic cascade X and a secondary neutrino or lepton of the same flavor:

$$\nu_l(\bar{\nu}_l) + N \longrightarrow \nu_l(\bar{\nu}_l) + X \text{ (NC)} \tag{3.1a}$$

$$\nu_l(\bar{\nu}_l) + N \longrightarrow l(\bar{l}) + X \text{ (CC)} \tag{3.1b}$$

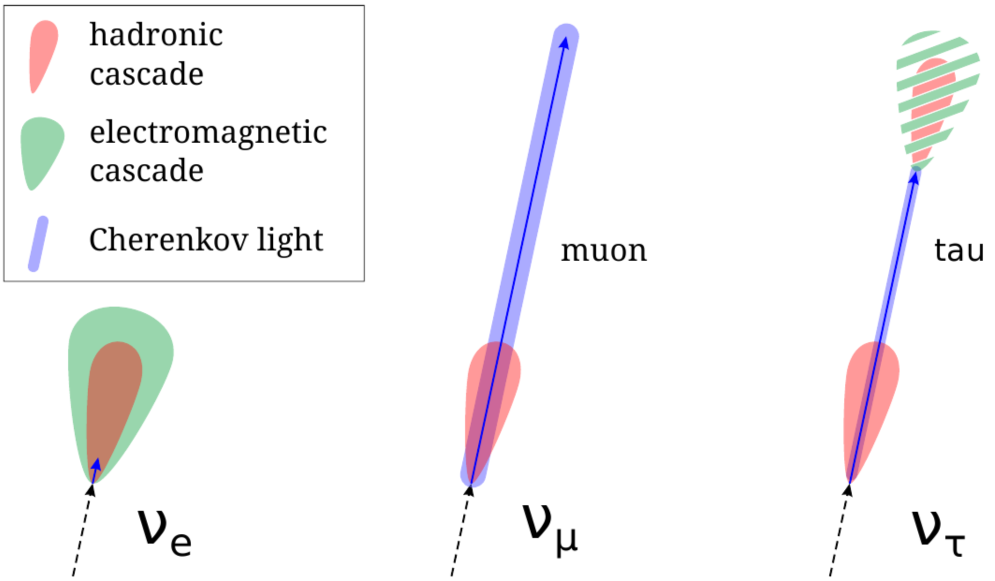

Figure 3.2: An illustration of the Cherenkov signatures of charged current neutrino interactions [104]

where l is one of the lepton flavors (e, μ, τ) and N is a target nucleus. For neutrino detection charged current interactions are favored since both the hadronic cascade and the secondary lepton emit Cherenkov radiation. In neutral current interactions the scattered neutrinos escapes the detector with a significant fraction of the total energy. Additionally the interaction probability for charged current interactions at a given neutrino energy is about one order of magnitude larger than for neutral current interactions [103].

The exact Cherenkov signature for a charged current interaction depends on the flavor of the neutrino, which is illustrated in Figure 3.2. High energy electrons produce an electromagnetic cascade that overlaps with the hadronic one. The extremely short lived taus usually decay inside the hadronic cascade, which leads to a brighter cascade. Only at very high energies the tau can leave the hadronic cascade before decaying, resulting in a second bright cascade (the so called *double bang* signature). Finally, the relativistic muons produced in ν_μ-interactions have a long range, that causes a track-like Cherenkov signature.

In most cases the muon channel is the preferred detection channel in order to search for the origin of high energy cosmic rays, because the track like signature provides the best directional information. At TeV energies the muon direction and energy can be reconstructed with an accuracy of the order of 1° or better by measuring arrival time and intensity of the Cherenkov light at different points in the detector. The direction of the neutrino is closely related to that of the muon with an upper limit of the angular difference given by [105]

$$\langle \Theta_{\nu\mu} \rangle < \frac{1.5^\circ}{\sqrt{E_\nu/\mathrm{TeV}}} \tag{3.2}$$

while the energy of the neutrino is roughly twice the muon energy.

The advantages of the muon channel for neutrino detection are diminished by a large background of muons from CR induced air showers in the earth atmosphere. Unlike these atmospheric muons, however, neutrinos can pass through the earth and produce muons that enter the detector from below. Hence, the atmospheric muon background can be suppressed significantly by selecting only muon signatures with directions from below the horizon. The remaining background is then composed of a small fraction of atmospheric muons for which the directional reconstruction failed and muons from neutrinos created in CR interactions on the opposite side of the Earth.

3.3 Detector Design

The small interaction probability of neutrinos poses a challenge for astrophysical observations. Kilometer-scale detectors are required to detect the predicted cosmic neutrino fluxes. Additionally the detection medium must be sufficiently clear and shielded from outside light in order to allow the detection of Cherenkov radiation. Since it is impracticable to construct detectors of this size and properties from scratch, existing neutrino telescopes utilize naturally occurring environments. IceCube is buried between 1450-2450 m deep in the glacial ice shield at the geographic south pole. The deep underground location also provides shielding from muons produced in air showers in the atmosphere, which are the major background for this detector type. Similar neutrino detectors are NT-200 at Lake Baikal as well as ANTARES [106] and its planned successor KM3NeT [107] in the Mediterranean Sea.

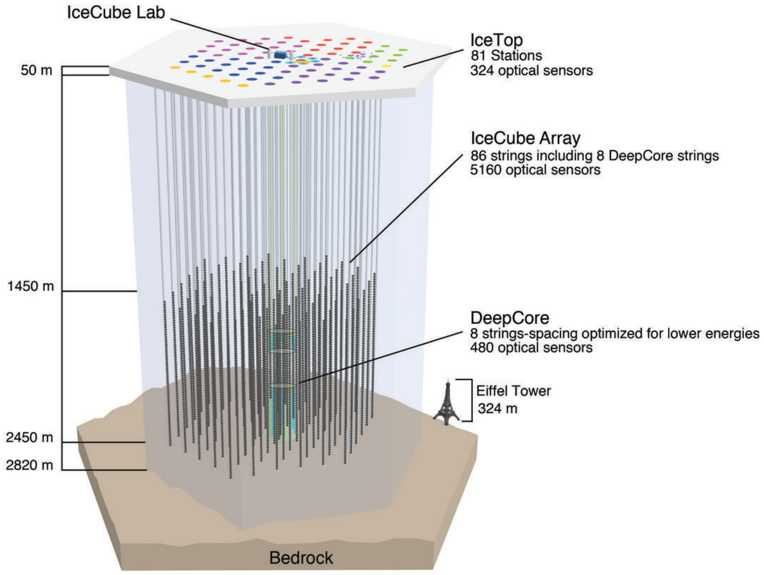

Figure 3.3: A sketch drawing of the IceCube detector. Also shown are the low energy extension Deep-Core and the cosmic ray air shower detector IceTop at the surface.

3.3.1 Geometry and Deployment

The basic layout of the IceCube detector is depicted in Figure 3.3. The main component is the deep *InIce* array consisting of 78 long cables, called *strings*, each of them equipped with 60 optical sensors called Digital Optical Modules (DOMs). The strings are placed in water-filled holes, which have been bored with a hot-water jet. The water refreezes after a while, optically coupling the DOMs to the surrounding ice but also rendering them permanently inaccessible. The strings are arranged in a hexagonal pattern with an average spacing of 125 m covering an area of $\sim 1\,\mathrm{km}^2$ (see Figure 3.4). The instrumented volume spans from 1450-2450 m below the surface with a DOM spacing of 17 m. In this configuration the lower energy threshold for neutrino detection is of the order of 100 GeV [99].

In the central part of the InIce detector 8 additional strings are deployed in between the standard strings. These string are equipped with 60 high-efficiency DOMs. The lower 50 DOMs are located in the very clear deep ice

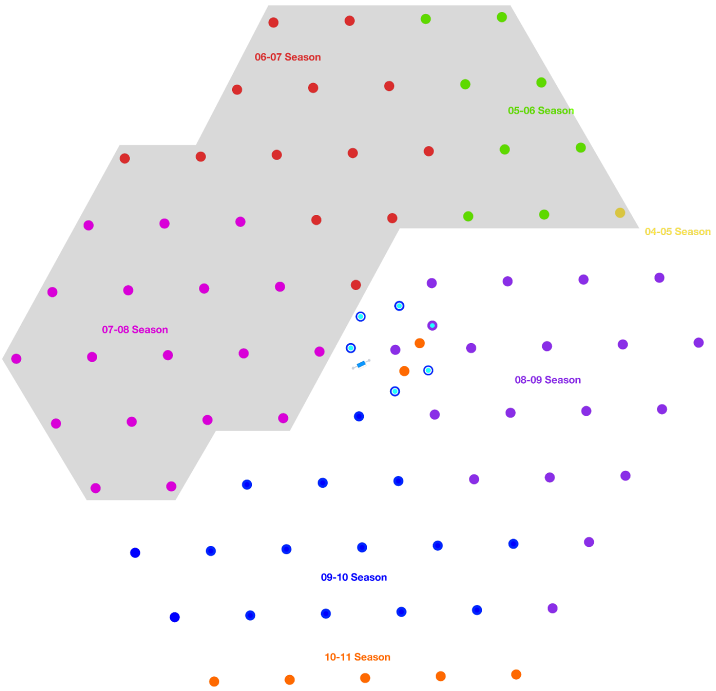

Figure 3.4: Top View of the IceCube array. The colors indicate the order in which the strings were deployed in the ice, by season. This analysis considers only the strings deployed up to the 2007-08 season.

below a depth of 1700 m with a spacing of 7 m. The remaining 10 DOMs are located in a depth of 1700 m − 1850 m with a spacing of 10 m. In the intermediate region no DOMs are deployed because of the very short effective scattering lengths (see Section 3.3.3).These 8 strings, together with the 7 central regular IceCube strings, constitute the *DeepCore* subdetector [108]. The higher efficiency of the DeepCore DOMs and denser instrumentation increase the sensitivity in the low energy regime below a few hundred GeV with a lower energy threshold of ∼ 10 GeV.

The InIce array is complemented by the *IceTop* surface air shower detector. IceTop consists of 162 polypolyethylene tanks, each filled with 2.5 m^3 bubble-free ice and instrumented with two DOMs [109]. The tanks are positioned in pairs on the same grid as the vertical InIce cables. The two tanks at each surface station are separated from each other by 10 m. The surface detector is designed to study the mass composition of primary cosmic rays in the energy range from about 100 TeV to 1 EeV. Additionally, IceTop can act as a veto for atmospheric muons from air showers in the InIce detector.

The IceCube detector has been constructed in several stages. Because of the harsh conditions at the geographic south pole deployment is only possible during austral summer (from Nov. to Feb.). Construction started in the 2004/2005 season and was completed in 2010/2011. Between the construction periods the IceCube detector has been taking data using the already deployed strings. The data for the presented analysis was obtained in 2008/2009 while IceCube was roughly half complete with 40 deployed strings (IC40) and an instrumented volume of ~ 0.5 km^3.

3.3.2 Digital Optical Module (DOM)

The Digital Optical module is the fundamental light detection unit of IceCube [110]. The DOM's main hardware elements are a Photomultiplier Tube (PMT) and the DOM Mainboard (DOM MB) holding important electronics. The components are encased in 35.6 cm diameter glass sphere. Internal power, including the PMT high voltage, is derived from the nominal ±48 V DC, supplied by a twisted pair cable, which also carries communication and timing signals. A schematic view of a DOM is shown in Figure 3.5. The individual components are described in the following.

Photomultiplier Tube

The PMT allows to convert light into an electrical signal. Primary electrons are generated in a photocathode by the *photoelectric effect* when incident photons strike the material and are therefore called photo-electrons (PE). The efficiency of the photon to electron conversion depends on the photon wavelength and the material of the photocathode. A multi-staged electrode (dynode) array then multiplies the electrons through the process of secondary emission. The multiplied electrons are measured as a current at an anode terminating the electrode array. The multiplication factor for primary electrons is called the gain and depends on the high voltage (HV) value applied to the dynode array. The gain value allows to determine the number of PEs recorded by the PMT.

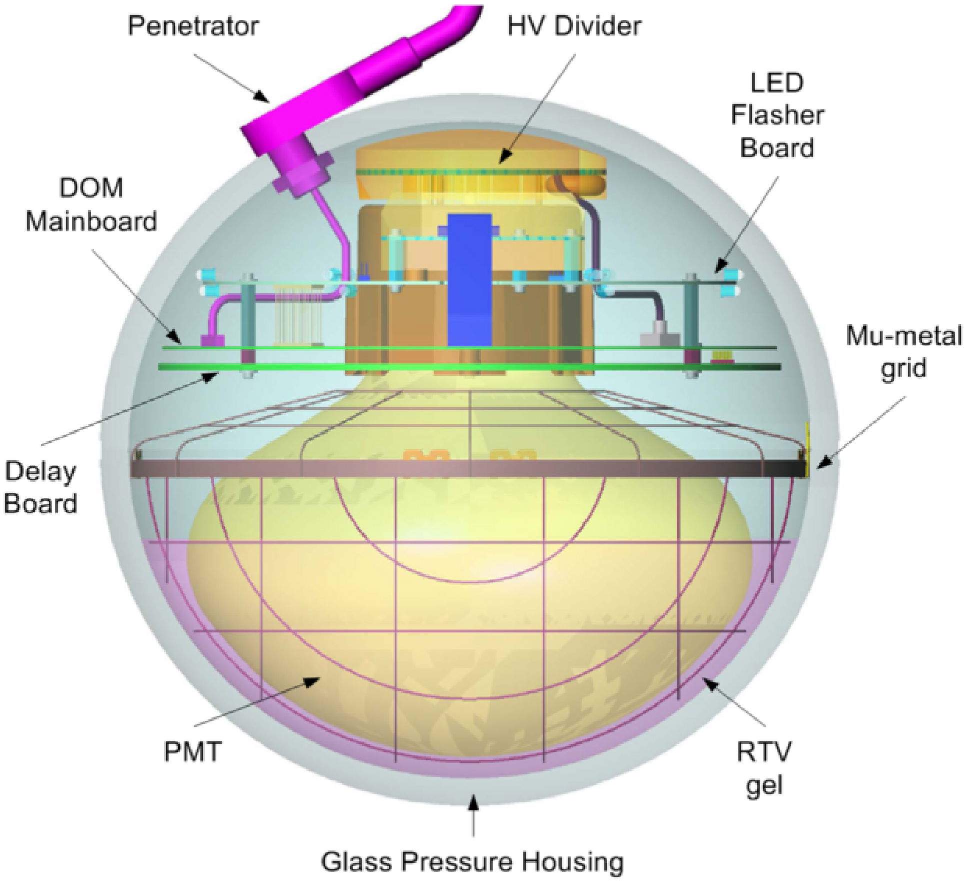

Figure 3.5: Schematic illustration of a Digital Optical Module [111]

IceCube DOMs are equipped with a commercial Hamamatsu R7081-02 PMT [112]. This 25 cm diameter PMT is optimized for optical wavelengths between 300-600 nm with a peak quantum efficiency of $\sim$ 25% at 390 nm. PMTs installed in DeepCore DOMs reach 33% quantum efficiency. Inside the DOM the PMT is surrounded by a permalloy sheet and wire in order to decrease the effect of the earth's magnetic field on the PEs. Optical coupling of the PMT to the glass sphere and mechanical support is provided by a flexible gel. For InIce DOMs the PMT is operated at a gain of 10^7. The two PMTs in each IceTop tank are operated at different gains (10^5 and $5 \cdot 10^6$) in order to better cover the dynamical range of the extremely different signals in air showers [109]. Otherwise IceTop and InIce DOMs are technically identical.

DOM Mainboard

The analog output signal is not send directly to the surface since the signal quality is affected by dispersion in the cable. Instead the signal is digitized before transmission by the electronics on the DOM MB, which also manages triggering and time-stamping. The functional blocks of the DOM MB are shown in Figure 3.6. The PMT signal is split into three paths at input to the DOM MB: An on-board trigger as well as low and high quality digitizers. Additionally, an electrical pulser allows to inject a controlled charge into the analog signal path for calibration purposes. All paths are controlled by Altera EPXA-4 Field-Programmable Gate Array (FPGA), which can be reprogrammed remotely [111]. The DOM MB also controls 12 so-called *flasher LEDs* installed on a dedicated circuit board. The LEDs produce bright UV optical pulses with controllable output levels and pulse lengths, which can be detected by other DOMs. They are used to measure the optical properties of the ice (see Section 3.3.3), simulate physical events and calibrate the detector (see Section 3.5.1).

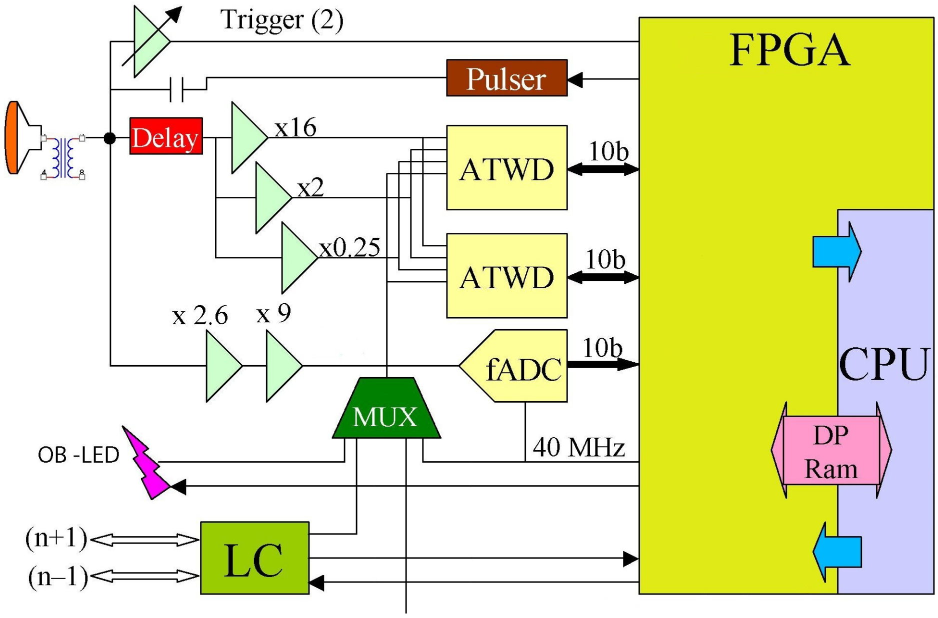

Figure 3.6: A simplified block diagram of the DOM Mainboard electronics. See [111] for the complete version. The operation of the components are described in the text.

The on-board trigger system consists of two high-speed comparators (discriminators) with a configurable threshold. The comparators have different resolutions and operating ranges and are intended to sense single photo-electron (SPE) and multi photo-electron (MPE) pulses. Once the PMT signal exceeds one of the comparator thresholds (~ 0.2 PE for the SPE comparator) the FPGA initiates data acquisition and synchronizes the trigger signal to the next leading edge of the DOM internal clock. Running at 40 MHz the time resolution of the clock is 25 ns. Together with the digitized PMT waveform, this coarse timestamp constitutes a *hit*, the fundamental IceCube data unit. A finer time resolution can be derived later from the digitized PMT waveform. The FPGA also receives trigger information from the 4 neighboring DOMs on the same string. Full readout of the digitized waveform is only initiated if at least one of these DOMs report a trigger within a ±1 µs time window [113]. Otherwise only the timestamp and a coarse measure of the charge will be transmitted to the surface. These two modes are referred to as *Hard Local Coincidence* (HLC) and *Soft Local Coincidence* (SLC). However, SLC data is only available since the operation start of the 59-string configuration in 2009. For the data taken with the IC40 detector only the HLC information was recorded.

The main digitizer system uses an Analog Transient Waveform Digitizer (ATWD), which is a custom Application Specific Integrated Circuit [114, 111]. The four input channels of the ATWD store 128 samples in analog memory with a sampling rate of 300 megasamples per second (MS/s) (3.3 ns/sample) until they are digitized or discarded. The covered time window of ~ 422 ns is in most cases sufficient to capture the physically relevant part of a waveform. The PMT signal is forwarded to three of the four input channels with amplification factors of 16, 2 and 0.25. The different amplification accounts for the large dynamic range of signals from 0.2 PEs up to several hundred PEs. This is illustrated in Figure 3.7. The fourth channel is used for calibration and monitoring.

The waveform capture sequence of the ATWD is initiated by the FPGA once a trigger signal from the PMT discriminator has been received and timestamped. Trigger formation in the FPGA and sending the signal to the ATWD to start recording typically takes less than 50 ns and about 20 ns respectively. Thus, the PMT signal is send through a 75 ns delay line on its way to the ATWD. Digital conversion of the captured waveform starts with the highest gain channel. The lower gain channels are only digitized, if the channel with the next higher gain overflows, i.e. any sample

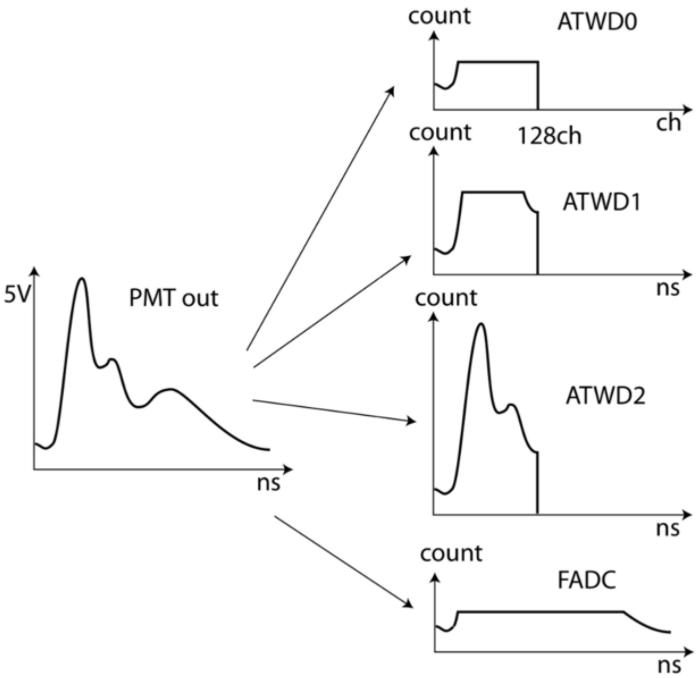

Figure 3.7: An illustration of the four waveform digitization channels. The three ATWD channels operate at different gains (top to bottom ×16, ×2 and ×0.25) to capture the full dynamic range of the waveform. The PMT ADC (labeled FADC here) operate at a fixed gain (×23.4) but covers a much longer time range than the ATWD channels. Taken from [115].

in this channel exceeds 768 counts. The ATWD takes 29 µs to convert a captured waveform, including data transfer and incidental overhead. During this time the ATWD is not available for signal capture. In order to minimize dead time the DOM MB is equipped with two ATWDs operating in ping-pong fashion. Additional dead time reduction is achieved by converting waveforms only if the logical conditions set by the local coincidence mode are met. The total dead time fraction is estimated to be less than 10^{-4}.

The ATWDs are supplemented by a second digitizer system intended for signal lasting longer than the ATWD capture time window. It uses a commercial Analog Digital Converter (ADC), referred to as *PMT ADC*[4]

---

[4] An alternate but inaccurate description is flash/fast ADC or fADC

[111]. The PMT ADC continuously samples the signal with 40 MS/s (25 ns/sample) synchronized to the on-board clock. To account for the coarser time binning, the signal path includes a three stage waveform shaping amplifier with a 180 ns shaping time and total gain of 23.4. The amplification ensures that a digitized SPE signal is sufficiently above the ADC's baseline to be detected. In response to an on-board trigger a total of 256 PMT ADC samples covering a 6.4 µs time window are recorded by FPGA. This includes the time bin corresponding to the trigger time stamp as well as the three previous bins to capture the full physics event. The output of the PMT ADC channel is also illustrated in Figure 3.7.

3.3.3 Detection Medium

The largest part of IceCube is the instrumented polar ice serving as both Cherenkov medium for relativistic charged particles and physical support structure. Having formed naturally over thousands of years from compressed snow the polar ice sheet is about 2820 m thick with a layer structure. The approximately horizontal layers contain different types and concentration of impurities due to fluctuating atmospheric conditions. Understanding the optical properties of the ice is crucial in order to measure the trajectories and energies of events within IceCube.

The most relevant properties for the propagation of Cherenkov photons are scattering and absorption. Scattering occurs on small impurities in the ice such as submillimeter-sized air bubbles or dust particles, affecting both timing and direction. The scattering process is mathematically described by Mie scattering and can be characterized by an effective scattering length [116]. This parameter defines the path length after which a photon has lost its initial direction information due to repeated non-isotropic scattering. Absorption occurs on both impurities and the ice itself. Similar to scattering absorption is characterized by a length scale parameter, which is defined as the distance at which the survival probability of a photon drops to 1/e.

The scattering and absorption lengths can be measured in-situ using the flasher LEDs mentioned in Section 3.3.2. Figure 3.8 shows the inverse effective scattering length and inverse absorption length in dependence of depth and wavelength. In the topmost kilometer scattering is dominated by the contribution of residual air bubbles which results in an effective scattering length of the order of 1 m. In deeper ice layers the bubbles

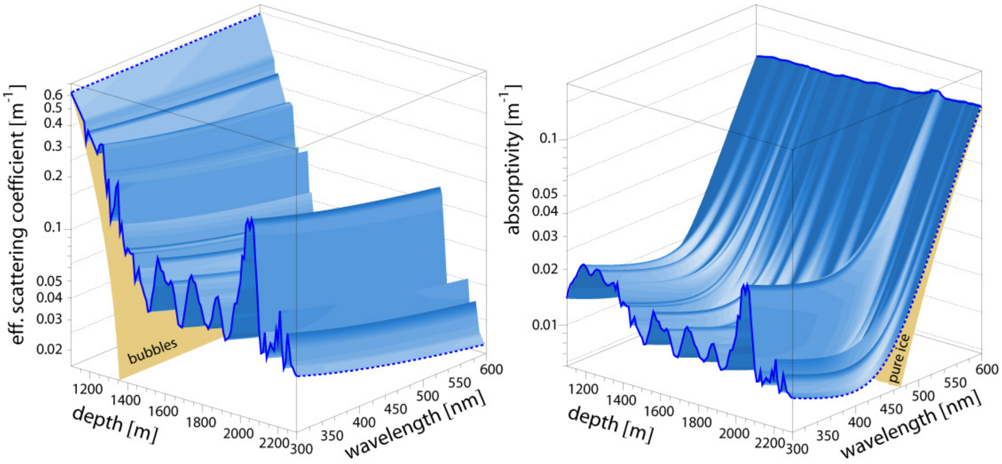

Figure 3.8: Absorption coefficient (left) and scattering coefficient (right) in the South Polar ice as functions of depth and wavelength [116]

are converted to non-scattering air hydrates by the high environmental pressure. Below 1350 m the ice is very clear with absorption lengths of ∼ 100 m and effective scattering lengths of ∼ 20 m. Since the minimal spacing between two IceCube DOMs is 17 m, this means that most photons are scattered at least once before detection. The deep ice also features several layers with increased scattering and absorption due higher dust concentrations. The most prominent one, called the *dust layer*, is situated at a depth of about 2100 m and features an effective scattering length of less than 10 m, thus being hardly optically penetrable.

3.4 Data Acquisition

When a hit is recorded by a DOM and the local coincidence conditions are met, the hit information is send to the surface over twisted pair cables. At the surface the individual hits are captured by the Data Acquisition (DAQ) system, which either combines the into an detector event or discards them. The DAQ consists of special hardware and software components, which are explained in the following. A schematic overview is shown in Figure 3.9. The data is recorded in so-called *runs*, which define a certain configuration of the DAQ and are usually 8 hours in duration.

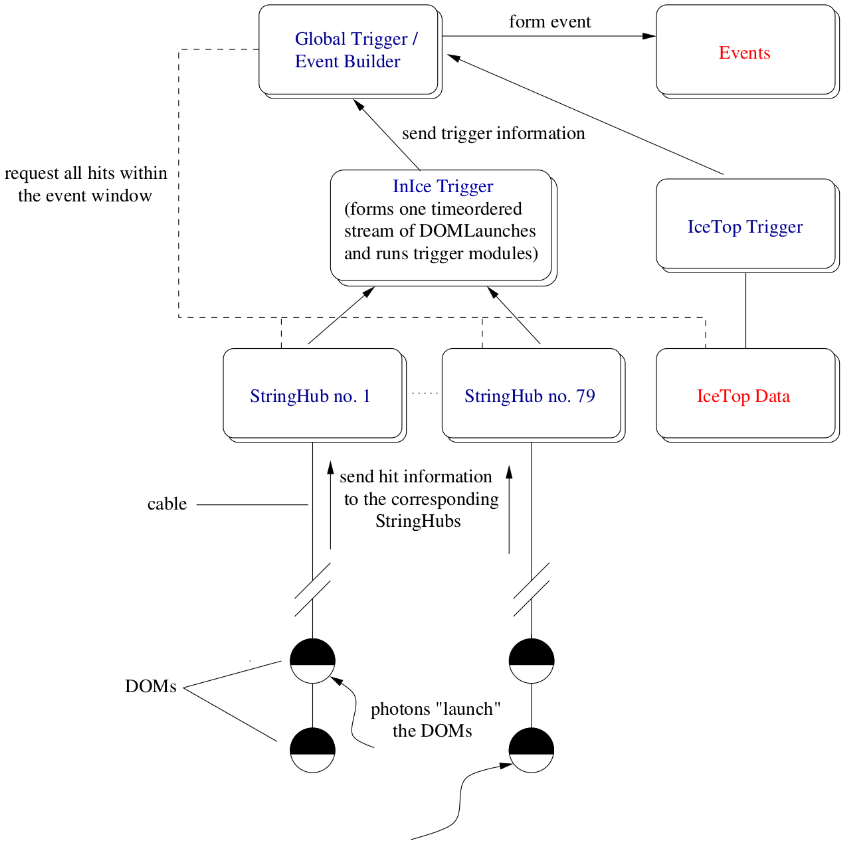

Figure 3.9: Schematic of the IceCube Data Acquisition [117]. Hardware components are colored blue. Data are colored red. The components are described in the text.

3.4.1 Hardware

The DAQ hardware for IceCube is housed in the IceCube Laboratory (ICL) located on the ice surface in the center of the detector. The equipment includes standard industrial computers that run the Java based DAQ software and provide temporary storage capacity for the event data.

Each InIce string is connected to a so called *DOM Hub* computer containing 8 DOM Readout (DOR) cards, one DOMHub Service Board (DSB) and single board computer. A single DOR card can provide 8 DOMs with power and time calibration signals and manages communications with them. For IceTop only 4 DOMs are serviced per DOR card because of the higher data rate. The DSB card distributes the system timing and reference signals to the DOR cards, which are derived from a system clock and a Global Positioning System (GPS) reference signal. The latter originates from a GPS receiver that is also located in the ICL.

3.4.2 Software

StringHub

Each DOMHub computer hosts a software component called the *StringHub*, which facilitates higher level communications to the rest of the DAQ software [111]. The StringHub receives the hits from all DOMs on a string and applies a time transformation to the coarse timestamp accompanying a DOM hit. These transformations bring all data into an universal time domain, the IceCube Time, which differs from the Coordinated Universal Time (UTC) by a static offset. The DOM hits are then time ordered by the StringHub and cached for several seconds for later retrieval. A minimal version of the time ordered DOM hits is send multi-string trigger handlers (see Section 3.4.2), which send back a readout request if the configured trigger conditions are met.

Triggering

The task of the trigger software is to determine when data from the entire IceCube detector should be recorded. An event is build hierarchically from one or more trigger modules as illustrated in Figure 3.10. The low-level modules are a series of algorithms that are applied to all hits satisfying the local coincidence condition. When one of the modules finds its trigger condition fulfilled it sends a readout request to *Global Trigger* in the top level. The intermediate *Throughput* level manages time window information for a specific trigger, which is used to merge different readout requests. The Global Trigger then handles all readout requests and merges request overlapping in time.

The implemented trigger algorithms and configurations may vary for different data taking seasons and are supervised by the Trigger Filter Transmission Board. However, the main trigger algorithm for all previous seasons is the *Simple Majority Trigger* (SMT), which uses only hit-time infor-

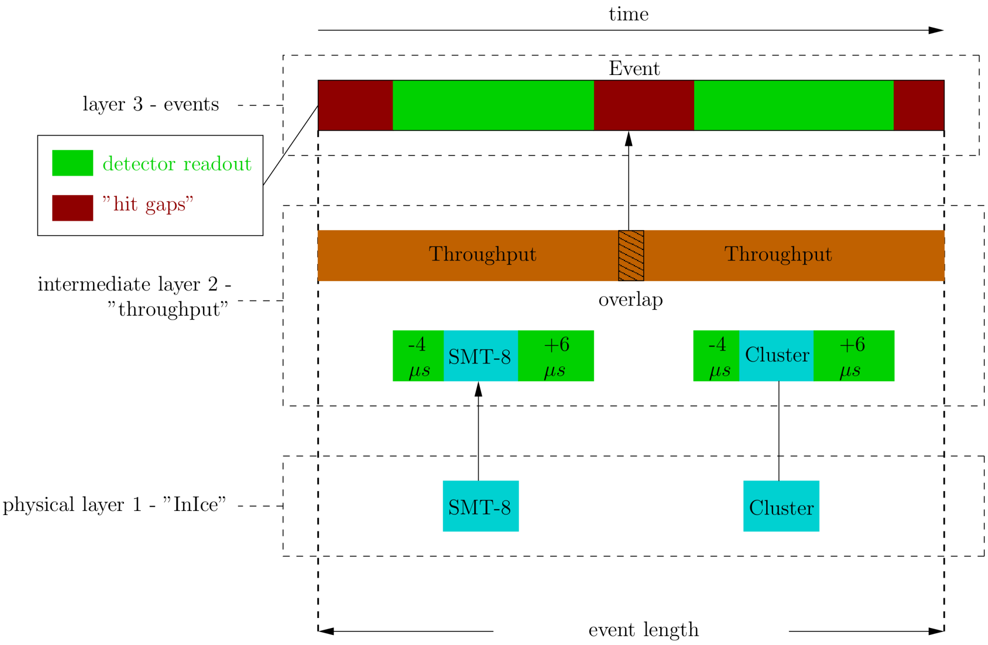

Figure 3.10: Illustration of the trigger hierarchy [117]. Different triggers are combined into one event if their corresponding Throughput Triggers overlap. Since the readout windows are shorter than the throughput window, hits occurring between two triggers may be missing from the record.

mation. For the 2008/2009 season the InIce SMT condition was 8 DOMs reporting a hit within a time window of 5 µs. Hits that follow afterward are included as long as they also fulfill the trigger condition. The time difference between the first and last hit in this series then defines the trigger length. The readout time window of a SMT also includes 10 µs before and after the trigger window in order to capture all relevant hits.

Other trigger algorithms in place during the 2008/2009 season include a *String Trigger*, an *Ultra Low Energy Event* (ULEE) trigger and a SMT for IceTop. The String Trigger is specifically designed to respond muon that traverse the detector almost vertically by looking for hit clusters on a single string [118]. The ULEE trigger simply applies a different configuration of the String Trigger algorithm to look for low energy neutrino events [119]. For subsequent seasons this task was transferred to the DeepCore subdetector.

Filtering

Data taken with IceCube has to transferred to the northern hemisphere via satellite because of the remote location at the South Pole. However, the available bandwidth ($\sim$ 25 Gb/day) is significantly lower than the data rate from all triggered events ($\sim$ 100 Gb/day). The number of events to transmit is thus reduced by further filtering, which selects several types of physically interesting signatures. Each filter is associated with a *prescale factor* n, which selects only every nth filtered event for transmission. This allows to adjust the data rate for the individual filter. In addition to the transfer via satellite, all triggered events are currently written to tapes at the South Pole and later shipped to the north.

The physics filters for the 2008/2009 season are listed in Appendix C. Notable physics filter are the *Muon Filter*, which aims to select particle tracks from muon neutrino interactions and the *Cascade Filter*, which selects bright light burst from electron neutrino interactions. Several *Minimum Bias* filters retain an unbiased sample of events presented to the filtering system, which is used for evaluation and verification purposes.

Another notable filter is the *Extremely High Energy* (EHE) Filter, designed for neutrino searches in the energy region 10^7-10^{10} GeV. The EHE Filter for 2008/2009 requires that the total number of PEs, which is a measure of brightness (see Section 3.5.3), is larger than $10^{2.8} \approx 630$. Events caused by relativistic magnetic monopoles should predominantly pass this condition because of their bright nature (see Section 2.5.2) making this filter a suitable base for a monopole search.

3.5 Calibration

The essential information required to reconstruct an event in IceCube are the timing and integrated charge of each recorded waveform as well as the position of the corresponding DOM. This section describes the calibration procedures that are applied to ensure the reliability of the recorded data.

3.5.1 Geometry Calibration

The *Geometry Calibration* is a multi-staged procedure, that determines the relative position of all DOMs within one meter. The first stage is a string wise calibration based on data taken during deployment. Two pressure sensors located 1000 m on the string combined with measurements allow to determine the depth of the lowest DOM. The depths of the remaining DOMs follows by successively subtracting the known DOM spacing. The horizontal position of the string is measured by a survey of the drill equipment. From this the horizontal positions of the individual DOM is calculated by adding depth dependent drift corrections based on drill data. The data from all strings is then compiled in the so called *Stage 1 geometry* [120].

The second stage of calibration is to determine the relative depth offsets between the strings relative to the Stage 1 geometry. For this purpose measurements using the flasher LEDs (see Section 3.3.2) are used, where the flashing DOM and the receiver DOM are on different strings. The depth offset for a certain flasher-receiver combination can be reconstructed from the distribution of photon travel times. A global fit to all available data then yields the depth offset for pairs of strings, which is incorporated into the Stage 1 geometry [121].

The third and final stage of geometry calibration tracks the gradual deformation of detector array due to ice shear, the differential horizontal motion of the ice with time. Since inter-string flasher measurements have little horizontal sensitivity, a method called *muon tomography* is used to determine the positions of individual DOMs [122]. The calibration procedure for a given DOM calculates the DOM's contribution to the track likelihood of high quality down-going muon tracks as a function of the DOM's position. The maximum of this map is the best-fit for the DOM's position.

3.5.2 Time Calibration

Time information in IceCube is recorded locally by each DOM with an internal free running oscillator clock. The main task of time calibration is to synchronize this ensemble of several thousand clock with the UTC reference. This is achieved with a method called Active Pulsing Calibration (RAPcal) [111], which allows to determine phase and frequency of the DOM clock relative to a GPS controlled oscillator on the surface.

The RAPcal process starts by the DOR card (see Section 3.4.1) transmitting a precisely timed bipolar pulse to the DOM. The DOM receives the pulse after dispersion and attenuation in the cable and records both digitized waveform and coarse timestamp. An identical bipolar pulse is then send back to the DOR card, after a short delay to ensure quiet condition on the cable. The DOR receives and timestamps this pulse in the same way as the DOM using identical electrical components. Finally the DOR requests the digitized pulse waveform and timestamp from the DOM.

The symmetry or reciprocity of pulse generation and reception of the dispersed, attenuated pulse at both ends allows to calculate the one-way propagation time as

$$\tau = \frac{\rho - \delta}{2}, \tag{3.3}$$

where ρ is the round trip time and δ the delay time of the DOM [111]. The offset between DOM clock and DOR master clock can then be determined by comparing the two recorded waveforms after correcting for the propagation time. An example is shown in Figure 3.11. The statistical error on the propagation time can be minimized by measuring repeated calibration pulses. Additionally, the ratio of time intervals between the pulses on the DOM and DOR side gives the frequency ratio for DOM clock and master clock:

$$\frac{\nu_{\mathrm{DOM}}}{\nu_{\mathrm{master}}} = \frac{\Delta T_{\mathrm{DOR}}}{\Delta T_{\mathrm{DOM}}}. \tag{3.4}$$

The overall time precision achieved with RAPcal is of the order of 1 ns and mostly limited by electronic noise on the cable. The whole calibration procedure is repeated every few seconds and takes less than ~ 1.4 ms, during which PMT signals are continued to be captured, digitized and buffered. The process should therefore be invisible to normal data taking.

3.5.3 DOM Calibration

The individual DOMs are calibrated regularly with a program named *DOMCal.*The calibration functions performed by DOMCal include measuring of transit times and residual baselines. The main functions are, however, calibration of the front-end electronics and PMT gain.

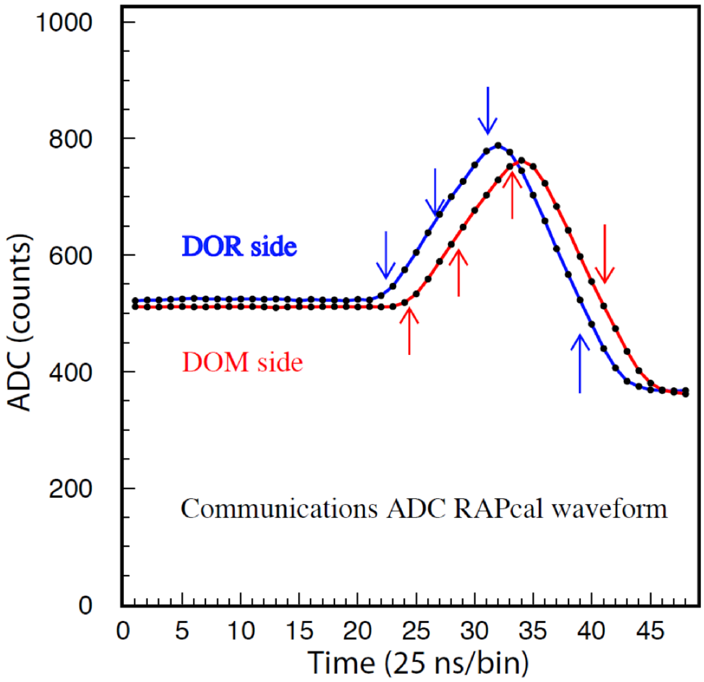

Figure 3.11: A typical RAPcal waveform with several time marks (arrows). The offset between the local DOM clock and the DOR master clock is given by the relative shift of the waveform recorded at the DOR side (blue) and the DOM side (red). From [111]

Calibration of the front-end electronics is necessary to translate the digitized PMT waveform into the number of photo-electrons (NPE) recorded by the DOM. Ideally, the NPE is proportional to the number of photons received by the PMT and thus a measure of brightness. The calibration procedure measures quantities like the threshold for the on-board trigger or the gain and waveform pedestal pattern for the ATWD and PMT ADC readout channels. For this purpose, a pulser on the DOM MB can inject waveforms similar to SPE PMT pulses and configurable amplitude into the signal path. The desired calibration quantities are then derived by mapping the electronics response for different input signals.

The calibration values found for front-end electronics are subsequently used to calibrate the PMT gain. For this, DOMCal measures the PMT response to a single PE in terms of an integrated charge, which relates to the gain. For each DOM a map of the gain is created by varying the high voltage. The individual PMT are then set to HV values that ensure a uniform gain of 10^7 throughout the entire detector.

4 Monopole Detection with IceCube

In this chapter, the Cherenkov light emission by magnetic monopoles and likely sources of background are discussed. These two aspects determine the possibility to detect relativistic monopoles with the IceCube detector and reach sensitivities below the Parker Bound (see Section 2.6).

4.1 Signal

As shown in Section 2.5.2 relativistic magnetic monopoles are expected to emit immense amounts of Cherenkov light when traversing a transparent medium. A straight forward approach for a monopole search is therefore to look for events with an extremely bright Cherenkov signature. This section quantifies the generation of Cherenkov light for the special case of ice as the detection medium and gives some constrains on the accessible monopole parameter space.

4.1.1 Cherenkov Signature in Ice

The total number of Cherenkov photons per track-length $\mathrm{d}x$ and wavelength interval $\mathrm{d}\lambda$ emitted by a monopole follows from Equation (2.18):

$$\frac{\mathrm{d}^2 N_\gamma}{\mathrm{d}x\mathrm{d}\lambda} = \frac{2\pi\alpha}{\lambda^2}\left(\frac{gn}{e}\right)^2\left(1 - \frac{1}{\beta^2 n^2}\right). \tag{4.1}$$

Since the number of photons is proportional to $\mathrm{d}\lambda/\lambda^2$, the Cherenkov spectrum is dominated by shorter wavelengths. A minimally charged monopole in ice ($n \approx 1.32$) generates $\mathcal{O}(10^6)$ photons per centimeter in the wavelength interval between 400 nm and 600 nm. The total energy loss due to Cherenkov radiation is about 300 MeV/cm, two orders of magnitude less than the ionization energy loss.

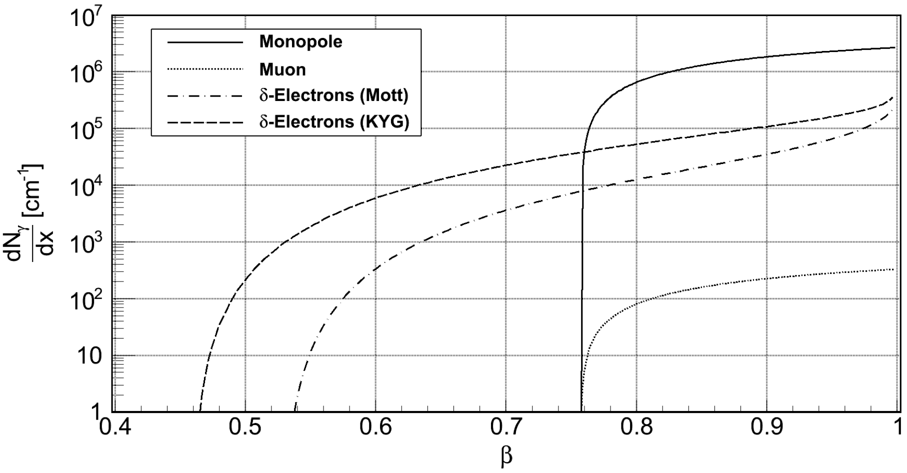

Figure 4.1: The number of Cherenkov photons generated per unit path length as a function of velocity for magnetic monopoles and muons. The two lines labeled as δ-electrons represents the Cherenkov light from secondary electrons generated by a monopole at a given velocity and are based on different calculations of the monopole-electron cross section.

Unlike muons, magnetic monopoles do not need to be ultra-relativistic in order to be detectable with a neutrino telescope. In fact, even close to the Cherenkov threshold ($\beta \approx 0.758$ in ice) a monopole emits as much Cherenkov radiation as a bare electric charge with $\beta \approx 1$. This is illustrated in Figure 4.1, where the number of Cherenkov photons emitted by monopoles and muons as a function of their velocity is shown. As a consequence, the Cherenkov angle (see Eq. (2.17)) for monopoles can be smaller than muons ($\Theta_c \approx 40.7°$). This may poses a problem during event reconstruction since many algorithms available in the IceCube software collection are optimizes for a fixed velocity of $\beta = 1$.

Another source of Cherenkov radiation are secondary electrons, which have been knocked out of atoms and accelerated by a passing monopole. Since electrons are much lighter than a monopole, this is even possible when the monopole itself is below the Cherenkov threshold. The number of photons generated by the secondary electrons depends on the cross section for monopole-electron interaction. Results from calculations using the Mott [59] and the Kazama-Yang-Goldhaber [62] cross sections are included in Figure 4.1. However, for monopoles above the Cherenkov threshold the additional light due to secondary electrons is only a small correction and therefore neglected in this work. A more elaborated treatment underlying theory as well as the detection of these *subthreshold monopoles* can be found in References [105] and [123].

4.1.2 Parameter Space

Detecting magnetic monopoles with neutrino telescopes requires that the monopoles move at relativistic velocities in order to generate Cherenkov light either directly or through secondary effects. The sensitivity of these telescopes therefore depends on the monopole mass, initial kinetic energy at the Earth's surface and energy loss in the Earth. Since this analysis treats mass and kinetic energy as free parameters, they are constrained by the energy loss, which is a function of the zenith angle direction.

The total energy loss has been simulated for 21 different values of $\cos\theta$ ranging from -1 to 1 in increments of 0.1, taking into account the structure of the Earth as well as stochastic energy losses [124]. The results are shown in Figure 4.2. One can understand the general shape of the constrained parameter space by considering three mass ranges. For small masses the Lorentz boost becomes large and stochastic energy losses rise dramatically. Hence, below a certain mass threshold monopoles are stopped in the Earth and the allowed parameter space cuts of sharply.

At larger masses the energy loss is dominated by the ionization loss described by the Bethe-Bloch formula (2.16). Considering, for example, a monopole traversing the full diameter of the Earth, the total energy loss is of the order of 10^{11} GeV [125] independent of its mass. For other zenith directions the total energy loss is lower, of course. In order to retain relativistic, the initial kinetic energy must be of about the same order as the energy lost. The parameter space is thus constrained by a minimum kinetic energy, which only depends on the zenith direction.

Finally, at even larger masses the energy loss in the Earth is too low to impact the velocity of the monopole and an already relativistic monopole will not be slowed down to subrelativistic velocities. The boundary of the allowed parameter space is then given by the initial kinetic energy required for a monopole to be relativistic, which is linearly increasing function of the mass.

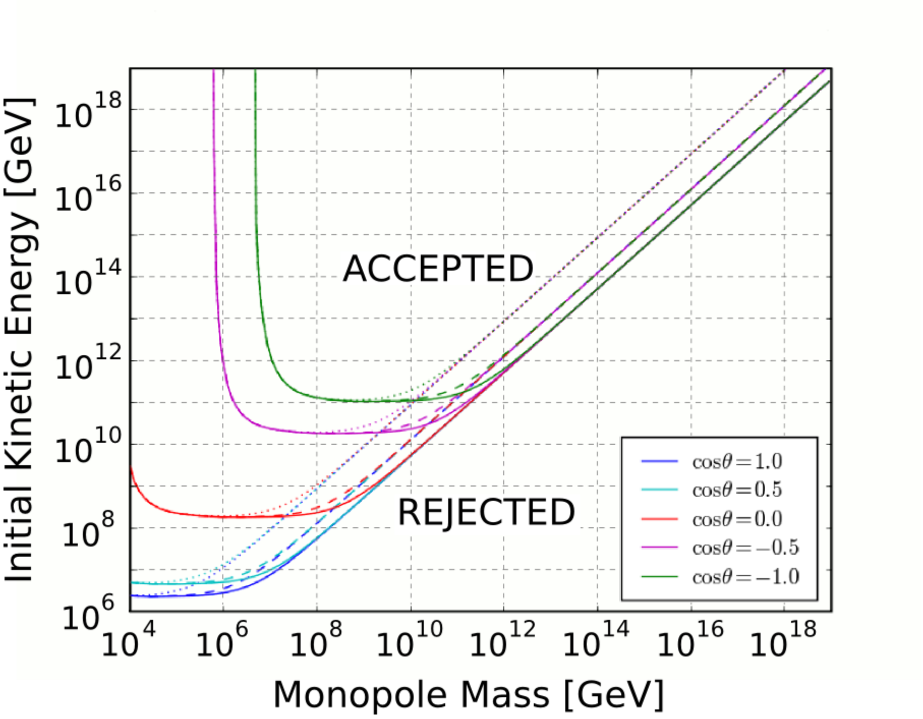

Figure 4.2: The parameter space of magnetic monopoles accessible by the IceCube detector. Monopoles in the rejected region can not reach the detector with relativistic velocities. The colors represent different arrival directions e.g vertically down-going (green) or vertically up-going (blue). Dotted lines are for a threshold of $\gamma = 10$, dashed for $\beta = 0.9$ and solid for $\beta = 0.76$

4.2 Background

The fundamental background for magnetic monopole searches at relativistic velocities in IceCube are secondary particles produced by cosmic ray interactions in the Earth's atmosphere. The secondary particles may be muons or neutrinos that produce leptons in a charged current interaction near the detector (see Section 3.2). A thorough understanding of CR properties is essential in order to get a suitable description of the background and ultimately separate it from the signal.

4.2.1 Cosmic Rays

Cosmic rays were discovered by Victor Hess in 1912 when he measured ionization rate of air as a function of altitude during several balloon flights [126] and have been actively researched ever since then. Though many important questions about CR still remain open, a standard description has evolved, which will be briefly summarized here. For a more detailed description, see [67] or [101].

Composition

The composition of CRs was first measured during the 1940s with cloud chambers and photographic plates carried to high altitudes in balloon experiments. It was found that the primary CR flux consists of fully ionized atomic nuclei moving at relativistic velocities. The most abundant elements are hydrogen ($\sim$ 90%) and helium ($\sim$ 9%), whereas heavier elements as well as electrons, positrons and neutrons only contribute $\sim$ 1% [127]. The relative abundance of the elements in CRs is very similar to the one found in the solar system and all elements of the periodic table have been observed [101]. Higher abundance of elements such as lithium and beryllium in CRs are assumed to be the result of spallation processes during propagation. The composition therefore indicates that CRs are regular interstellar matter accelerated to extremely high energies. Changes of the CR composition with energy are believed to be related to the involved acceleration mechanism. However, at energies above 10^{14} eV CRs can only be detected indirectly from extended air showers in the atmosphere. At these energies even resolving groups of elements poses an experimental challenge due to uncertainties in the hadronic interaction models used to describe air shower development. The current knowledge of the CR composition at high energies is therefore limited.

Energy Spectrum

The differential energy spectrum of all CR particles, as depicted in Figure 4.3, spans many orders of magnitude on both axis. Primary CR particles have been measured with energies ranging from several MeV to at least 10^{20} eV. The overall particle flux at the top of the atmosphere decreases rapidly with increasing energy ranging from about 10000 nuclei per square

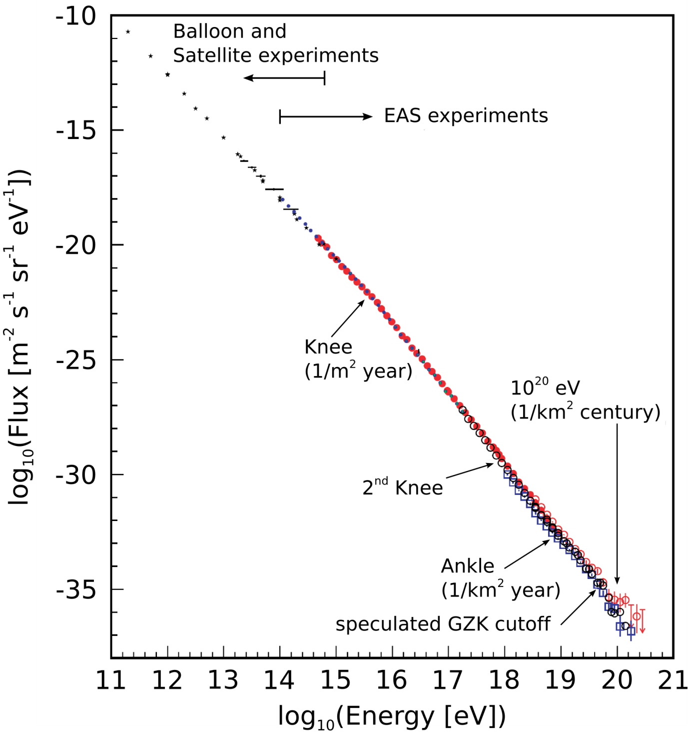

Figure 4.3: The energy spectrum of primary cosmic rays derived from direct observations with balloon- and satellite-borne detectors as well as indirect observations with air shower detectors [129].

meter and second at GeV energies to less than one particle per km^2 and century above 10^{20} eV. Though the spectrum appears relatively featureless, following a power law $\mathrm{d}N/\mathrm{d}E \propto E^{-\gamma}$, three kinks become visible if the flux is weighted with some power of the energy as seen in Figure 4.4. The first around $3 \cdot 10^{15}$ eV is the so called *knee*, where the slope of the spectrum steepens reflected by the change of the spectral index of the power law from $\gamma \approx 2.7$ to $\gamma \approx 3.1$ [101]. The existence of a *second knee* has been claimed around $4 \cdot 10^{17}$ eV with the spectral index changing to $\gamma \approx 3.3$ [128]. At about $4 \cdot 10^{18}$ eV, the *ankle* marks the spectrum flattening again to $\gamma \approx 2.7$. Finally, the spectrum cuts of sharply beyond $5 \cdot 10^{19}$ eV.

The power law form of the energy spectrum, as well as the CR composition, is believed to be the result of non-thermal acceleration processes. First-order Fermi acceleration [131] in shock fronts of supernova remnants is

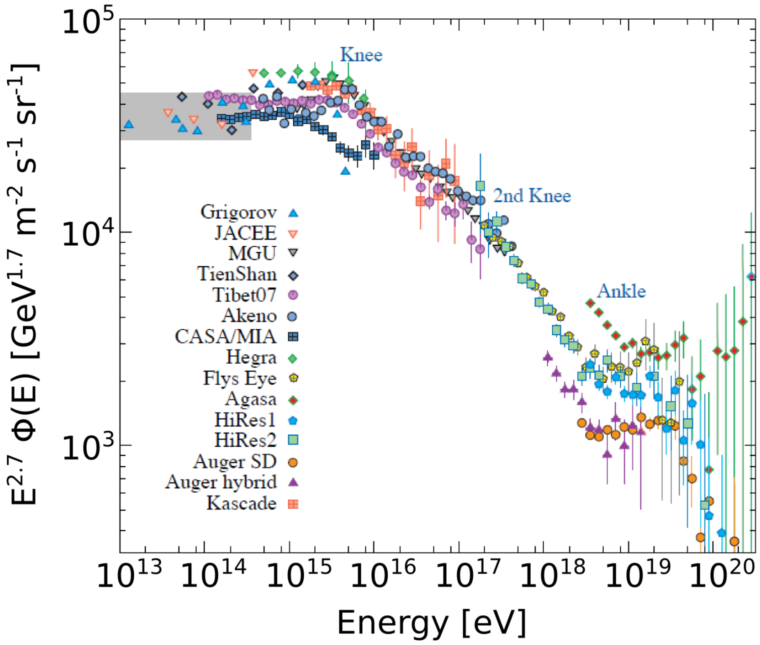

Figure 4.4: Air shower measurements of the CR energy spectrum with the particle flux multiplied by $E^{2.7}$ to highlight the structure [130].

generally assumed to be the source of CRs up to 10^{17} eV [132]. In this picture, the knee is supposedly related to an upper limit of acceleration in galactic supernovae as well as leakage of CRs from the galaxy [101]. In both cases the limiting factor is magnetic confinement and the spectra of individual elements with charge z would cut off at energies of

$$E_c^z = z \cdot E_c^p, \tag{4.2}$$

where E_c^p is cut-off energy for protons. The CR composition is thus expected to shift to heavier elements above the knee in agreement with current measurements [101]. The knee is then the result of the proton cut-off, whereas the subsequent cut-offs for heavier elements causes the steeper but smooth spectrum above the knee. The origin of the second knee has not yet been conclusively determined. However, a recent theory attributes it to the cut-off of a significant ultra-heavy component in CRs [133].

First-order Fermi acceleration in shock fronts can not explain CR energies above $\sim 10^{18}$ eV since the maximum attainable energy is limited by

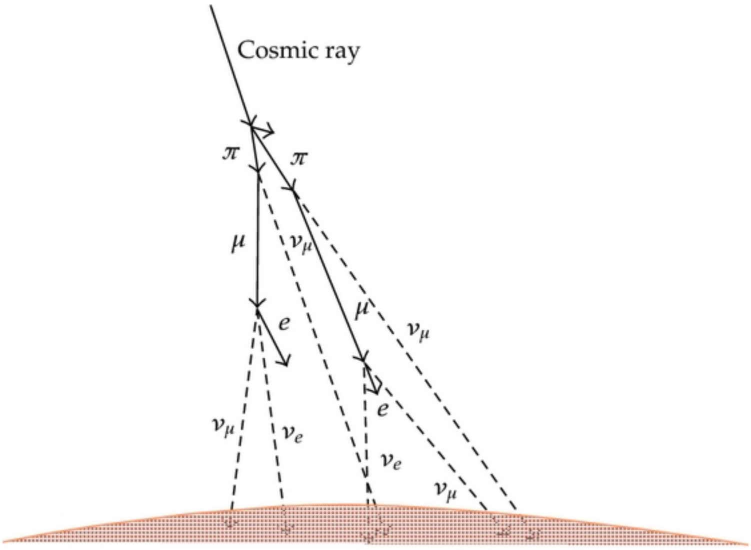

Figure 4.5: Schematic drawing of the production of atmospheric muons and neutrinos [136].

the finite lifetime of the shock front. Additionally, CR particles at these energies have gyro radii larger than the extension of the galactic disk. Hence, they are believed to be of extragalactic origin and the ankle is interpreted as the onset of this component. The suppression of the CR flux at the highest energies is often related to the absorption of protons through pion production with photons from the 2.7 K microwave background ($p\gamma \rightarrow \Delta^+ \rightarrow n\pi^+(p\pi^0)$). This effect is referred to as the Greisen-Zatsepin-Kuzmin (GZK) cut-off [134, 135].

4.2.2 Atmospheric Muons

Atmospheric mouns predominantly originate from the decay of charged pions and kaons that were created in CR interactions in the atmosphere. This is illustrated in Figure 4.5. At energies above a few GeV, mouns are capable of reaching the surface before decaying. Their energy and angular spectrum is then a convolution of the primary CR spectrum energy loss in the atmosphere and decay probability [67]. In the 10-100 GeV range the muon energy spectrum reflects the $E^{-2.7}$ spectrum of the primary CR.

However, at higher energies the spectrum steepens by about one power since pion decay is suppressed by interactions in the atmosphere. At these energies, muons from the decay of short-lived mesons containing heavy quarks, most notably charm, are also expected to contribute significantly to the spectrum [137].

Neutrino detectors are often placed deep underground to shield them from the muon flux at the surface. However, atmospheric muons with energies above $\sim$ 100 GeV can penetrate to depths of several kilometers. Hence, the majority of detected particles are still atmospheric muons. Figure 4.6 shows the vertical muon intensity as a function of depth in water equivalent. With an overburden of $\sim$ 1.5 km ice, the expected trigger rate due to atmospheric muons in the 40 string IceCubeIC40 detector was about 1 kHz [138]. At this depth, the energy spectrum above several hundred GeV still reflects the surface spectrum.

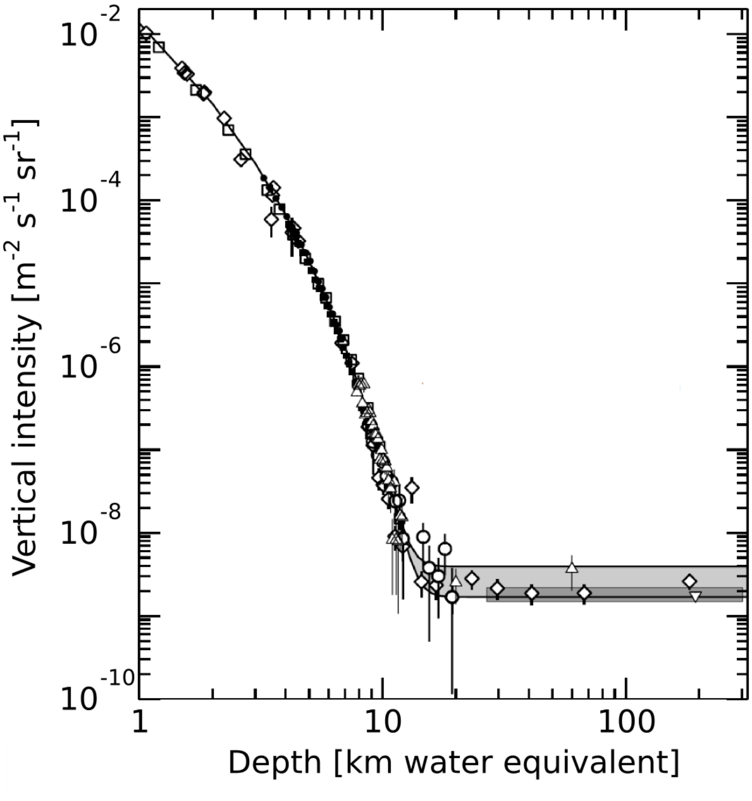

Figure 4.6: Vertical muon intensity vs depth [67]. The shaded area at large depths represents neutrino-induced muons of energy above 2 GeV.

One would expect atmospheric muon events with a total Cherenkov light yield comparable to magnetic monopoles to be extremely rare, due to their steep energy spectrum. However, high energy CR interactions in the atmosphere produce bundles of many nearly parallel muons. While the individual muons are of relatively low energy, they may still reach the underground detector for primary energies above 100 TeV. Thus, a larger fraction of the total energy is deposited in the detector as Cherenkov light. Since the muons are highly collimated and close to each other in space [139, 140], they mimic the signature of a single extremely high energetic (EHE) particle.

A common feature of atmospheric muons is that they enter the detector from above the horizon (see Figure 4.7). Rejecting particles traveling downward through the detector is thus an effective way to eliminate the atmospheric muon background. The downside of this approach is that one also rejects half of a signal with isotropic direction distribution. Thus, searches for cosmic EHE neutrinos, magnetic monopoles or other particles with a bright Cherenkov signature often attempt to extend their search region above the horizon. In any way, the zenith direction of an event remains a key observable in order to reject atmospheric muon.

4.2.3 Atmospheric Neutrinos

Atmospheric neutrinos occur as decay products of charged mesons in the same way atmospheric muons do (see Figure 4.5). In theory, muon-neutrinos (ν_μ) and electron-neutrinos (ν_e) and their anti-particles are created with ratio of 2:1. However, at energies relevant for IceCube, above $\sim$ 100 GeV, muons tend to interact in the atmosphere before they can decay. Due to this suppression, the ν_e flux at sea level is about an order of magnitude lower than the ν_μ flux [142]. In fact, most ν_e at these energies originate from the decay of charged kaons. A similar effect causes the direction distribution of atmospheric neutrinos to peak at the horizon, as seen in Figure 4.7. At this incident angle the pions and kaons travel a longer distance in the thin upper atmosphere where interactions are less likely to occur. This is known as the $\sec\theta$ effect [67].

The competition between meson decay and interaction in the atmosphere also effects the energy spectrum of the secondary neutrinos. The spectrum of ν_μ from meson decay is one power of energy steeper than the primary cosmic ray spectrum ($\propto E^{-3.7}$). For ν_e the spectrum is two powers of

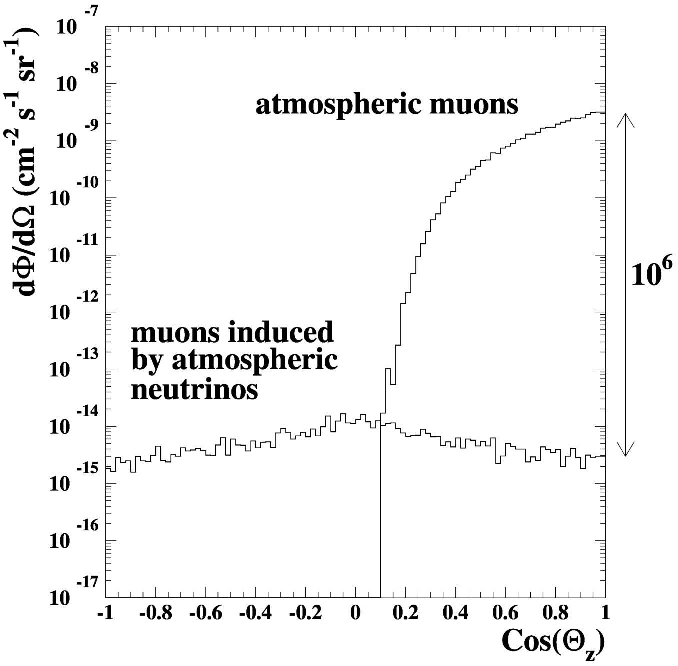

Figure 4.7: Zenith angular distribution of the muon flux above 1 TeV from atmospheric muons and atmospheric neutrino induced muons at 2300 m water equivalent depth [141].

energy steeper ($\propto E^{-4.7}$), because the parent muons are decay products themselves. At energies above 10^5 GeV kaons also encounter the interaction-decay competition and a prompt neutrino component begins to dominate the spectrum. These prompt neutrinos are daughter particles from the decays of charmed mesons, which are also responsible for prompt atmospheric muon flux [137]. A summary plot of the atmospheric neutrino fluxes and measurements is shown in Figure 4.8.

While the rate of atmospheric neutrino events registered by IceCube is about a factor 10^6 less than atmospheric muon events [144], they can not be neglected in monopole searches. This neutrino background is dominated by muons from ν_μ CC interactions near the detector. Events caused by ν_e or NC interactions can be effectively rejected since their signature is sufficiently different from a monopole (see Section 3.2). In order to generate a similar amount of Cherenkov light as a monopole, the muon from a ν_μ interaction must be of extremely high energy and so must the neutrino

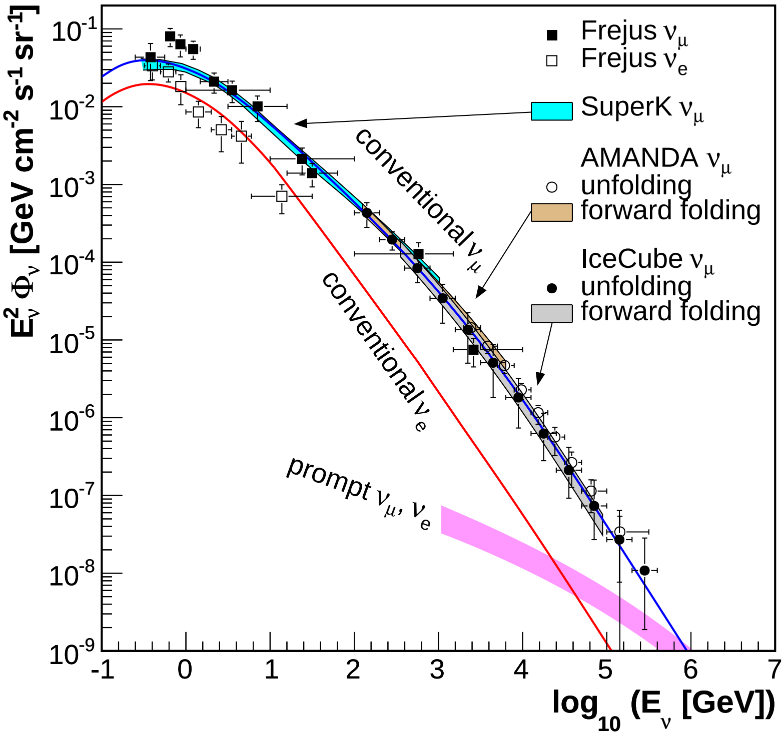

Figure 4.8: Atmospheric neutrino fluxes from measurements and model predictions [143]

itself. Hence, one expects prompt neutrinos to contribute significantly to the neutrino background, due to their flatter energy spectrum.

4.2.4 Cherenkov Signature of Background Muons

Analog to Equation (4.1), the total number of Cherenkov photons per track-length dx and wavelength interval dλ emitted by a muon is given by

$$\frac{\mathrm{d}^2 N_\gamma}{\mathrm{d}x\mathrm{d}\lambda} = \frac{2\pi\alpha}{\lambda^2}\left(1 - \frac{1}{\beta^2 n^2}\right). \tag{4.3}$$

The minimum kinetic energy for muons to emit Cherenkov radiation in ice is about 160 MeV. However, the ionization energy loss of muons is of the order of MeV per centimeter and would only emit Cherenkov radiation along a few meters of its path. Hence, a muon must be ultra-relativistic $\beta \approx 1$ in order to be detectable by a neutrino telescope. At these energies, a muon emits about 200 photons per centimeter in the relevant wavelength interval at a Cherenkov angle of $\Theta_C \approx 40.7°$. This is $\mathcal{O}(10^4)$ less Cherenkov light than emitted by a bare magnetic charge at the same velocity

The direct Cherenkov light from ultra-relativistic muons is enhanced by secondary particles. These particles are generated by stochastic energy loss processes, which dominate over the continuous ionization energy loss above 600 GeV [145]. Since the momenta of secondary particles are aligned with the muon track, the Cherenkov light is emitted roughly at the same angle preserving the conical signature. At $\sim$ 14 PeV the total amount of Cherenkov light emitted by a muon is about the same as that of a magnetic monopole with $\beta \approx 1$.

5 Simulation

This analysis tries to measure a small signal using a series of experimental selection requirements, or *cuts*. In this scenario, prior knowledge of the effect of the event selection on the data may result in an unwanted bias. For example, the cuts may be tuned to exclude a few extra background-like events, yielding a lower limit [146]. To avoid such bias, the analysis is developed in a blind way. This means the experimental data is kept concealed and the choice of cuts based only on simulated data.

This chapter gives a brief overview of the simulation software and summarizes the main stages of the simulation: Generation, propagation, light injection and detector response. Generation and propagation for signal and background events is handled by different software modules and will therefore be described separately. Light injection and detector response, on the other hand, uses common IceCube software modules.

5.1 Simulation Software

The IceCube software suite is a C++ based environment that provides a framework for simulation, reconstruction and analysis applications [147]. The framework is designed to be modular, allowing the user to consecutively execute software modules performing specific tasks. For certain applications, like simulation or reconstruction, the basic software components are available as a *meta-project*, including standard toolboxes of modules for the specific task. Additionally, users can write their own modules and integrate them into the process chain.

Control flow for the modules is provided by the *IceTray* frame work, the centerpiece of the IceCube software. It offers an easy and straightforward way to configure data processing by using Python-based steering scripts. Within IceTray data is stored in a heterogeneous data container called a frame. Usually a frame contains the detector readout from one global trigger but geometry, calibration and configuration of the detector are also available. Each frame is passed from module to module, reading the data and adding new one.

5.2 Monopole Simulation

The generation of magnetic monopoles is handled by a module conveniently called *Monopole-Generator*. Its function is to create and initialize the basic data structures required by the other modules in the simulation chain. The original module was implemented for a previous monopole analysis [93, 124].

The generator samples the initial vertices of monopole track such that they are uniformly distributed on a generation disk as illustrated in Figure 5.1. The monopole direction is set perpendicular to the disk towards the detector. The radius of the disk and the distance to the detector center along its symmetry axis are configurable parameters. Simulations for this analysis use a radius of 850 m and distance of 1000 m. These choices ensure that the monopoles start well outside the detector and sufficiently cover the acceptance region of the detector. The orientation of the disk relative to the detector is randomized for each new monopole track, resulting in an isotropic flux.

Additional configuration parameters for the generator module include the mass of the monopole, the initial velocity and the number of events to generate. Since the manner in which the light propagation is simulated (see Section 5.4) requires the monopole speed to be approximately constant, the monopole mass was chosen to be 10^{11} GeV/c^2. With this choice the Cherenkov angles for the four considered monopole velocities, $\beta = 0.995$[5], 0.9, 0.8 and 0.76, do not change significantly over a track length of $\mathcal{O}(1\text{ km})$ [124]. For the three fastest monopole velocities 10^5 events are simulated, whereas for $\beta = 0.76$ 10^6 events needed to be generated to ensure enough statistic in the final sample.

The second step of the simulation chain is to propagate the monopole through the detector, which is handled by a module called *Monopole-Propagator*. The propagator determines the energy loss of the monopole based on Equation (2.16) and tracks the velocity change. The latter is

---

[5] The monopoles are actually simulated with an initial Lorentz boost of $\gamma = 10$, which gives $\beta \approx 0.995$. The β-notation is used for reasons of consistency.

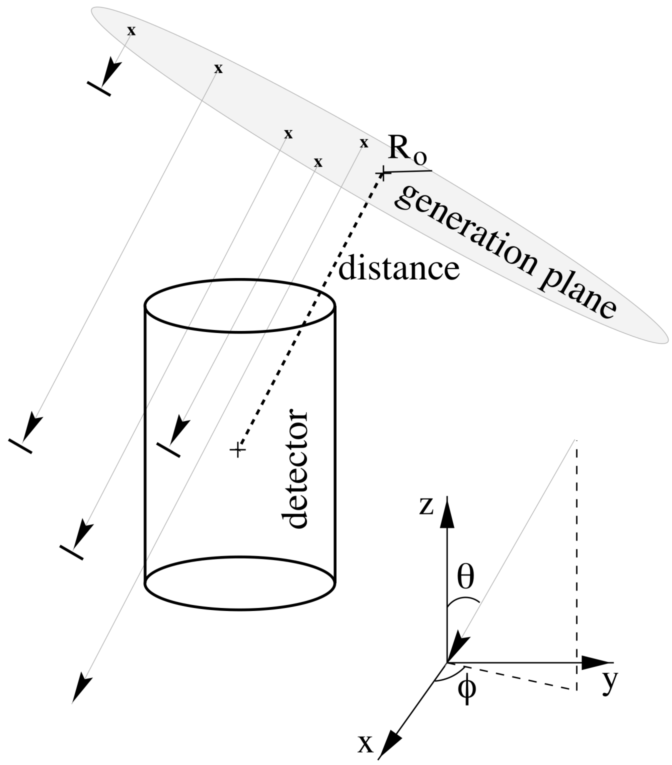

Figure 5.1: Generation of monopole tracks [148]. The starting point of each track is sampled from generation disk of radius $R_0 = 850$ m at a constant distance of 1000 m from the detector center.

achieved by subdividing the monopole track into segments, such that the change in kinetic energy on one segment is 0.1%. A minimum and maximum segment length may be configured for the propagator module and were set to 0.1 m and 10 m.

5.3 Background Simulation

5.3.1 Cosmic Rays

The background of muons and muon bundles originating from CR interactions in the atmosphere is simulated with the independent software

CORSIKA (COsmic Ray Simulations for Kaskade) [149]. The software models the interaction of the primary CR particle with the atmosphere as well as the evolution and properties of the resulting shower of secondary particles.

Several models are available to describe hadronic interactions at high energies, though none is able to reproduce the data obtained from air shower measurements over the entire energy range [150, 151]. For this work the SIBYLL model [152] is used, which is known to predict less high energy muons than other models [153].

An important theoretical input for the simulation is the energy spectrum of the primary CR. Most simulations for IC40 are based on the polygonato (many knee) model [133], which describes the total spectrum as the sum of spectra from individual elements up to uranium ($Z = 92$). For an element with nuclear charge z the energy spectrum is given by a broken power-law

$$\frac{\mathrm{d}\Phi_z}{\mathrm{d}E_0} = \Phi_z^0 E_0^{\gamma_z} \left[1 + \left(\frac{E_0}{\hat{E}_z} \right)^{\epsilon_c} \right]^{\frac{\Delta\gamma}{\epsilon_c}} , \tag{5.1}$$

where the normalization Φ_z^0, spectral index γ_z and knee position $\hat{E}_z$ are specific for each element. The latter is assumed to scale with z as defined in Equation (4.2), with the proton-knee located at $\hat{E}_1 = 4.5\,\mathrm{PeV}$. The parameters $\Delta\gamma$ and ϵ_c, respectively characterize the change of the spectral index at the knee and the smoothness of the transition, are universal. Figure 5.2 shows the resulting spectrum along with measured data.

A complication arises from the fact that CORSIKA does not support the simulation of primary particles heavier than iron ($Z = 26$). Consequently, the CR flux at energies above 10^8 GeV, where trans-iron elements contribute significantly, is underestimated by the simulation. For most analyses not focused on exceptionally bright events this deficit is negligible. However, it poses a problem for this analysis since muon bundles from high energy CR appear most similar to magnetic monopoles and represent a critical background.

In order to accurately simulate the *all particle spectrum* at high energies with CORSIKA, an alternative model, that does not contain contributions from trans-iron elements, is required. The so-called *two-component* model uses only proton and iron primaries to represent light and heavy components [154]. The energy spectrum for each component is modeled by a broken power law, reflecting the general features of the CR spectrum (see

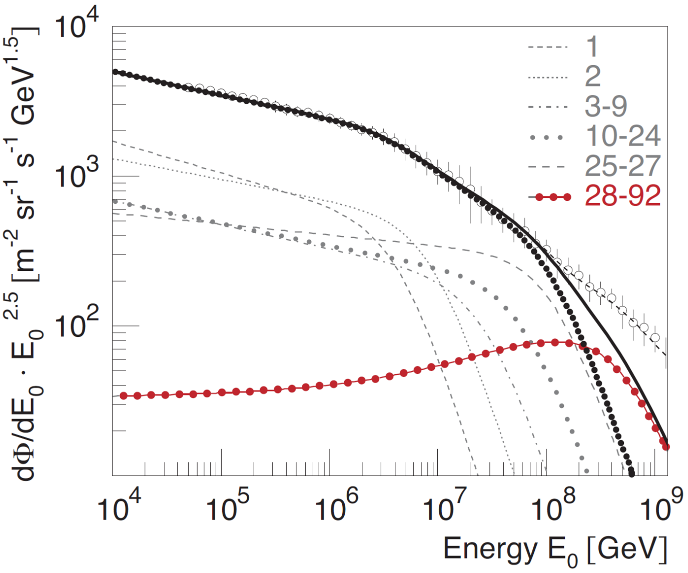

Figure 5.2: The poly-gonato model [133]. Open markers represent measured data of the all particle spectrum. The thick dotted line is the sum of all elements up to $Z = 27$ and the red dotted line the sum of all heavier elements.

Section 4.2.1). The open parameters of the model are the spectral indices below and above the knee, the position of the knee and the absolute flux for both components. The values for these parameters are obtained by fitting the model to air shower data measured by the KASCADE experiment [155] and summarized in Table 5.1.

Parameter	Proton	Iron
Normalization	$1.98 \cdot 10^4$	$1.07 \cdot 10^4$
E_{knee} [GeV]	$4.1 \cdot 10^6$	$1.1 \cdot 10^8$
γ_1	-2.67	-2.69
γ_2	-3.39	-3.1

Table 5.1: Spectral parameters for the two-component model [154]

The fitted proton iron spectra as well as the combined spectrum are shown in Figure 5.3 along with measured data. Since the iron knee is outside the KASCADE's fit region, only a single power law is obtained for this

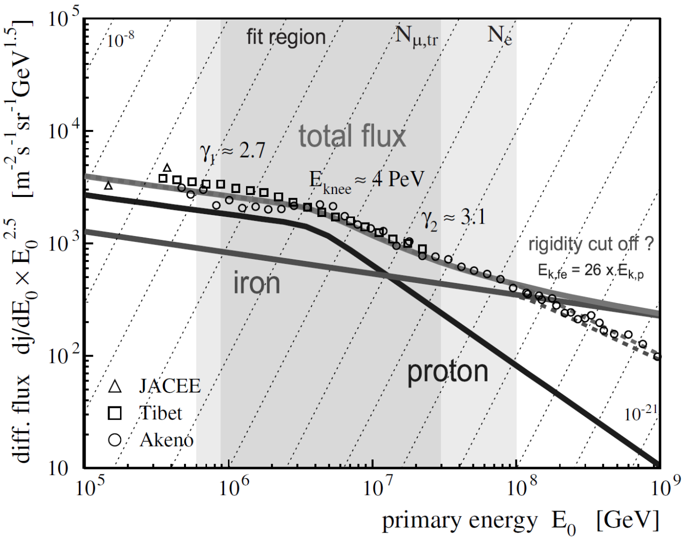

Figure 5.3: The two-component model. Shown are measured data (open markers) and the fitted proton and iron spectra (full lines). The gray shaded area indicates the fit region.

component. The position of the iron knee is therefore calculated using Equation (4.2) and the proton knee from the fit. The also unfitted spectral index above the iron knee is chosen such that the measured all particle spectrum at high energies is reproduce. Finally, a comparison of data simulated with the two-component and the poly-gonato model is shown in Figure 5.4.

During simulation, the primary CRs are sampled with energies between 10^4 and 10^{11} GeV from a E^{-2} spectrum. This oversampling yields better statistics for high energy event. The spectrum of the two-component model can be restored by appropriate weighting at the analysis level. The secondary muons resulting from the air shower are propagated through matter with the MMC (Muon Monte Carlo) software package [145]. MMC handles the continuous and stochastic energy loss of the muon. Stochastic losses from pair-production, bremsstrahlung, and photo-nuclear processes are recorded individually to later on determine the light output of each muon.

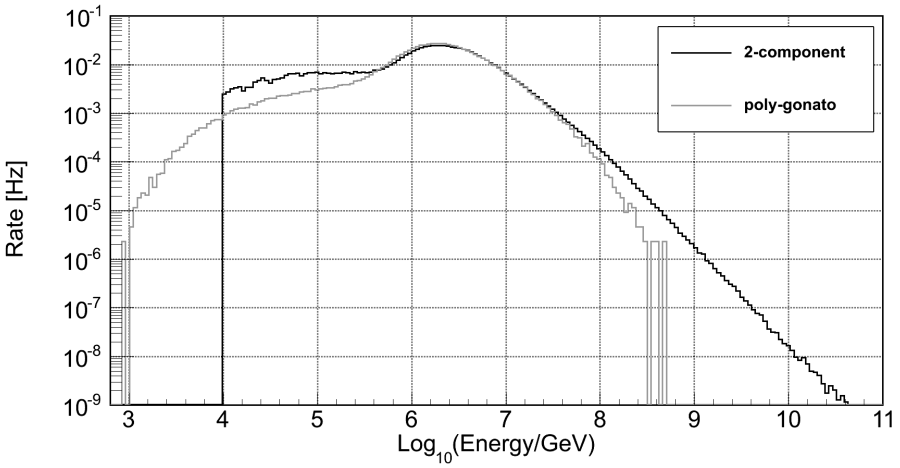

Figure 5.4: The muon spectrum at the EHE filter level (see Section 3.4.2) simulated with CORSIKA using the poly-gonato and the two-component model as input. At high energies the poly-gonato simulation predicts fewer events due to CORSIKA's inability to simulate elements heavier than iron and also has considerably less statistics compared to the two-component simulation. The difference at lower energies is due to the lack of intermediate elements in the two-component model.

5.3.2 Neutrinos

The neutrinos detected with IceCube may originate either from CR interactions in the atmosphere or astrophysical sources. The predicted energy spectrum for a given source is model dependent and can differ significantly between models. However, neutrino simulation for IceCube are usually produced with a generic energy spectrum. Any desired source spectrum can then be obtained by applying an appropriate weighting scheme. This allows to accommodate for the many possible spectra while conserving computing and data storing resources. Here, the models of Honda et al. [156] and Enberg et al. [157] are used for the conventional and prompt neutrino flux respectively. The energy spectra predicted by these models are shown in Figure 4.8.

The actual implementation of neutrino generation and interaction is provided by the NUGEN software package. Since the nature of neutrinos cross section makes a straightforward implementation prohibitively inefficient, a weighted Monte Carlo simulation is used instead. Each generated neutrino is forced to produce secondary lepton, which is then inserted in or near the detector. The probability of this actually happening is accounted for by an appropriate weight to the event. For muon neutrinos the resulting muons are passed to MMC and propagated further, whereas electrons from electron neutrinos are treated as point-like showers.

It should be noted that the NUGEN version used for IC40 simulations was found to be affected by a software bug which led to systematically higher rates. Since this applies to all datasets, the bug is considered an additional uncertainty and therefore handled in Chapter 8 with the other uncertainties.

5.3.3 Coincident Events

An additional class of background events that needs to be considered are so-called coincident events. They occur when the detector is triggered by two or more physical yet causally independent events in short succession so that DAQ combines them into one event. These events are especially prone to be mis-reconstructed since directions and locations of light generating particles are random.

The rate of coincident events depends on the length of the trigger window and the event rate of a given type. Hence, coincidences between atmospheric mouns are the most common type. Assuming a Poisson distribution for muon detection, the rate of two coincident muons is given by $R_c \approx \Delta t R^2$, where Δt is the length of the time window and R is the muon event rate [158]. In general, the fraction of events with n coincident muons is

$$f(n) = \frac{\Delta t^{n-1} R^{n-1}}{(n-1)!}. \tag{5.2}$$

At trigger level the fraction of two coincident events is of the order of 10^{-1} assuming $R \approx 1$ kHz and $\Delta t \approx 100$ µs.

Coincident events are simulated by merging several events with a single primary particle into on event. For coincident muons this is done by the *Polyplopia* module, which also calculates the corresponding probability weight of the merged event. The merging is done after each primary has been simulated separately up to the hit construction due to the way light propagation is simulated in IceCube (see Section 5.4). For IC40 detector several datasets with double and triple muon coincidences are available. These datasets were used in conjunction with the 2-component dataset, which contains only single events.

5.4 Light Simulation

The Cherenkov light generation and propagation in the ice is handled by so called *light injectors*. The light injectors available for IceCube either directly track all photons created by light emitting particle or use tabulated arrival time probabilities. While the latter approach suffers from drawbacks, such as binning artifacts and large memory requirements, it was used for most simulations including those with the IC40 geometry. Additionally, direct photon tracking for monopoles is often computationally impracticable due to the large number of photons involved. The light simulation for monopoles is thus also based on tables.

The probability tables are generated with the PHOTONICS software package [159], using a model of the south pole ice as input. The model describes the wavelength dependent optical properties of the ice assuming a structure of horizontal layers. Most of the available simulation data for the IC40 geometry uses the Additionally Heterogeneous Absorption (AHA) ice model [160], which is based on data taken in 2005 with the AMANDA-II detector [116]. This model is therefore also used for the monopole simulation. A more recent ice model, the South Pole ICE (SPICE) model [161], was used to study systematic uncertainties. The difference of these two models are shown in Figure 5.5. Since the Cherenkov angle for monopoles can be significantly different compared to muons, dedicated tables have been generated for each simulated monopole velocity. The straightforward implementation of monopoles as light sources into PHOTONICS is described in Reference [162]. During the simulation process, the tables are then accessed by the *HitMaker* module in order to determine the probability a DOM being hit by a photon depending on its relative position to the light source. The probability is then scaled with the absolute light yield and used as the mean value for the Poisson distribution from which the actual number of incident photons is sampled.

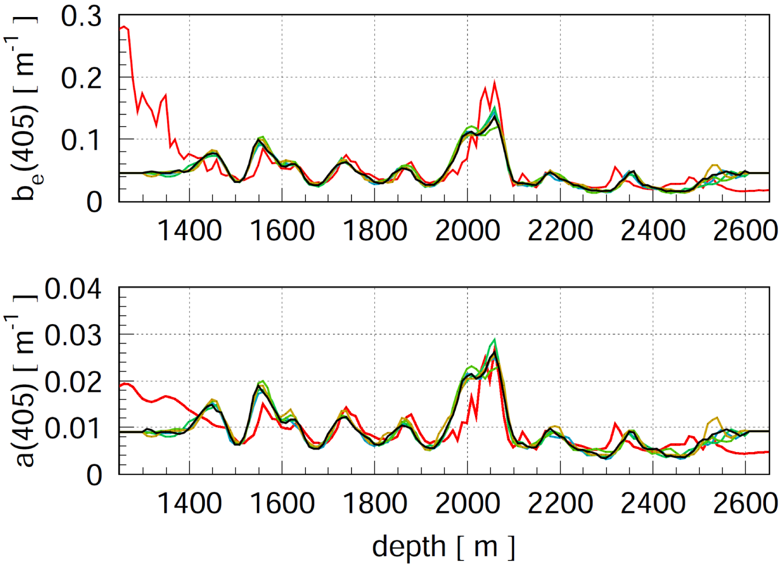

Figure 5.5: Comparison between SPICE (black line) and AHA (red line) [161]. The upper plot is an effective scattering length as functions of depth. The lower plot shows absorption coefficients. Also shown are uncertainties for the Spice model (green lines).

5.5 Detector Simulation

Once the number of incident photons, referred to as Monte Carlo hits (MChits), has been generated, noise hits are added by the *Noise-Generator* module. The noise generator simulates Poissonian noise either with a globally configured rate or using noise rate measurements for individual DOMs. A newer noise generator, that also accounts for non-Poissonian noise bursts, is currently under development. For this analysis a fixed noise rate of 650 Hz was used for all simulated data since individual noise rate measurements are not available for the 2008/2009 season.

The MChits, including noise, are passed to the *pmt-simulator* module, which applies the discriminator threshold and constructs a PMT output waveform. In the next step, the DOM main board response is simulated by the *DOMsimulator* module, which also accounts for the local coincidence logic. The result is a series of *DOM launches* containing the raw charges and digitized waveforms for the ATWD and PMT ADC channels. Finally, the trigger logic is simulated by various modules.

5.6 Burn Sample

Since a blind analysis relies on simulated data, it is necessary to verify that the simulation is accurate. This is done by comparing the simulated data to a small sample of experimental data. The data sample is thus *burned* and not used for the final analysis.

For this analysis, the experimental data sample consists of all "good runs" recorded during August 2008. The definition for a good run has been developed by the collaboration and is based on a set of basic data quality criteria such as a correct physics run configuration or stable rate during the run. This excludes data from test runs, LED flasher runs or very short runs. A list of good runs can be found in Reference [163]. The total sample used in this analysis has a live-time of $\sim$ 2601720 s $\approx$ 30 days, which corresponds to $\sim$ 8% of all available data taken with the IC40 detector. Figure 5.6 shows the event rates for the burned runs at the EHE filter level.

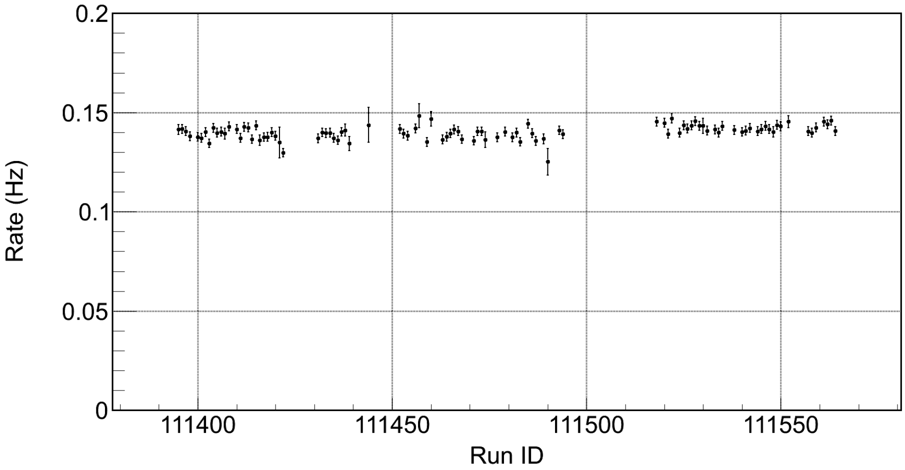

Figure 5.6: Event rates for all good runs in the burn sample. Note that gaps in the Run ID are not necessarily associated with equally large gaps in the data record since failed runs tend to be of short duration.

6 Cut Parameters and Reconstruction

Developing variables that can be used to distinguish signal (magnetic monopoles) and background (muon bundles and neutrino-induced leptons) has been a key task of this analysis. The final set of variables may be divided in two groups, furthermore called inclusive and exclusive variables. Inclusive variables utilize three unique features of magnetic monopoles: (1) Their brightness, (2) their potential to arrive from all directions and (3) their velocity, which may be significantly below the speed of light. On the other hand, exclusive variables are designed to identify certain types of background events, e.g. coincident events. This chapter summarizes the definitions of the variables used in the final analysis and the motivations behind them. The actual cuts and the order in which they are applied is described in Chapter 7.

6.1 Fundamental Data

The mapping of an event in the detector consists of the digitized waveforms recorded by the DOMs. However, the waveforms themselves are just of minor interest for most analysis purposes. Instead the number of photons and arrival times at the PMT are the basic information required to calculate higher-level variables and apply reconstruction algorithms. These information are contained in the waveforms convoluted with the response of the PMT and DOM electronics. In order to fully characterize an event it is thus necessary to extract relevant information from the waveforms.

6.1.1 Information Extraction

The first step to extract the desired information is to translate the signal recorded as a series of ATWD or PMT ADC counts to signals in voltage. This is done by the *DOMcalibrator* software module, which also corrects for known effects of the electronics like the droop of the transformer coupling PMT and DOM mainboard. After calibration is done the data is passed to a feature extraction algorithm, which may also calculate some waveform based observables. The extracted information usually consists of a series of so-called *RecoPulses* related to the detection single or multiple photo-electrons. Each pulse is described by its timing, charge and width as well as its spatial position determined by the DOM it is associated with. A similar but deprecated data type is the *RecoHit* that only contains timing information. The terms *pulse* and *hit* are used synonymously here but always refer to a RecoPulse.

PORTIA

The PORTable Impulse Analyzer (PORTIA) is a part of the EHE analysis framework, which aims at events with extremely high energies. Unlike other modules with similar purpose, PORTIA does not attempt to extract a pulse-based photon-count from the PMT output. The reason is that EHE waveforms are the result of a massive bulk of photo-electrons, which makes the extraction of single pulses difficult. The algorithm applied by PORTIA is therefore a simple integration of the ATWD and PMT ADC waveforms divided by a single charge. However, it should be noted that PORTIA has its own baseline subtraction algorithm, a task which is usually taken care of by the DOMcalibrator module. The waveforms used by PORTIA are therefore calibrated with this function disabled in the DOMcalibrator configuration.

PORTIA calculates both DOM- and event-wise observables like the number of photo-electrons. The event-wise NPE output is given separately for ATWD, PMT ADC and as a combined value. The latter is calculated by comparing the former two on a DOM by DOM basis and adding whichever value is larger to the sum. This *best* NPE combines the advantages of both channels, a large saturation point for the FADC and a wide time window for the PMT ADC. It is this value that is used by the EHE filter described in Section 3.4.2.

Feature-Extractor

Feature-Extractor is a software module designed to extract the arrival times of photons at the PMT contained in the captured waveforms. The procedure is only briefly summarized here. A more detailed description can be found in [164]. For the FADC output pulse extraction is done with a fast Bayesian unfolding method [165, 166]. The method assumes that the recorded waveform is a superposition of single photo-electron pulses with a typical pulse shape $S(t)$ for a photo-electron arriving at $t = 0$. The resulting waveform is then described by

$$F(t) = \int S(t - t')x(t')dt' \tag{6.1}$$

where

$$x(t) = \sum_{i=1}^{N} \delta(t - t_i) \tag{6.2}$$

is the searched for distribution of photo-electron arrival times. The iterative unfolding procedure starts with an arbitrary initial approximation for $x(t)$ and eventually converges to exact solution. The number of iterations is chosen high enough to ensure a sufficiently precise result and low enough to avoid instabilities due to noise in the waveform. The photon arrival time for each pulse is estimated by the intersection of a line fitted to the leading edge with the waveform baseline. The timing of all pulses is adjusted to either the timing of the first or largest pulse extracted with a more precise but slower method. Here, the first pulse was chosen. Similarly the pulse charges are rescaled to match the total charge found by the aforementioned method. Said charge is simply calculated as the sum of all waveform bins above a given threshold.

Pulse extraction from PMT ADC waveforms uses a different and vastly simplified method due to different design requirements and waveform properties. A pulse starts with the first waveform sample exceeding a given threshold. Starting from this sample, the pulse charge is computed as the sum of all bin values up to the sample in which the waveform falls below the threshold again. Pulse timing is again derived from the leading edge as described above.

6.1.2 Hit Selection

Not all hits recorded in an event contain useful information for reconstruction purposes and calculating cut variables. Especially bright events are likely to have a large fraction of hits originating from multiple scattered photons. Such hits tend to decrease the accuracy of the the reconstruction since the arrival times of scattered photons are delayed. Additionally, the probability that a recorded hit was caused by a scattered photon increases with the distance of the receiving DOM from the particle track. In order to mitigate such effects, hits must be selected with care for the intended purpose. Such a selection is necessarily different from standard selections, which are usually optimized for events featuring far less light than a monopole event.

The selection applied here actually starts even before hits are extracted from the waveforms. In a first step, data from DOMs, which are known to have spurious output, is removed. A list of problem DOMs can be found in Reference [167]. This *Launch Cleaning* also removes all but the first readouts from any DOM. Then a *Local Coincidence Cleaning* step selects only readouts that fulfill the HLC condition as described in Section 3.3.2. However, this is merely a precaution to ensure that the processed data conforms to the IC40 standard.

After pulse extraction has been executed using Feature-Extractor, the output is checked for pulses with negative charge, which may occur in case of spurious baselines. With these pulses removed, two sets of pulses are constructed as follows: (1) Select only the first pulse from each DOM and set its charge to the be the sum of all pulses from this DOM. (2) Starting from the previous selection, order the pulses by charge and select the topmost 10% of the sample (HC DOMs). These two selections are designed to fulfill the different requirements of the various cut parameters. The first selection provides a large statistic of hits for those variables that are based on the spatial distribution of hits. The second selection, on the other hand, is more suited for purposes where precise timing information is preferred.

6.2 Brightness

As shown in Section 2.5.2 relativistic magnetic monopoles are expected to generate large amounts of Cherenkov light. Thus the amount of light detected in an event is an important observable in order to identify a possible signal. A multitude of variables, which give a more or less accurate measure of amount of light, are available. A simple proxy, for example, is the number of DOMs that recorded a waveform or the number of photo-electrons mentioned in the previous Section. However, the absolute amount of detected light may vary depending on the orientation and spatial position of the primary particle track relative to the detector. For a track passing through the outer region of the instrumented volume less light will be detected compared to the same track passing through the center of the detector. Additionally, the amount of Cherenkov light generated by a monopole decreases rapidly as its velocity approaches the Cherenkov threshold (see Figure 4.1).

In order to mitigate such effects instead of the absolute brightness a measure of relative brightness is used. This measure is defined as the ratio of total number of photo-electrons in an event and the number of DOMs, which contributed to it. Both values are calculated by PORTIA using only waveforms from the PMT ADC digitizer channel. This choice was found to yield better signal to background ratio for very bright events compared to using the ATWD channel or the combined waveform. Since the number of DOMs (Nch) scales with the illuminated volume, the ratio is effectively a measure of the light density. A disadvantage of the light density is that it gives misleading results for small volumes i.e. few DOMs. Hence, before a cut on the light density can be attempted a pre-cut on the number of DOMs is made.

6.3 Direction and Velocity

Apart from brightness, two more distinctive observables for magnetic monopoles are the direction and the velocity. Monopoles have the potential to arrive from all directions, whereas the background arrives dominantly from above (see Chapter 4). Hence, knowing the direction of an event is critical for the background rejection. The velocity is of interest since monopoles can also travel large distances even at velocities significantly less than the speed of light. Muons at such velocities would be quickly decelerated below the Cherenkov threshold.

Direction and velocity of an event are reconstructed using a simple analytic algorithm termed *LineFit* (LF). The algorithm is based on the assumption that a particles passes through the detector as plane wave of light. The directional velocity v of a particle and its velocity is reconstructed by a least-square fit of the hypothesis to the measured data. In particular, given N hits at positions $\vec{x}_i$ and times t_i the optimization problem can be written as

$$\min_{t_0,\vec{x}_0,\vec{v}} \sum_{i=1}^{N} \rho_i(t_0,\vec{x}_0,\vec{v})^2 \tag{6.3}$$

where

$$\rho_i(t_0,\vec{x}_0,\vec{v}) = \|\vec{v}(t_i - t_0) + \vec{x}_0 - \vec{x}_i\|. \tag{6.4}$$

The position $\vec{x}_0$ of the particle at time t_0 is taken to be the average position and time of the hits reducing the problem to finding $\vec{v}$. The solution can then be calculated analytically [168]:

$$\vec{v} = \frac{\sum(\vec{x}_i - \vec{x}_0)(t_i - t_0)}{\sum(t_i - t_0)^2} \tag{6.5}$$

The assumption of a plane wave is not physically valid since in case of Cherenkov light the particle sits at the tip of a trailing light cone. However, it is a good approximation if the hits are close to the particle track. Hence, limiting the LineFit-reconstruction to the first pulse from each HC DOM, as described in Section 6.1.2, significantly improves the quality of the reconstruction. This is illustrated in Figure 6.1 showing the absolute difference between reconstructed and true zenith angle for both hit selections. The medians of the histograms are listed in Table 6.1.

Selection	atm. μ	atm. ν	$\beta = 0.995$	$\beta = 0.9$	$\beta = 0.8$	$\beta = 0.76$
All	2.1°	2.8°	6.9°	6.4°	5.2°	2.3°
HC	0.8°	1.3°	1.5°	1.4°	1.2°	0.8°

Table 6.1: Median deviation of the reconstructed zenith angle from the true value for signal and background simulation using different hit selections.

The hit selection also greatly improves the accuracy of the reconstructed velocity as shown in Figure 6.2. However, it was found that simulation and experimental data do not match well in the low velocity tail of the distribution as can be seen in Figure B.1 in the appendix. Since no clear cause for the discrepancy could be identified, the reconstructed velocity is only used as a minor cut variable to remove very slow events.

It should be noted that other analyses use the LineFit-reconstruction only as a first guess for more sophisticated likelihood based algorithms. However, these algorithms are usually particularly designed for relativistic

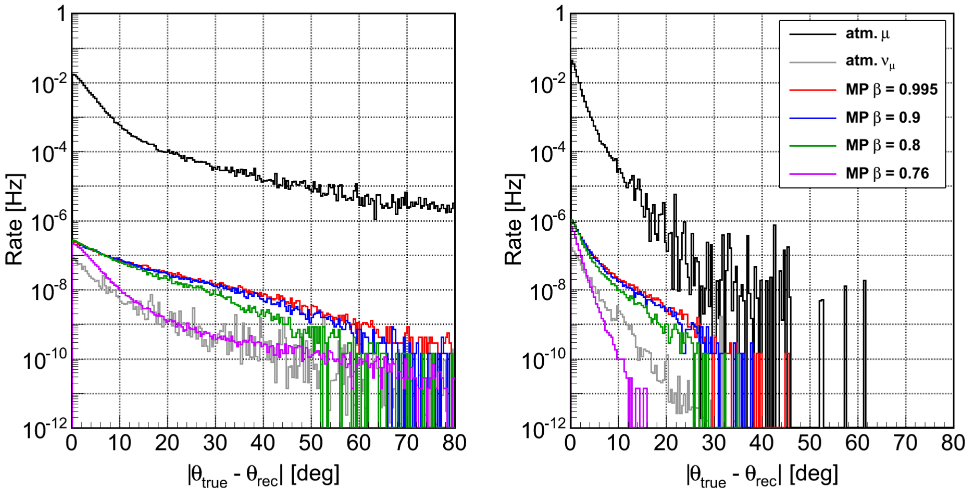

Figure 6.1: Absolute difference between true and reconstructed zenith angle. Left plot using no hit hit selection. Right plot using only the first from each HC DOM.

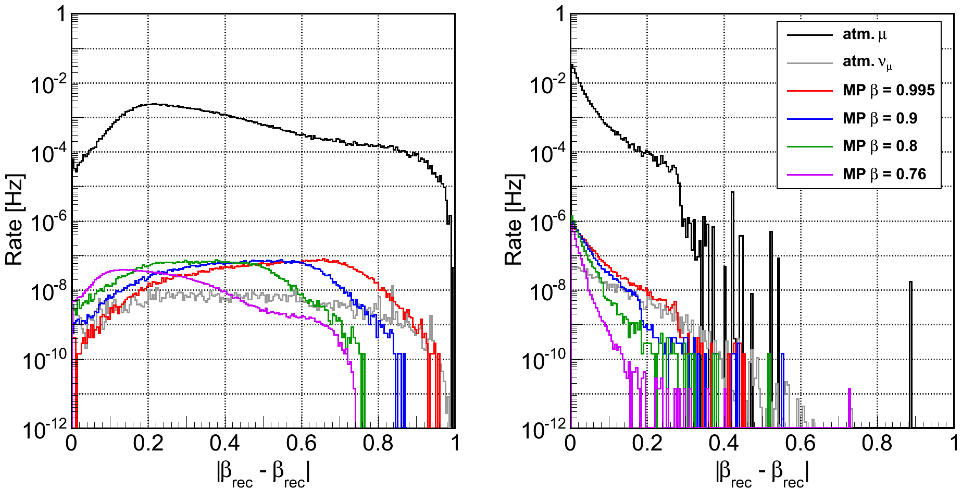

Figure 6.2: Same as Figure 6.1 for the absolute difference between true and reconstructed velocity.

muons in ice, e.g. by assuming a fixed Cherenkov angle of 40.7°. Adapting the likelihood approach for magnetic monopoles is not trivial due to the velocity dependence of the light emission. Additionally, the LineFit algorithm performs quite well for bright tracks with many hits while requiring only minimal resources. Lacking a better alternative, the LineFit was chosen for this analysis, though a better velocity reconstruction would be desirable.

6.4 Cascade Events

During the analysis it was found that some background events are characterized by a localized burst of light while being rather faint otherwise. Figure 6.3 shows an example event. These light burst can be the result of a catastrophic energy loss along a muon tracks initiating a hadronic cascade. As a result the DOMs that recorded the most photons are typically clustered closely in space and time. Since bright hits are favored by the hit selection described in Section 6.1.2, the data used for reconstruction will mostly consist of hit in one such cluster. The LineFit reconstruction then does not have a large enough lever arm to accurately determine the direction and velocity of the event.

Though the fraction of such cascade-like events is relatively small, they may not be caught the direction dependent cuts if they are wrongly reconstructed as up-going. Hence, the analysis applies two cuts on simple variables sensitive to these event class. The first variable is the number of strings over which the selected hits are distributed, which is a simple measure of the spatial extent. For a not to high energetic the number of string is expected to be small, indicating close proximity between the brightest DOMs. Additionally, enforcing a minimum number of string over which the DOMs must be distributed increases the lever arm and improves the general reconstruction quality. The second variable utilizes the time structure of a cascade and is defined as time interval between the first and last selected hit. Again, small values indicate a clustering of the brightest hits expected from a cascade.

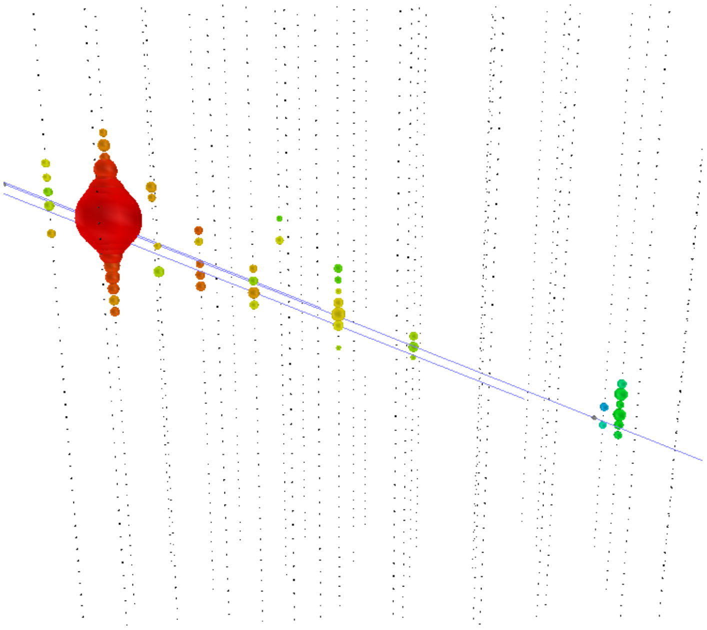

Figure 6.3: Example of a simulated event with a cascade component. The colored spheres indicate the timing (red = earlier, blue = later) and brightness (radius) of the signal for each DOM. Also shown are the true tracks (blue lines) of the most energetic muons of the event.

6.5 Coincident Events

As described in Section 5.3.3, coincident events are caused by two or more independent primary particles. Like cascade events, they are prone to misreconstruction, however not due to a short lever arm but the occurrence of causally and spatial distinct groups of hits. In order to discriminate coincident events, a so-called topological trigger algorithm, implemented in the *ttrigger* module, is used. This algorithm sorts the hits in an event into topologically connected sets, which ideally can be identified with different primary particles. The decision whether or not two hits are connected is based on three criteria:

1. Vertical distance less than z DOMs
2. Horizontal distance less than r meters
3. Deviation from the light cone less than t ns

The generated subsets are required to contain a minimum number of hits within a certain time window in order to avoid random grouping. All of the above parameters are configurable through the modules interface. The values used for this analysis are summarized in Table 6.2.

Parameter Name	Value	Description
Topo	1	Enable precise calculation
Multiplicity	5	Required multiplicity in a hit set
TimeWindow	4000 ns	Multiplicity time window in a hit set
TimeCone	450 ns	Max. deviation from t-r/c cone
ZDomDist	30	Max. separation between DOMs on same string
XYDist	300 m	Max. distance between neighboring strings

Table 6.2: Configuration of the Topological Trigger module. Options not listed here are set to default values.

The topological trigger is applied with the hit selection restricted to the first hit from each DOM (see Section 6.1.2). This choice was made for two reasons. First, restricting the hit selection to HC DOMs does not provide enough statistics for the algorithm to work properly. Second, pulses from photons arriving late at on particular DOM due to the stochastic nature of scattering may be wrongly allocated to a different hit group than earlier pulses. This is prevented by using only the first hit from each DOM. However, with the given parameter configuration the fraction of coincident events that are split at all is relatively small. Increasing this fraction by adjusting the parameters would also increase the fraction mistakenly split signal events. Hence, additional cuts need to be applied in order to further reduce the rate of coincident events, especially whose who are heavily mis-reconstructed.

The additional cuts are based on four conventional variables: (1) The reconstructed velocity, (2) the so-called no-hit fraction (NHF), (3) the size of the largest gap between hits along the reconstructed track g_{max} and (4) the lateral spread of hits around the track $d_{\perp}^{\mathsf{RMS}}$. The velocity is provided by the LineFit-reconstruction described in Section 6.3. For coincident events, it can be significantly slower than the speed of light depending on the timing of the involved primary particle tracks and their

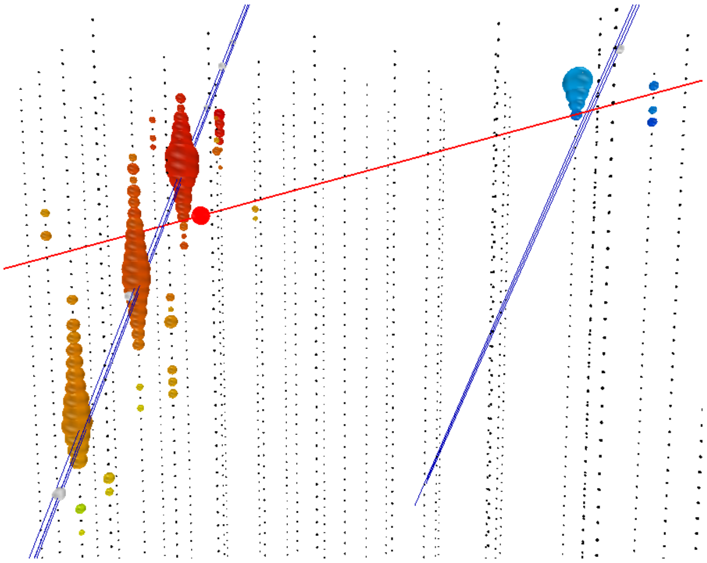

Figure 6.4: Example of a simulated coincident event. The true tracks of the muons are shown in blue, the erroneous reconstruction in red.

position in the detector. The track information from the LineFit is also used to calculate the other variables explained in the following.

The variables NHF, g_{max} and $d_{\perp}^{\mathsf{RMS}}$ all characterize the spatial distribution of hits relative to a given track hypothesis. They are motivated by the observation that for coincident events the reconstructed track is often misaligned relative to the hit positions and passes through regions of the detector where few or no light is recorded. An example event is shown in Figure 6.4. The variables can therefore be viewed as quality parameters of the reconstruction. The no-hit fraction is defined as

$$\mathsf{NHF}(r) = \frac{n_0(r)}{n_{\mathsf{tot}}(r)}, \tag{6.6}$$

where n_0 is the number of DOMs without a hit within a cylinder volume of radius r around the track and n_{tot} is total number of DOMs in the cylinder. For this analysis, a cylinder radius of 100 m was chosen. The lateral spread is calculated as the root mean square of the orthogonal distances of the hit DOMs to the reconstructed track using the recorded charges as weight. Unlike most other variables both the NHF and $d_{\perp}^{\mathsf{RMS}}$ are calculated without the restriction to HC DOMs. Otherwise the distribution of hits would be too sparse to provide meaningful results. Finally, g_{max} is defined as the largest distance between two consecutive hits, whose position has been projected orthogonally on the track. This variable is used in two variants calculated once for each of the two hit selections defined in Section 6.1.2.

7 Event Selection

The following chapter summarizes the event selection, developed in a blind fashion, and the adopted optimization methods. The cuts are grouped into several levels loosely based on similar function. Before the final cut level the dataset is divided in two subsamples. The reason and splitting condition are given in Section 7.6. The cuts are then applied to the experimental data, excluding the burn sample. The results of this *unblinding* process are described in Chapter 9. The absolute passing rates of signal and background events for each level can be found in Table 7.3 at the end of this chapter.

7.1 Optimization Methods

The task to chose experimental cuts in an unbiased way while trying to achieve an optimal result requires balancing of different boundary conditions. In the presence of a signal the goal is to maximize the significance, whereas in the case of no signal a high sensitivity is desired. In astrophysical searches the latter case is frequently encountered since they usually seek the confidence interval for the normalization of an otherwise known signal flux model. For this search the monopole flux spectrum is assumed to be flat and only the upper limit of the normalization is of considered. The sensitivity is then optimized with the *model rejection potential* (MRP) method [169], which is widely used by searches with neutrino telescopes.

The MRP technique attempts to find cuts that minimize the expected upper limit on a particle flux, that can be derived from an experiment in the absence of a true signal. For a given selection of cuts the upper limit is given by

$$\Phi_\alpha = \frac{\mu_\alpha(n_{\mathsf{obs}}, n_{\mathsf{bg}})}{n_{\mathsf{s}}} \Phi_0. \tag{7.1}$$

The index α represents the confidence level of the upper limit with $\alpha = 90\%$ for this analysis. The expected number of signal events n_{s} is derived from Monte Carlo and is proportional to the initially assumed signal flux Φ_0. Therefore Φ_α is independent of whichever initial flux is chosen. Here, a constant flux of 5×10^{-17} cm^{-2}sr^{-1}s^{-1} is used, roughly corresponding to the limit obtained by AMANDA [90]. Finally, $\mu_\alpha(n_{\mathsf{obs}}, n_{\mathsf{bg}})$ is the Feldman-Cousins upper limit[6] [170] of signal events in experiment expecting n_{bg} background events and observing n_{obs} events. The quotient $\mu_\alpha/n_{\mathsf{s}}$ is then called the Model Rejection Factor (MRF).

The optimal choice of cuts minimizes the MRF. However, μ_α depends on the observed number of events n_{obs}, which is not known until the experiment is performed. To asses the sensitivity in an unbiased fashion, $\mu_\alpha(n_{\mathsf{obs}}, n_{\mathsf{bg}})$ is replaced by an *average upper limit* prior to unblinding. The average is calculated from an ensemble of hypothetical experiments with no true signal and background expectation n_{bg} [170]. The average upper limit is then the sum of the upper limits from all possible experimental outcomes weighted by their Poisson probability:

$$\bar{\mu}_\alpha(n_{\mathsf{bg}}) = \sum_{n_{\mathsf{obs}}=0}^{\infty} \mu_\alpha(n_{\mathsf{obs}}, n_{\mathsf{bg}}) \frac{(n_{\mathsf{bg}})^{n_{\mathsf{obs}}}}{(n_{\mathsf{obs}})!} \exp(-n_{\mathsf{bg}}). \tag{7.2}$$

Figure 7.1 shows $\bar{\mu}(n_{\mathsf{bg}})$ for several different confidence levels. With this substitution Equation (7.1) yields the sensitivity, which only depends on the expected number of signal and background events.

Since n_{bg} can be determined with Monte Carlo methods, the cuts can be optimized prior to unblinding. However, the limit obtained with the unblinded data will be based on the actual number of observed events, which depends on how the background fluctuates. Still, the average upper limit allows to choose cuts, that yield the best limits averaged over multiple repetitions of the experiment.

Finding the minimum of the MRF becomes increasingly difficult as the number of involved cuts grows. Thus, the MRP technique is usually only applied to the final cut. The remaining cuts then need to be optimized with a different method. For this analysis, a method based on the cut efficiency, i.e. the fraction of signal events passing the cut, was chosen. For a particular cut, the goal is to minimize the background passing rate while keeping a minimum efficiency. The threshold commonly used here is 95%, though this value is somewhat arbitrary and is adjusted in places if the results justify it.

---

[6] Actually, it is the confidence interval, but the lower limit is usually neglected.

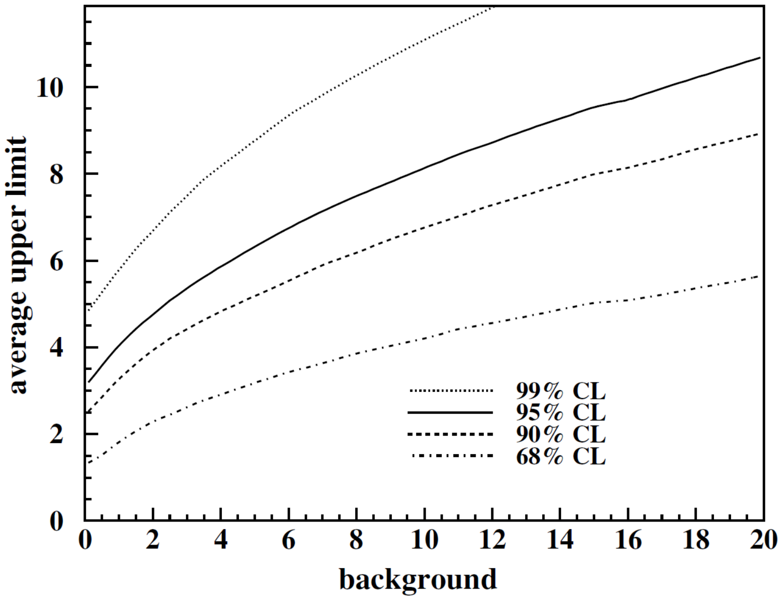

Figure 7.1: Feldman-Cousins average upper limit as a function of the expected number of background events for several confidence levels [169].

7.2 Level 0: Pre-Selection

The lowest level of the event selection is comprised of events passing the EHE filter criterion mentioned in Section 3.4.2. This pre-selection is based on the number of photo-electrons calculated by the PORTIA feature-extraction algorithm (see Section 6.1.1). The filter selects events with NPE $> 10^{2.8} \approx 630$. This allows for an reduction of the data volume by more than two orders of magnitude [138] while retaining the bright events that are of interest for this analysis. Though experimental data and simulated background already contain the NPE information, it was re-calculated for the event selection to ensure consistency with the simulated signal data. Figure 7.2 shows the NPE distribution at this level.

7.3 Level 1: Light Density Cut

The next step of the event selection is to reduce the data volume to a manageable level before proceeding with more resource intensive calculations.

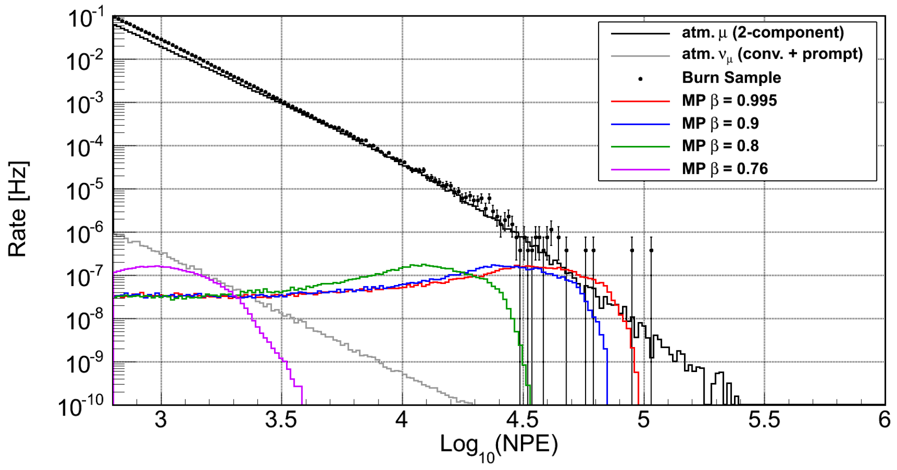

Figure 7.2: Distribution of the number of reconstructed photo-electrons at the EHE filter level. Shown are simulated signal (colors), simulated muon and neutrino background (black and gray) and measured data points from the burn sample.

Therefore only variables already calculated by the PORTIA module in the previous selection level are used here. Similar to the EHE filter, the cuts are based on the event brightness represented by the light density (LD) and Nch variables described in Section 6.2.

The cut conditions applied here are $\mathsf{Nch} \geq 60$ and $\mathsf{LD} \geq 8\ \mathsf{PE/DOM}$. The distribution of the light density before and after the Nch cut is shown in Figure 7.3, illustrating the necessity of the pre-cut. Both cut thresholds have been optimized with regard to the signal efficiency, as described in Section 7.1, with the Nch cut using the standard value of 95%. However, for the LD cut this condition would only result in a marginal reduction of the background, as can be seen in Figure 7.4. Instead, a threshold that simply halves the background rate after the Nch cut was chosen. This results in signal efficiency of $\sim 74\%$ for monopoles with $\beta = 0.76$ and close to 99% for all other simulated velocities. The relative passing rate for the whole level compared to the previous is about 35% for background and 70% – 95% for signal events.

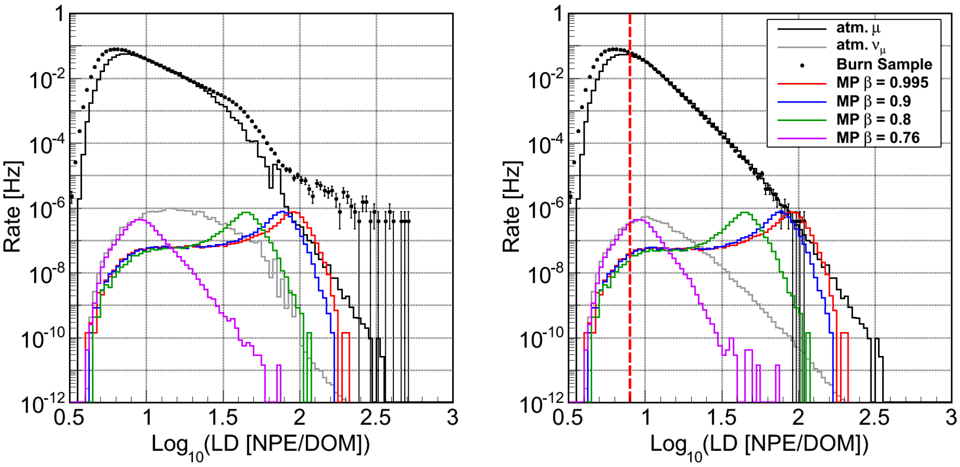

Figure 7.3: Distribution of the light density (NPE/Nch) variable. Left before and right after the Nch cut. The vertical red line in the left plot indicates the cut value for this variable.

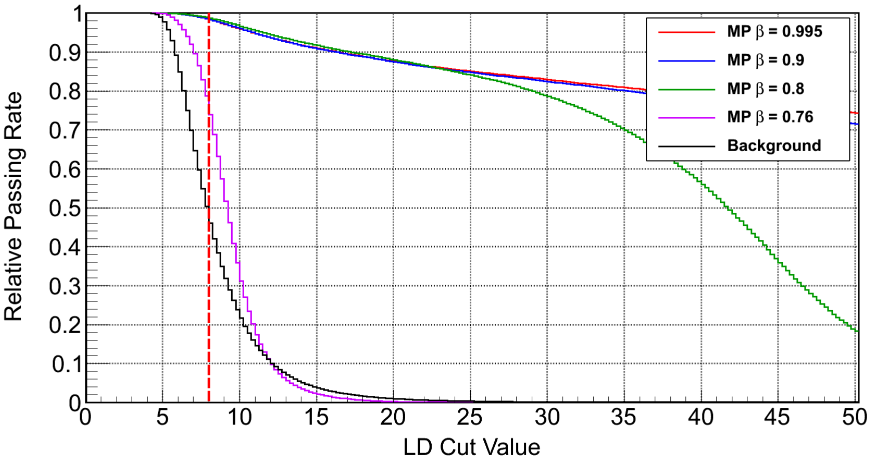

Figure 7.4: Relative passing rates for increasing values of the LD cut value. The red dashed line represents the value chosen for the analysis

7.4 Level 2: Cascade Events

The purpose of the cuts in this level is to remove events dominated by a cascade like burst of light, which are likely to lead to a poor reconstruction. These events can be discriminated by using the time range Δt of the event and number of strings n_{str} that recorded a hit as described in Section 6.4. Additionally, events with a low reconstructed velocity v_{LF} are removed at this level. This cut has some overlap with level 3 (see Section 7.5) since a low velocity may also be caused by a mis-reconstructed coincident event. However, mis-reconstructed cascade events appeared to be more frequent, so the cut is placed here.

The cut conditions for the three variables are

1. $v_{\mathsf{LF}} \geq 0.215$ m/ns $\approx 0.72c$,
2. $n_{\mathsf{str}} \geq 3$,
3. $\Delta t \geq 792$ ns,

which are applied in this order. Distributions for these variables can be found in Appendix B.1. All cuts are optimized in the order of their application with the velocity and time range cuts using the standard threshold of 95% signal efficiency. For the n_{str} cut this threshold results in a cut value of 2, which was found to be insufficient to suppress some cascade events. Considering the discrete nature of n_{str}, the cut value was increased to 3, allowing $> 80\%$ of the signal and $\sim 52\%$ of the background to pass.

7.5 Level 3: Coincident Events

Following the removal of cascade-like events in the previous cut level, this level is focused on coincident events. The first step is the application of the topological trigger to split the selected set of hits into causally distinct groups as described in Section 6.5. In principle, it would be possible to separately analyze these subsets in order to reduce the number of mistakenly split signal events. However, this occurs only for a small fraction ($< 1\%$) of the signal events. Hence, only events that are not split at all are kept in order to keep the event selection as simple as possible.

The above condition reduces the rate of coincident events by only about 24%. However, a strong suppression of the coincident background is not imperative here since most of it will be taken care of by the final cut level. Still, some problematic events escape the topological trigger and need to be removed by other cuts. Such events are typically characterized by a poor match between the hit pattern and the reconstructed track, that is quantified by several other variables defined in Section 6.5. Ultimately, the three following selection conditions are applied:

1. $\mathsf{NHF}_{100} < 0.784$
2. $d_{\perp}^{\mathsf{RMS}} > 110\ \mathrm{m} - \mathsf{NHF}_{100} \cdot 64\ \mathrm{m}$
3. $g_{\mathsf{max}} < 420\ \mathrm{m}$

All three cuts are again optimized using the 95% signal efficiency threshold. The cuts mostly remove extreme outliers from the distribution of each parameter. The corresponding plots can be found in Appendix B.2.

7.6 Level 4: Directional Cuts

The final cut level aims to remove the bulk of the remaining background, which is mostly downward going muon bundles, by applying cuts based on the reconstructed direction. However, at this point of the analysis the zenith distribution features a discrepancy between experimental and simulated data near the horizon as seen in Figure 7.5. Several issues, like the atmospheric neutrino flux or the uncertainty of the muon flux, have been investigated as potential causes of this discrepancy. Still, none of these candidates is able to reproduce the observed difference in rate.

7.6.1 Data Split

In the absence of a conclusive explanation for the discrepancy, the chosen approach was to isolate the problematic data and handle it separately. Since background events with a reconstructed direction close or below the horizon tend to have a low light density (see Appendix B.3), the data is split in two subsets based on this variable. The separation value was chosen to be $\log(\mathsf{LD}) = 1.5$. The discrepancy is then contained in the low light density (LLD) branch of the analysis, as shown in Figure 7.6. The LLD branch also contains the monopole signal with $\beta = 0.76$, whereas monopoles with $\beta \geqq 0.8$ are primarily found in the high light density

(HLD) branch. This allows to apply more restrictive cuts in order safely avoid the discrepancy without regard for most of the signal. The event rates for both branches are listed in Table 7.3.

7.6.2 Low Light Density Events

As mentioned above, the subset of events with $\mathsf{LD} \lesssim 31.6$ contains the monopole signal with the slowest simulated velocity as well as the majority of the atmospheric muon background. The original goal of this cut level was to remove the data-MC discrepancy observed in the zenith distribution with additional cuts and recombine the subsets before the final cuts are applied. Unfortunately, no viable way was found to achieve this. Therefore, it was decided to apply a hard cut on the reconstructed zenith direction, shown in Figure 7.7, to certainly avoid the discrepancy. The zenith cut is preceded by a reiteration of the event time range and g_{max} cuts with hardened threshold values which are shown in Appendix B.4.

The final selection conditions are

1. $\Delta t > 1400$ ns
2. $112 \text{ m} < g_{\mathsf{max}} < 261 \text{ m}$
3. $\cos\theta_{\mathsf{z}} < -0.2$

where θ_{z} is the reconstructed zenith angle. For the first to cuts the threshold values were determined with the usual optimization method. However, the threshold value for the zenith cut was chosen to be conservative without optimization.

No atmospheric muon events survive the above cuts. The only significant background originates from atmospheric muon neutrinos with an expected rate of 2.2 events per year. For monopoles with $\beta = 0.76$ the passing rate is 18 events per year (given the flux from Section 7.1) or about 27% relative to the previous cut level. Despite this significant reduction, the resulting sensitivity (see Section 7.7) is still an improvement over previous analyses.

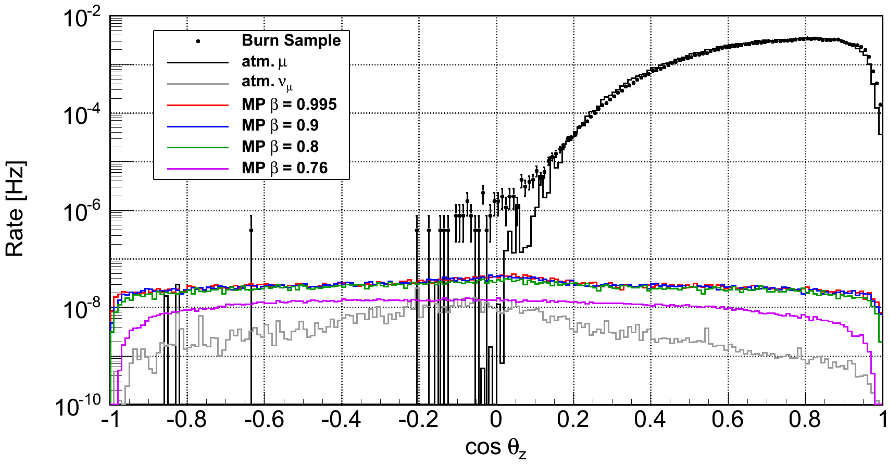

Figure 7.5: The reconstructed zenith angle for signal, background and burn sample. Around the horizon ($\cos\theta_z = 0$) the simulation underestimates the rate of atmospheric muon events.

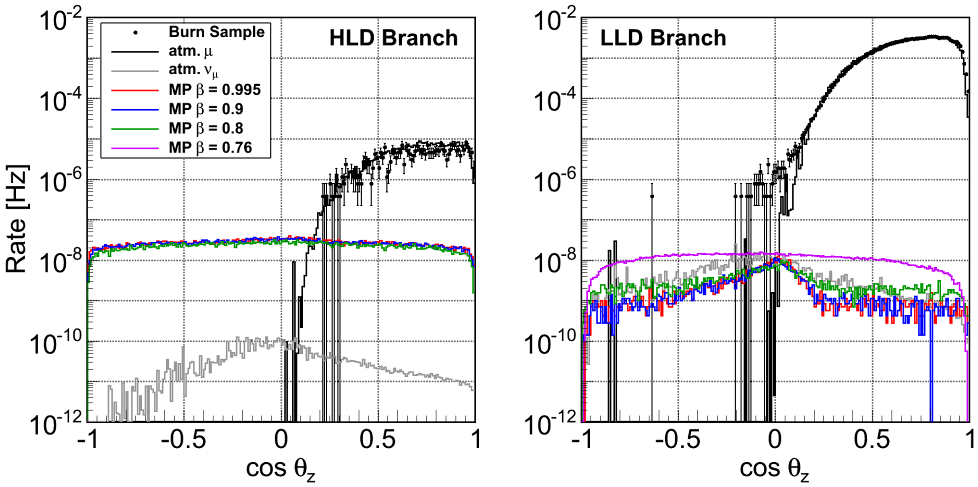

Figure 7.6: The reconstructed zenith angle for the HLD (left) and LLD (right) branch after splitting the data.

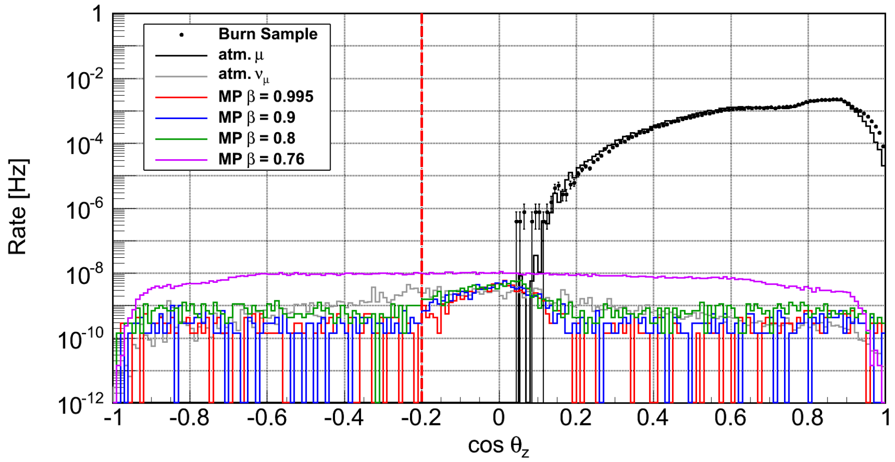

Figure 7.7: Final cut of the LLD branch. The cut value is marked by the dashed vertical line.

7.6.3 High Light Density Events

The subset of events with high light density is dominated by high energy atmospheric muon bundles. In order to remove this background, two-dimensional cuts in the θ_z versus LD and Δt plane are applied. Figures 7.8 and 7.9 show both distributions for signal and background. The cuts are divided in an up-going ($\cos\theta_\mathrm{z} < 0$) and down-going ($\cos\theta_\mathrm{z} \geq 0$) zenith angle range. For the down-going cases, LD and Δt spread to larger values the more vertical the event is. Hence, a cut threshold increasing linearly with $\cos\theta_\mathrm{z}$ is considered for this range. The up-going case, on the other hand, is mostly background free, so a straight cut with no zenith dependence is chosen. Both parts are joined at $\cos\theta_\mathrm{z} = 0$. The general cut condition can then be expressed in terms of a baseline for the up-going region and a slope for the down-going region:

$$\text{variable} > \begin{cases} \text{baseline} & \text{if } \cos\theta_\mathrm{z} < 0, \\ \text{baseline} + \text{slope} \cdot \cos\theta_\mathrm{z} & \text{if } \cos\theta_\mathrm{z} \geq 0 \end{cases}$$

with "variable" representing the light density or the time range.

In principle, the optimal values of the two baselines and slopes could be found by minimizing the model rejection factor, as described in Section

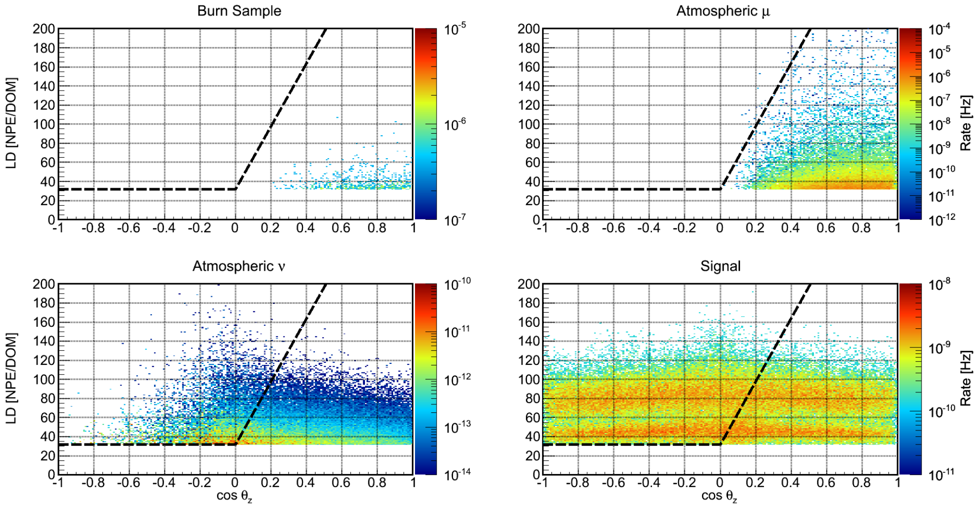

Figure 7.8: Final cut of the HLD branch in the $\cos\theta_\mathrm{z}$ vs LD plane.

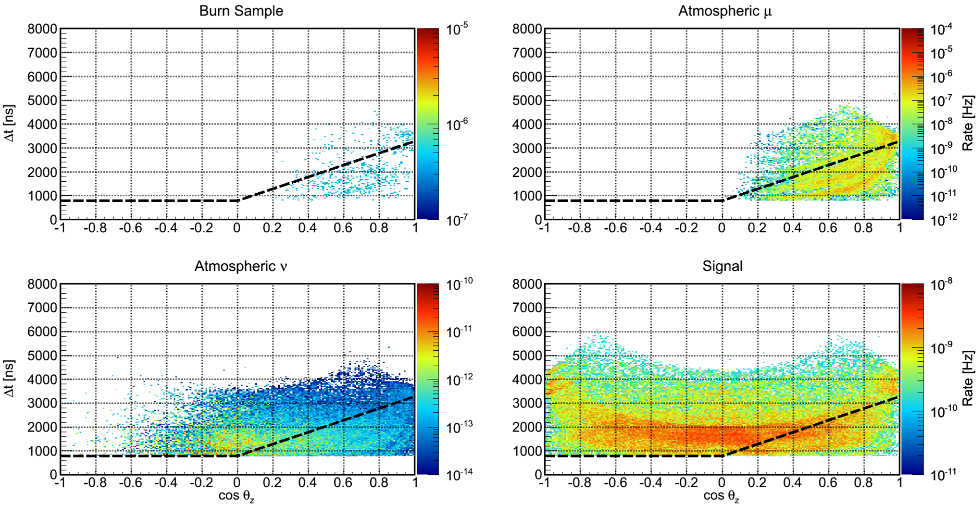

Figure 7.9: Final cut of the HLD branch in the $\cos\theta_\mathrm{z}$ vs Δt plane.

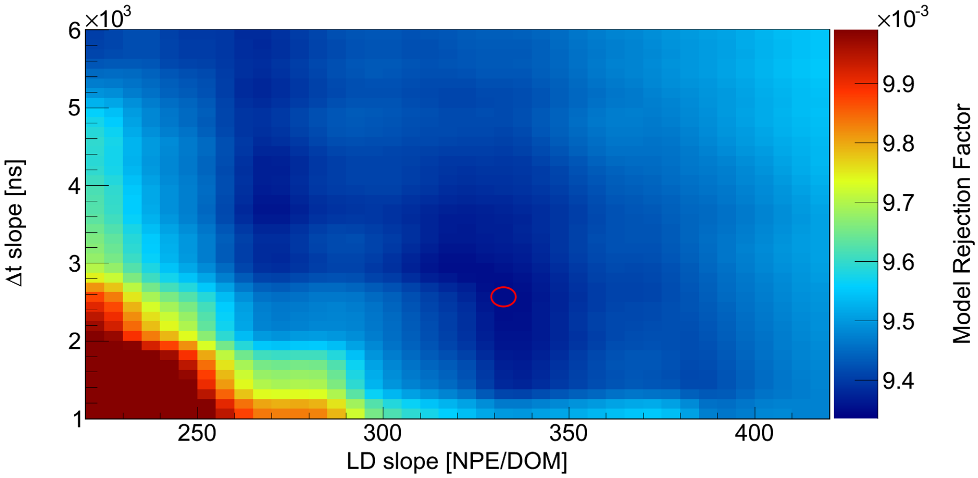

Figure 7.10: Model Rejection Factor scan for various values of the Δt and LD slopes in the final cut. The red circle marks the minimum.

7.1. This requires scanning a four dimensional parameter space, which is computationally resource intensive and difficult to visualize. Therefore, the number of free parameters is reduced by setting the LD baseline to the splitting threshold (~ 31.6) and the Δt baseline the value obtained in Section 7.4. This is equivalent to no cut at all for the up-going region and is motivated by the negligible background in this region. The MRF is then minimized by scanning the two-dimensional space of the slopes using both muon (two-component model) and neutrino (Honda2006/Sarcevic models) background as well as the combined signal data for $\beta \geq 0.8$. The parameters of the scan are listed in Table 7.1. The resulting MRF landscape shows no no distinct minimum due to statistical fluctuation. Therefore, an additional smoothing step is applied to the histogram which finally yields a stable minimum as seen in Figure 7.10. The final values of the cut parameters are then 2500 ns for the Δt slope and 330 NPE/DOM

Slope	Start	Stop	Step Width
LD [NPE/DOM]	220	420	5
Δt [ns]	1000	6000	125

Table 7.1: Parameters of the MRF scan

for the LD slope. With these values the final background rate is about 0.14 events per year predominantly from atmospheric neutrinos and a small contribution from atmospheric muons.

7.7 Sensitivity

The sensitivity defined in Section 7.1 is a measure of the effectiveness of an analysis. It is a function of the expected number of signal and background events. Since monopoles have been simulated with four different velocities in this analysis, each signal is treated separately. For monopole velocities $\beta = 0.995$, $\beta = 0.9$ and $\beta = 0.8$ the expected background from HLD branch is it contains the majority these signals. Conversely, for $\beta = 0.76$ only the background from the LLD branch is considered. The resulting sensitivities are listed in Table 7.2. Figure 7.11 displays this results relative to other experimental and theoretical limits.

	$\beta = 0.995$	$\beta = 0.9$	$\beta = 0.8$	$\beta = 0.76$
n_{s}	101.9	96.5	76.1	18.0
n_{bg}	0.14	0.14	0.14	2.18
$\bar{\mu}_{90\%}(n_{\mathsf{bg}})$	2.56	2.56	2.56	4.01
Sensitivity	$1.26 \cdot 10^{-18}$	$1.33 \cdot 10^{-18}$	$1.69 \cdot 10^{-18}$	$1.12 \cdot 10^{-17}$

Table 7.2: Sensitivity (in $\mathrm{cm}^{-2}\ \mathrm{s}^{-1}\ \mathrm{sr}^{-1}$) for each of the four signals. Also listed are the expected numbers of signal and background events for a full year as well as the average upper limit defined in Equation (7.2).

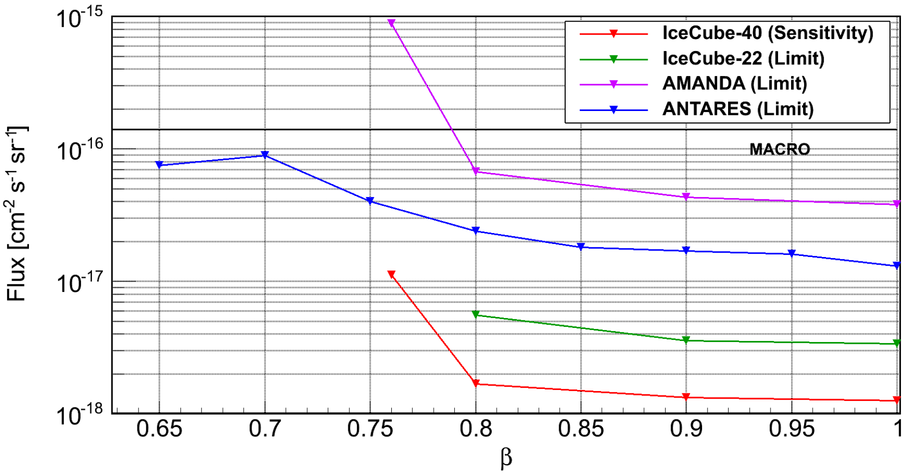

Figure 7.11: Sensitivity calculated for the four simulated monopole velocities (red triangles). Lines are meant to guide the eye. Also shown are limits from other experiments.

Data	Level 0	Level 1	Level 2	Level 3	Final	
					HLD	LLD
$\beta = 0.995$	270.2	256.4	188.8	182.5	101.9	0.6
$\beta = 0.9$	259.7	246.0	183.8	177.5	96.5	0.7
$\beta = 0.8$	231.5	218.4	164.9	159.5	76.1	1.7
$\beta = 0.76$	126.9	89.3	71.6	66.8	-	18.0
Burn Sample	$3.6 \cdot 10^7$	$1.0 \cdot 10^7$	$5.4 \cdot 10^6$	$4.4 \cdot 10^6$	-	-
Proton	$1.6 \cdot 10^7$	$4.9 \cdot 10^6$	$2.0 \cdot 10^6$	$1.6 \cdot 10^6$	$5.4 \cdot 10^{-4}$	-
Iron	$1.1 \cdot 10^7$	$4.9 \cdot 10^6$	$2.9 \cdot 10^6$	$2.6 \cdot 10^6$	$2.8 \cdot 10^{-2}$	-
Coincident μ	$4.0 \cdot 10^6$	$1.3 \cdot 10^6$	$6.9 \cdot 10^5$	$4.5 \cdot 10^5$	-	-
Conv. ν_μ	602.9	169.5	33.2	24.3	$7.2 \cdot 10^{-2}$	1.9
Prompt ν_μ	15.1	8.9	3.0	2.5	$4.0 \cdot 10^{-2}$	0.3
Conv. ν_e	39.6	6.9	$< 10^{-3}$	$< 10^{-3}$	$< 10^{-3}$	-
Prompt ν_e	11.6	6.1	$< 10^{-2}$	$< 10^{-2}$	$< 10^{-3}$	-
Total BG	$3.1 \cdot 10^7$	$1.1 \cdot 10^7$	$5.6 \cdot 10^6$	$4.6 \cdot 10^6$	$1.4 \cdot 10^{-1}$	2.2

Table 7.3: Rates of background and signal datasets (events/year) for each cut level

8 Systematic Uncertainties

The calculation of upper limits on the monopole flux is based on the expected number of signal and background events as described in Section 7.1. However, due to the blind approach of the analysis, these are derived from Monte Carlo simulations, which contain various kinds of uncertainties. One such uncertainty is the statistical error, which is caused by the finite number of simulated data samples and can be calculated exactly and calculated as the Pythagorean sum of the event weights. On the other hand, systematic uncertainties are usually known only approximately if at all. Systematic uncertainties can be roughly divided into experimental and theoretical uncertainties, arising from imperfect modeling of both aspects in the simulation. These uncertainties are therefore derived by varying certain parameters of the simulation one at a time and comparing the results. The total uncertainty for a given parameter is then conservatively estimated by the difference in final rates and the statistical uncertainty of this difference added linearly. For parameters where no data was available or could not be generated with reasonable effort numbers taken from publications and other analyses are used. The final values of all uncertainties considered for signal and background are summarized in Tables 8.2 and 8.3 at the end of this chapter. For the background only atmospheric muons and muon neutrinos are considered since the electron neutrino rate at the final cut level is negligible.

8.1 Experimental Uncertainties

The experimental uncertainties are a measure of how well the simulation describes the physical properties and hardware of the detector. Only two general parameters, the modeling of the polar ice and overall detection efficiency of the DOMs, are considered here since they are believed to be the largest factors.

8.1.1 DOM Efficiency

One major source of uncertainty is the so-called DOM efficiency, which is a global factor applied to the light yield for each DOM and related to the absolute energy scale of the detector. The uncertainty is typically studied using a ±10% variation of the nominal DOM efficiency. For the signal, datasets with 90%/110% efficiency were generated locally for each monopole velocity. However, for the atmospheric muon background no data with varied DOM efficiency was available. The relative uncertainty is thus taken to be ±35%, the maximum deviation quoted by a previous monopole analysis with the 22-string IceCube detector (IC22) [124]. The uncertainty for neutrinos was studied using a ±10% sample of muon neutrinos and taken to be the same for electron neutrinos.

8.1.2 Ice Model

The uncertainty of how light propagates through the detector is determined mainly by the optical properties of the ice. To estimate this uncertainty, simulations based on AHA and SPICE ice models (see Section 5.4) are compared here.

For the atmospheric muon (two-component model) background, data using the SPICE model was only available with 10% of the statistics compared to the AHA data. As a consequence, the number of events remaining after the final cut was insufficient to derive a reliable uncertainty of the estimate. Therefore, the event rates of the two datasets were compared at the next to last cut level, yielding a relative uncertainty of 8.7%, which is used for both the LLD and the HLD branch. While for neutrino datasets the SPICE data also has significantly less statistics than the AHA dataset, the (unweighted) number of events remaining after all cuts is still sufficient for a comparison. The relative uncertainties (including statistics) are then 34.9% and 20.4% for the LLD and HLD branch respectively.

For signal, the AHA simulations used for the development of the analysis were compared to additional SPICE data generated with dedicated PHOTONICS tables. These new datasets had the same statistics as the original ones. The resulting relative uncertainties are of the order of a few percent for all monopole velocities. This is attributed to the larger average brightness of monopoles mitigating the light absorption in the ice.

8.2 Theoretical Uncertainties

Several sources of theoretical uncertainties can be identified in the simulation of signal and background. For atmospheric muon bundles and neutrinos the major uncertainty arises from the modeling of particle interactions and the parametrization of the particle spectrum. The properties of magnetic monopoles depend on the underlying theoretical model and are therefore also uncertain to some degree. However, since the search for monopoles is the subject of this analysis, these uncertainties are not addressed here. Instead, conservative values have been chosen for properties like the magnetic charge, whereas others are given in terms of an accessible parameter space (see Section 4.1.2).

8.2.1 Normalization and Energy Spectrum

Muons

The largest theoretical uncertainty for atmospheric muons and neutrinos comes from the parametrization of the particle spectrum. For the two-component model used to simulate the muon background (see Section 5.3.1) the fitted parameters are given with one sigma uncertainties [154]. These values, summarized in Table 8.1, are used to construct the steepest/flattest possible spectrum and re-weight the simulated data. Since the knee position for iron was not fitted but estimated as $26 \cdot E^{\mathsf{p}}_{\mathrm{knee}}$, the parameter value is varied by the same relative amount as the proton knee position. The spectral index above the iron knee is conservatively varied to -2.7 (no knee) and -3.5 to keep the variation symmetric. For the uncertainty of the overall normalization a value of ±26% is taken from differential flux value at the knee energy. Since this is a separate estimate, the re-weighted data is renormalized to the same total rate at the EHE filter level (see Figure 8.1) and then compared at the final cut level.

The statistics of the spectra compared here are correlated since they are based on the same simulated data with different weighting. The statistical error on the difference between two rates R_{a} and R_{b} is then given by

$$\sigma = \sqrt{\sigma_{\mathsf{a}}^2 + \sigma_{\mathsf{b}}^2 - 2\sigma_{\mathsf{a}}^2\sigma_{\mathsf{b}}^2\rho_{\mathsf{ab}}} \qquad (8.1)$$

Parameter	Fit Value	Steep Spectrum	Flat Spectrum
$E^{\mathrm{p}}_{\mathrm{knee}}$ [GeV]	$4.1 \cdot 10^6$	$3.7 \cdot 10^6$	$4.5 \cdot 10^6$
γ^{p}_1	-2.67	-2.68	-2.66
γ^{p}_2	-3.39	-3.47	-3.31
$E^{\mathrm{Fe}}_{\mathrm{knee}}$ [GeV]	$1.1 \cdot 10^8$	$9.8 \cdot 10^7$	$1.2 \cdot 10^8$
γ^{Fe}_1	-2.69	-2.71	-2.67
γ^{Fe}_2	-3.1	-3.5	-2.7

Table 8.1: Variation of spectral parameters for the two-component model

where $\sigma_{\mathsf{a,b}}$ are the statistical uncertainties of the two rates and ρ_{ab} is the Pearson correlation coefficient. Since ρ_{ab} is not known, a value of 0 is chosen to get a conservative estimate of the uncertainty even though the real value is more likely close to one.

Whether the statistic are correlated or not the uncertainty on the spectral model parameters is the dominating factor of the total uncertainty for the HLD branch (see Table 8.3). At the final cut level all remaining events are in the energy range from 10^{10} GeV to highest simulated energy at 10^{11} GeV where the spectral models differ by a factor ~ 10. This reflects the limited understanding of cosmic rays at these energies, which also makes a conservative estimate of the uncertainty appropriate. Despite this, the absolute uncertainty of 0.3 events per year is actually rather small.

Neutrinos

The uncertainty of the neutrino energy spectrum is studied using the same approach used for muons, however, separately for conventional and prompt neutrinos. For the conventional component the Honda [156] and Bartol [171] models are compared and an uncertainty of $\sim 25\%$ on the normalization is taken from the Honda paper. For the prompt component the uncertainty is estimated by considering the minimum and maximum of the Enberg model [157].

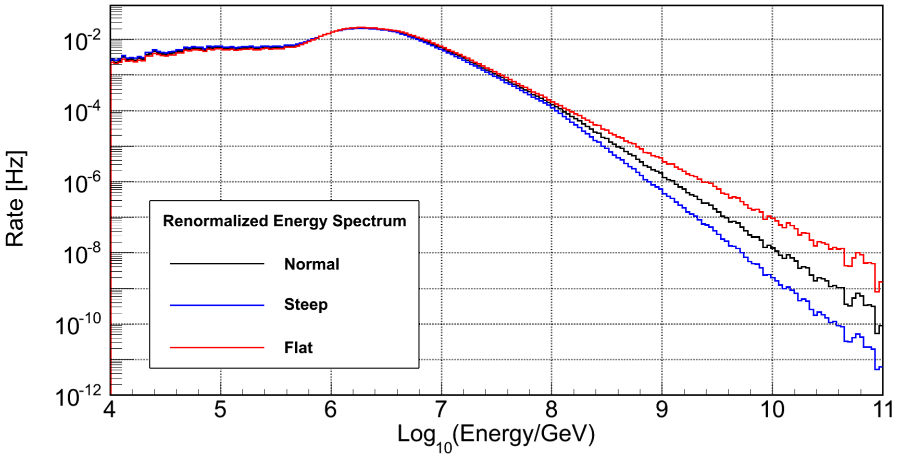

Figure 8.1: Variation of the muon energy spectrum derived from one sigma uncertainties of the model parameters. The spectra have been renormalized to the same total flux since the uncertainty of the normalization is handled separately.

8.2.2 Cross Sections

Another theoretical uncertainty stems from the cross section implemented in MMC and NUGEN (see Section 5.3), the latter only applying to neutrinos. Unfortunately, no data with varied MMC cross section were available for IC40. This uncertainty is therefore estimated by a ±10% value, which was chosen to match the largest deviation to one side quoted by the IC22 monopole analysis [124]. The value is used for both muon and neutrino background. An estimate on the uncertainty of NUGEN cross sections is taken from the IC40 ultra-high energy analysis [172] and set to 9.3%.

8.2.3 NUGEN Bug

The neutrino simulation for IC40 has been affected by a bug in the NUGEN software, as mentioned in Section 5.3.2. Studies of simulated data with the 59-string geometry have shown that due to the bug the overall neutrino rate is overestimated by about 10% [173]. Other changes to the simulation code made at the same time as the bug fix yield a further reduction by about the same amount. These software uncertainties, which may also affect the other neutrino uncertainties discussed before, are therefore estimated with a value of ±20%.

Uncertainty	$\beta = 0.995$	$\beta = 0.9$	$\beta = 0.8$	$\beta = 0.76$
DOM Efficiency	+4.2% -1.0%	+3.1% -3.6%	+3.7% -6.3%	+13.2% -16.4%
Ice Model	±3.8%	±3.4%	±4.6%	±6.8%
Statistical	±0.7%	±0.7%	±0.8%	±0.5%
Total	±5.7%	±4.7%	±6.0%	±17.8%

Table 8.2: Relative uncertainties for signal

	HLD			LLD
Uncertainty	atm. μ	atm. ν_μ	Total	atm. ν_μ
DOM Efficiency	$\pm 9.8 \cdot 10^{-3}$	$+2.2 \cdot 10^{-2}$ $-2.9 \cdot 10^{-2}$	$+2.4 \cdot 10^{-2}$ $-3.1 \cdot 10^{-2}$	$+3.4 \cdot 10^{-1}$ $-8.9 \cdot 10^{-1}$
Ice Model	$\pm 2.5 \cdot 10^{-3}$	$\pm 2.3 \cdot 10^{-2}$	$\pm 2.3 \cdot 10^{-2}$	$\pm 7.6 \cdot 10^{-1}$
Normalization	$\pm 7.3 \cdot 10^{-3}$	$\pm 1.8 \cdot 10^{-2}$	$\pm 1.8 \cdot 10^{-2}$	$\pm 4.7 \cdot 10^{-1}$
Spectrum	$+3.8 \cdot 10^{-1}$ $-3.4 \cdot 10^{-2}$	$+1.7 \cdot 10^{-2}$ $-1.3 \cdot 10^{-2}$	$+3.8 \cdot 10^{-1}$ $-3.6 \cdot 10^{-2}$	$+8.5 \cdot 10^{-2}$ $-1.2 \cdot 10^{-1}$
σ_{MMC}	$\pm 2.8 \cdot 10^{-3}$	$\pm 1.1 \cdot 10^{-2}$	$\pm 1.2 \cdot 10^{-2}$	$\pm 2.2 \cdot 10^{-1}$
σ_ν	N/A	$\pm 1.0 \cdot 10^{-2}$	$\pm 1.0 \cdot 10^{-2}$	$\pm 2.0 \cdot 10^{-1}$
Software	N/A	$\pm 2.2 \cdot 10^{-2}$	$\pm 2.2 \cdot 10^{-2}$	$\pm 4.4 \cdot 10^{-1}$
Statistical	$\pm 8.7 \cdot 10^{-3}$	$\pm 4.9 \cdot 10^{-3}$	$\pm 1.0 \cdot 10^{-2}$	$\pm 1.5 \cdot 10^{-1}$
Total			$\mathbf{\pm 3.8 \cdot 10^{-1}}$	$\mathbf{\pm 1.4}$

Table 8.3: Absolute uncertainties for background in (events/year)

9 Results

The final limits can in principle be calculated using Equation (7.1) once the experimental data has been unblinded and number of observed events is known. However, this approach neglects the systematic uncertainties associated with the measurements and assumes that the detector is exposed to an isotropic monopole flux at one of the four simulated velocities. This chapter is therefore divided in three parts: first, the results of the unblinding are summarized. Second, the incorporation of systematic uncertainties in the limit calculation is described. Third and last, the final limits at the detector and at the surface of the earth are derived.

9.1 Unblinding

The unblinded data sample consists of all "good runs" [163] recorded with the IC40 configuration in 2008/2009 excluding runs from August 2008, which have been used to verify the Monte Carlo simulations. This data sample has a total live-time of 29907504 s $\approx$ 346 days in 1423 runs. The individual event rates at the EHE filter level for all runs used in this analysis are shown in Figure 9.1.

After the unblinding three events remain in the final data sample: one in the LLD branch and two in the HLD branch. The two HLD events have sparked special interest since the expected number of background events for this branch is about one order of magnitude smaller. However, a more detailed analysis of the 3 events presented in Appendix A shows that none of them was likely caused by a magnetic monopole. However, without a better model for the background the final limits for this branch are calculated based on the background expectation from simulation. With 2 actually observed events this results in a higher yet conservative flux limit.

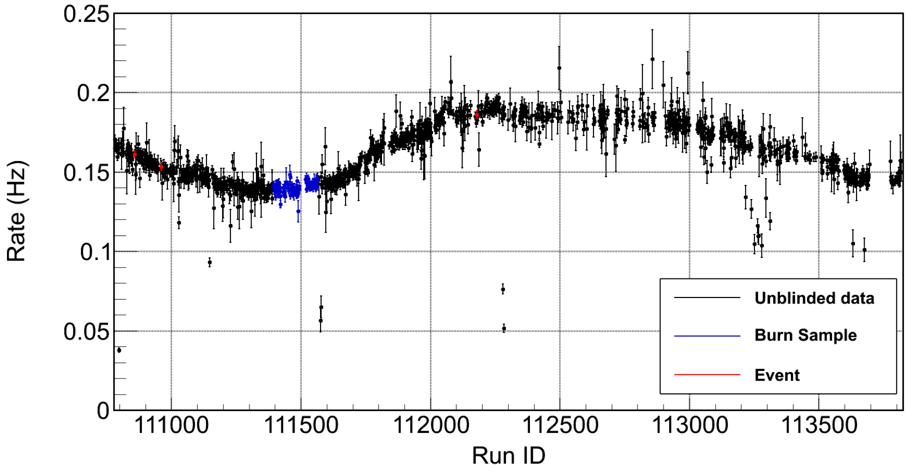

Figure 9.1: Event rates for all good data runs taken with IC40. Runs belonging to the Burn Sample are colored blue (compare Figure 5.6). Runs containing one of the remaining events are colored red. The periodic change of the average rate is due to seasonal variations of the atmosphere.

9.2 Inclusion of Systematic Uncertainties

In Section 7.1 the calculation of an average sensitivity for the analysis without prior knowledge of the number of observed events n_{obs} has been described. The essential Equation (7.2) can be seen as a way to incorporate an uncertainty associated with n_{obs}. For the calculation of the final flux limit this approach is extended to accommodate both the signal and background uncertainty.

In general, the upper limit on the flux is defined by Equation (7.1). Since n_{bg} and n_{s}, the quantities affected by uncertainty in this equation, represent independent factors, the inclusion of these uncertainties can also be handled separately:

$$\bar{\mu}_{90}(n_{\mathsf{obs}}) = \int \mu_{90}(n_{\mathsf{obs}}, n_{\mathsf{bg}}) \cdot \mathsf{PDF}(n_{\mathsf{bg}})\, dn_{\mathsf{bg}} \tag{9.1a}$$

$$\bar{n}_{\mathsf{s}} = \int n_{\mathsf{s}} \cdot \mathsf{PDF}(n_{\mathsf{s}})\, dn_{\mathsf{s}} \tag{9.1b}$$

where the two PDFs denotes the Probability Density Functions for the number of signal and background events and μ_{90} the Feldman-Cousins upper limit with 90% confidence level. Equation (9.1a) is analog to Equation (7.2) with the difference that now n_{bg} is varied. The final limit then follows from

$$\Phi_{90}(n_{\mathsf{obs}}) = \Phi_0 \cdot \frac{\bar{\mu}_{90}(n_{\mathsf{obs}})}{\bar{n}_{\mathsf{s}}} \tag{9.2}$$

where Φ_0 is again the initially assumed monopole flux.

The choice of the PDF is the crucial part of the limit calculation since it needs to contain all information about the signal (background) rate and the associated uncertainty. For this analysis the PDFs are expressed as

$$\mathsf{PDF}(n|\lambda, \sigma) = \int \frac{(\lambda + x)^n \, e^{-\lambda - x}}{n!} \cdot w(x|\sigma) \, dx. \tag{9.3}$$

This corresponds to a weighted average of Poisson distributions where the mean value varies around a central value λ with variance σ^2. Choosing a Poisson distribution mirrors the discrete process of selecting events. The resulting PDF is therefore actually a Probability Mass Function (PMF). The weighting function $w(x|\sigma)$, which describes the uncertainty, can only be hypothesized, though. Under the assumption that individual contributions to the uncertainty are symmetric and independent, a normal distribution with mean 0 and variance σ^2 would be the correct model. However, the Poisson distribution is only defined for positive mean values. Therefore a truncated normal distribution with the boundaries $-\lambda$ and $+\infty$ is used as the weighting function instead. Additionally, in case of the monopole simulation with velocities $\beta = 0.8$, 0.9 and 0.995 the Poisson distribution is approximated by a normal distribution for computational reasons. The final PMFs are shown in Figure 9.2.

With the above choices Equation (9.2) becomes

$$\begin{aligned} \Phi_{90}(n_{\mathsf{obs}}) = \Phi_0 \cdot & \sum_{n_{\mathsf{bg}}=0}^{\infty} \mu_{90}(n_{\mathsf{obs}}, n_{\mathsf{bg}}) \cdot \mathsf{PMF}(n_{\mathsf{bg}}|\lambda_{\mathsf{bg}}, \sigma_{\mathsf{bg}}) \\ & \cdot \left(\sum_{n_{\mathsf{s}}=0}^{\infty} n_{\mathsf{s}} \cdot \mathsf{PMF}(n_{\mathsf{s}}|\lambda_{\mathsf{s}}, \sigma_{\mathsf{s}}) \right)^{-1} \end{aligned} \tag{9.4}$$

where λ and σ for signal and background are set to the corresponding values obtained from simulations. The resulting upper limits on the magnetic

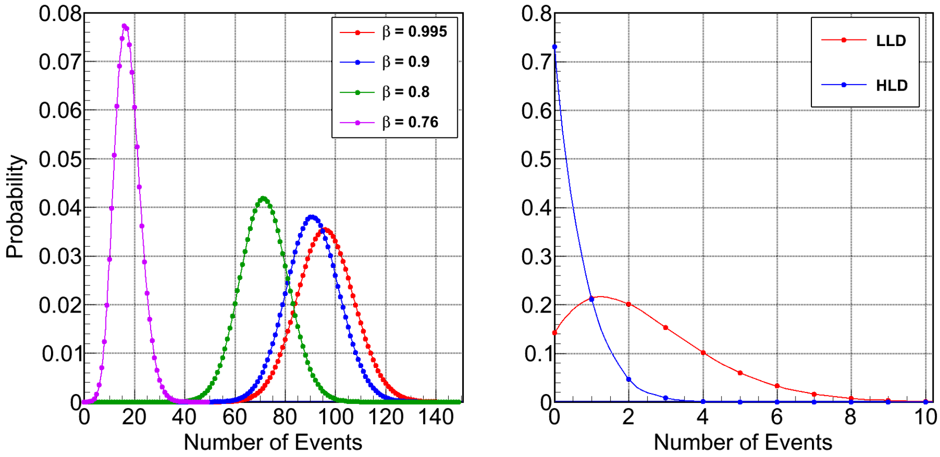

Figure 9.2: PMFs for the number of expected signal (left) and background (right) events due to statistical and systematic uncertainties. The actual values are marked by the colored circles. Lines are only drawn to guide the eye.

monopole flux for each simulated velocity can be found in Table 9.1. Also listed are the original limits from the IC22 analysis as well as recalculated values using the method described above. Finally, Figure 9.3 displays the results together with limits from other experiments.

	$\beta = 0.995$	$\beta = 0.9$	$\beta = 0.8$	$\beta = 0.76$
IC22 (original)	$3.38 \cdot 10^{18}$	$3.60 \cdot 10^{18}$	$5.57 \cdot 10^{18}$	$3.87 \cdot 10^{15}$
IC22 (recalculated)	$2.99 \cdot 10^{18}$	$3.19 \cdot 10^{18}$	$4.82 \cdot 10^{18}$	$2.74 \cdot 10^{15}$
This Analysis	$2.90 \cdot 10^{18}$	$3.06 \cdot 10^{18}$	$3.89 \cdot 10^{18}$	$7.73 \cdot 10^{18}$

Table 9.1: Flux limits (in cm^{-2} s^{-1} sr^{-1}) for each of the four signal velocities compared to the original from IC22.

For monopole velocities $\beta \geq 0.8$ the limits from this analysis are only a small improvement compared to the IC22 limits. The main reason for this are the two events observed in the HLD branch whereas IC22 has observed none. However, the IC22 results are based on a so-called a posteriori analysis. A first analysis made aggressive use of the reconstructed velocity, whose distribution was later found to be poorly understood in the tails. This lead to 12 event being found in the full data sample. The a posteriori analysis dropped the classification of events into speed bins and used improved background simulations to reassess several cuts. The new analysis was then applied to the full data sample and produced the results listed in Table 9.1. Since the results from this work do not include such a posteriori changes, they are less stringent but their derivation is more rigorous.

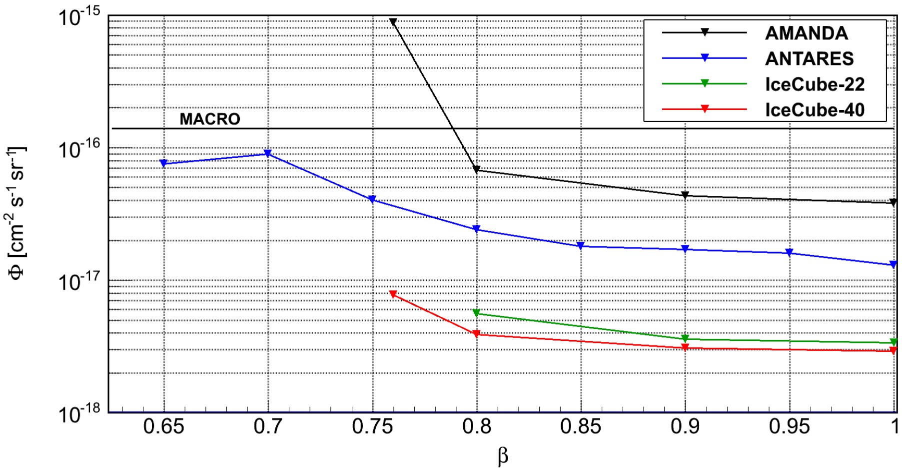

Figure 9.3: Final limits on the monopole flux for the simulated velocities (wedges) together with results from other experiments.

9.3 Flux Limits

The limits derived so far are valid for a particular monopole velocity β at the detector. However, as mentioned in Section 4.1.2, the free parameters of this search are the mass M and kinetic energy T of the monopoles. This section considers two cases of conversions between the $\Phi(\beta)$ and $\Phi(M, T)$: A time-independent monopole flux, which is isotropic either at the detector or the surface of the Earth. In each case, flux limits are calculated for pairs of (T,M) ranging from 10^4 to 10^{18} in units of GeV and GeV$/c^2$ respectively.

9.3.1 Flux Limits at the Detector

If the considered monopole flux is isotropic at the detector, the conversion between $\Phi(\beta)$ and $\Phi_{\mathsf{det}}(T, M)$ is straightforward since β can easily be expressed in terms of M and T:

$$\beta(T, M) = \frac{\sqrt{2TMc^2 + T^2}}{T + Mc^2} \tag{9.5}$$

However, $\Phi(\beta)$ is only known for discrete values of β, which prevents an exact mapping of (T, M) values belonging to intermediate velocities. A conservative approach is therefore to use a step function for the conversion:

$$\Phi_{\mathsf{det}}(T, M) = \begin{cases} \Phi(\beta = 0.995) & \text{if } 0.995 < \beta(T, M) \\ \Phi(\beta = 0.9) & \text{if } 0.9 < \beta(T, M) < 0.995 \\ \Phi(\beta = 0.8) & \text{if } 0.8 < \beta(T, M) < 0.9 \\ \Phi(\beta = 0.76) & \text{if } 0.76 < \beta(T, M) < 0.8 \\ 0 & \text{if } \beta(T, M) < 0.76 \end{cases} \tag{9.6}$$

Figure 9.4 shows the resulting limits in the (M, T)-plane along with limits from other experiments.

9.3.2 Flux Limits at the Earth's Surface

The limits at the detector are only physically valid if the energy distribution of the monopoles is independent of the arrival direction. While a flux of relic monopoles is indeed believed to be isotropic, the energy loss a monopole will experience as it travels the Earth will modify the flux seen by any detector. Determining flux limits at the Earth's surface therefore grants a more realistic view. The calculation presented here is roughly analog to the on in Reference [124].

The flux limit for a given zenith angle θ can be written as

$$\Phi_{\mathsf{surf}}(T_{\mathsf{s}}, M, \cos\theta) = \Phi_{\mathsf{det}}(T_{\mathsf{d}}, M) \cdot p^{T_{\mathsf{s}} \to T_{\mathsf{d}}}(M, \cos\theta) \cdot \epsilon(T_{\mathsf{d}}, T_{\mathsf{s}}, M, \cos\theta) \tag{9.7}$$

where T_{s} and T_{d} are the kinetic energies at surface and at the detector. The function $p^{T_{\mathsf{s}} \to T_{\mathsf{d}}}(M, \cos\theta)$ represents the probability that a monopole with initial kinetic energy T_{s} reaches the detector with energy T_{d} after

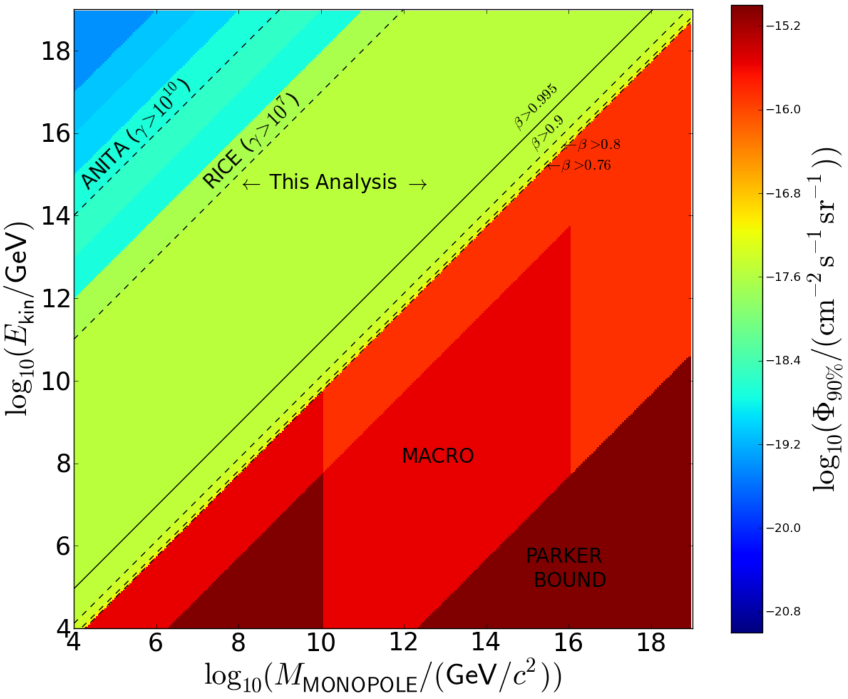

Figure 9.4: Final flux limits for different combinations of monopole mass and kinetic energy. The limits apply to an isotropic flux just outside the IceCube detector.

passing through the Earth. Naturally, this value depends on the monopole mass and the path length in the Earth associated with the arrival direction. Neglecting energy loss straggling, the average energy loss ΔE in the Earth is calculated for a bin width of 0.1 in $\cos\theta$ as described in Section 4.1.2. The kinetic energy at the surface is then given by $T_{\mathsf{d}} + \Delta E$ and the probability $p^{T_{\mathsf{s}} \to T_{\mathsf{d}}}$ is simply a delta function.

The factor ϵ in Equation (9.7) accounts for the fact that the upper limits at the detector and at the surface follow from Equation (7.1) as

$$\Phi_{\mathsf{surf}} = \frac{\mu}{n_{\mathsf{s}}^{\mathsf{surf}}} \Phi_0 \tag{9.8a}$$

$$\Phi_{\mathsf{det}} = \frac{\mu}{n_{\mathsf{s}}^{\mathsf{det}}} \Phi_0 \tag{9.8b}$$

where $n_{\mathsf{s}}^{\mathsf{surf}}$ and $n_{\mathsf{s}}^{\mathsf{det}}$ are the expected number of signal events at the surface and the detector respectively. Thus ϵ is given by

$$\epsilon = \frac{n_{\mathsf{s}}^{\mathsf{det}}}{n_{\mathsf{s}}^{\mathsf{surf}}}. \tag{9.9}$$

The number of signal events can be generally written as

$$n_{\mathsf{s}}(T, M, \cos\theta) = T_{\mathsf{live}} \cdot \Phi_0 \cdot A_{\mathsf{gen}} \cdot \int \frac{n_{\mathsf{det}}}{n_{\mathsf{gen}}}(T, M, \cos\theta)\, d\Omega \tag{9.10}$$

with $T_{\mathsf{live}} = 29907504\,\mathrm{s}$ the observed time interval, $A_{\mathsf{gen}} = 2.27\,\mathrm{km}^2$ the generation area of the simulation and $n_{\mathsf{det}}/n_{\mathsf{gen}}$ the fraction of generated monopoles remaining after all cuts. The $n_{\mathsf{det}}/n_{\mathsf{gen}}$ fraction is known for the four simulated monopole velocities with the same 0.1 bins in $\cos\theta$ as for ΔE above. The number of generated monopoles for each bin is approximated by the total number of generated monopoles divided by the number of bins. This *detection efficiency* is illustrated in Figure 9.5. Numerical values can be found in Appendix C.

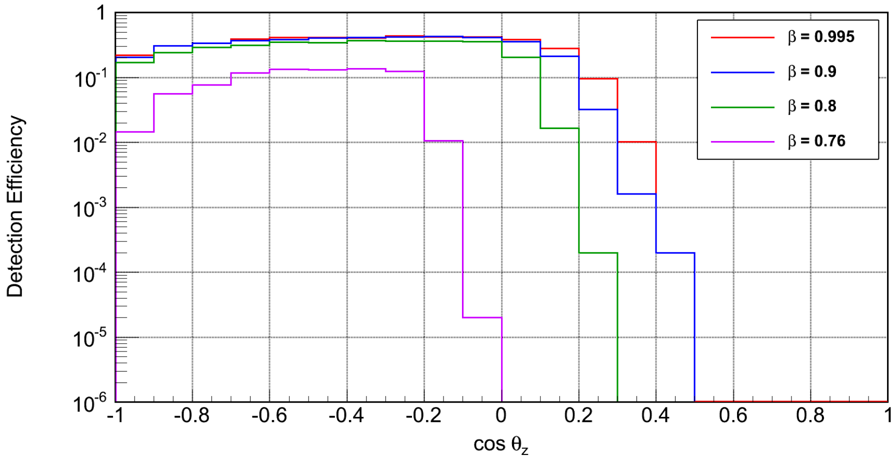

Figure 9.5: The detection efficiency of the final cuts for each of the four signal velocities.

In order to arrive at a limit that only depends on the monopole mass and kinetic energy the integrations in Equation (9.10) have to be carried out over the full solid angle Ω. Since the simulated flux is isotropic at the detector, $n_{\mathsf{s}}^{\mathsf{det}}$ becomes

$$\begin{aligned} n_{\mathsf{s}}^{\mathsf{det}}(T_{\mathsf{d}}, M) &= T_{\mathsf{live}} \cdot \Phi_0 \cdot A_{\mathsf{gen}} \cdot 2\pi \cdot \int_{1}^{-1} \frac{n_{\mathsf{det}}}{n_{\mathsf{gen}}}(T_{\mathsf{d}}, M, \cos\theta)\, d(\cos\theta) \\ &= T_{\mathsf{live}} \cdot \Phi_0 \cdot A_{\mathsf{gen}} \cdot 2\pi \cdot 2 \cdot \frac{n_{\mathsf{det}}^{\mathsf{tot}}}{n_{\mathsf{gen}}^{\mathsf{tot}}}(T, M). \end{aligned} \tag{9.11}$$

The final integral produces the total number of events generated and detected with a factor of 2 representing the integral over $d(\cos\theta)$. The conversion of the detection efficiency from a function of β to a function of T and M is done by a step function analog to Equation (9.6). The main difference for $n_{\mathsf{s}}^{\mathsf{surf}}$ is that the delta function in Equation (9.7) could pick out detection efficiency values from different velocities for different angles. The integration is therefore carried out as a summation over the 0.1 $\cos\theta$ bins:

$$n_{\mathsf{s}}^{\mathsf{surf}}(T_{\mathsf{s}}, M) = T_{\mathsf{live}} \cdot \Phi_0 \cdot A_{\mathsf{gen}} \cdot 2\pi \cdot \sum_{i=1}^{20} \Delta(\cos\theta)_i \cdot \frac{n_{\mathsf{det}}}{n_{\mathsf{det}}}(\cos\theta_i) \tag{9.12}$$

where $\frac{n_{\mathsf{det}}}{n_{\mathsf{det}}}(\cos\theta_i)$ is calculated for the largest simulated velocity that is smaller than $\beta(T_{\mathsf{s}} - \Delta E, M)$. Substituting Equations (9.11) and (9.12) in Equation (9.9) finally yields:

$$\epsilon = 2 \cdot \frac{n_{\mathsf{det}}^{\mathsf{tot}}}{n_{\mathsf{gen}}^{\mathsf{tot}}} \cdot \left(\sum_{i=1}^{20} \Delta(\cos\theta)_i \cdot \frac{n_{\mathsf{det}}}{n_{\mathsf{det}}}(\cos\theta_i) \right)^{-1} \tag{9.13}$$

Unfortunately, Φ_{det} and $n_{\mathsf{s}}^{\mathsf{det}}$ are also different for each velocity. In order to remain conservative, for each value of (T_{s}, M) considered, the largest value of $\Phi_{\mathsf{det}} \cdot n_{\mathsf{s}}^{\mathsf{det}}$ from any velocity used in the calculation of $n_{\mathsf{s}}^{\mathsf{surf}}$ is taken as the only value.

The final limits are shown in Figure 9.6. The shape of the regions with the same limit value reflects that of the constrained parameter space from Section 4.1.2. For low values of T and M the detector looses acceptance due to shielding by the Earth causing the limit to get worse. For monopole masses $\gtrsim 10^7$ GeV/c^2 and kinetic energies $\gtrsim 10^{11}$ GeV the Earth can not noticeably decelerate the monopoles, thus yielding the largest acceptance and the best limits.

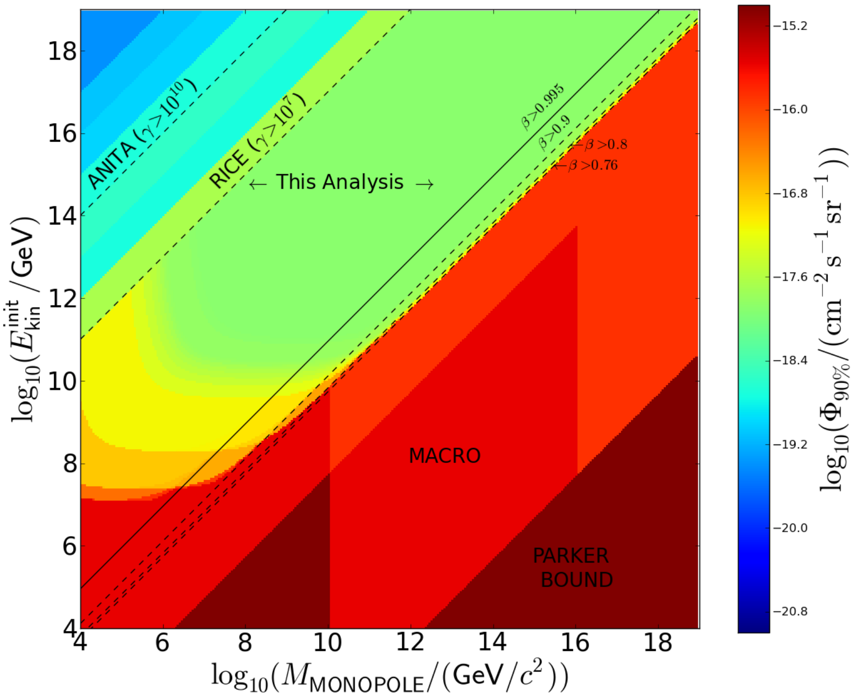

Figure 9.6: Final flux limits for different combinations of monopole mass and initial kinetic energy. The limits apply to an isotropic flux at the surface of the Earth.

10 Summary and Conclusion

This thesis describes the search for relativistic magnetic monopoles with the IceCube neutrino telescope. The existence of magnetic monopoles is a general prediction of grand unified theories. Depending on the choice of unification model, monopoles have predicted masses between 10^7 and 10^{17} GeV/c^2. Therefore, monopoles may have been created only in the early Universe at the time the unified symmetry was spontaneously broken. Due to their topological nature, such monopoles are stable and may have persisted until today.

During the lifetime of the Universe, chance encounters with large scale magnetic fields in the cosmos can accelerate magnetic monopoles. Current models of such galactic and extragalactic fields indicate that monopoles with masses up to 10^1 GeV/c^2 can reach relativistic velocities. This allows monopoles to be detected in neutrino telescopes like IceCube due to the Cherenkov light that they emit. Additionally, observations of the galactic magnetic field yield the Parker bound, the currently most stringent, model-independent limits on the monopole flux of 10^{-15} $\mathrm{cm}^{-2}\mathrm{sr}^{-1}\mathrm{s}^{-1}$.

Searches for relativistic monopoles have been performed with IceCube's predecessor AMANDA as well as the partially completed IceCube detector with 22 string. This work continues and improves the latter using data taken with the half completed, 40 string IceCube detector. The larger detector volume and adapted analysis methods allow to increase the sensitivity by about a factor of about 3 for monopole velocities $\geq 0.76c$. This is mainly achieved by an increased acceptance for magnetic monopoles, whereas the background, consisting of atmospheric muon bundles and neutrinos, remains on the same level as for IC22. The event selection consists of a series of relatively simple cuts based on the characteristic features of either monopoles or particular types of background. At the final level of the analysis the data is separated in two branches based on the event brightness. This done to handle a discrepancy between experimental and simulated data by applying different cuts in both branches.

Three events that pass all cuts of the analysis are observed in the complete IC40 data. One event in the low brightness branch shows the characteristics of a neutrino induced muon and is consistent with the expected background rate for this branch. The other two events cannot be definitely classified since they are located in the outskirts of the detector and are thus only partially contained. This is problematic since the two events represent a large deviation from the expected number of background events in the high brightness branch. However, additional studies show that they are unlikely to be magnetic monopoles.

The resulting limits on the flux of magnetic monopoles are currently the most stringent in the velocity range from $\beta \geq 0.76$ to $\gamma < 10^7$. The two events observed in the high brightness branch have a significant impact, though. Compared to the IC22 analysis, where no events were observed, the improvement is relatively small. However, for IC22 this result was only achieved after a re-unblinding procedure, which re-evaluated several cuts based on an improved background simulation. The limits derived in this work are therefore more rigorous.

Despite the achievement made in this work, future analyses still have many possible ways of improvement. Light generated by secondary electrons can produce detectable signatures even if the primary monopole is below the Cherenkov threshold. Including this effect in the simulation may allow monopole searches down to $\beta \approx 0.55$. Another crucial point is the event reconstruction. The two remaining events in the high brightness branch of this analysis likely passed due a poor reconstruction. A general improvement of the reconstruction quality may be achieved by applying selecting only sufficiently contained events. Finally, the biggest improvement will come from using data taken with the full detector for several years.

A Analysis of Final Events

This appendix describes a more detailed study of the 3 events found in the full year sample. The purpose is to test if these events are magnetic monopoles and to allow a better distinction between monopoles and background events in future analyzes. Table A.1 below summarizes some basic information like the event ID and several reconstructed parameters for the events.

	Event 1	Event 2	Event 3
Branch	HLD	HLD	LLD
Run	110860	110962	112181
EventID	1895025	17684691	29110332
Nch	154	125	166
NPE	6163	4905	2135
θ_z (LF)	91.9°	97.5°	102.5°
θ_z (MPE)	54.2°	78.7°	101.4°
Velocity	0.83c	0.82c	1.0c

Table A.1: Several parameters of the 3 observed events.

A.1 LLD Event

The event observed in the LLD branch of the analysis is consistent with a pure background interpretation. In fact the event has all the characteristics expected from muons generated in a neutrino interaction: a track-like signature (Figure A.1) and a velocity approximately equal to the speed of light (Figure A.2). Therefore, it seems safe to assume that event was not caused by a magnetic monopole but a neutrino.

Currently, none of the variables is designed particularly to distinguish neutrino events. The reason is that the neutrino background is several orders of magnitude smaller than the atmospheric muon background. However, at the final cut level neutrino events constitute a significant fraction of the background at the final cut level or even dominate it as in the case of the LLD branch. Future searches for relativistic monopoles are likely to require parameters dedicated to neutrino discrimination. This may also include astrophysical neutrinos, for which first evidence was found recently [174].

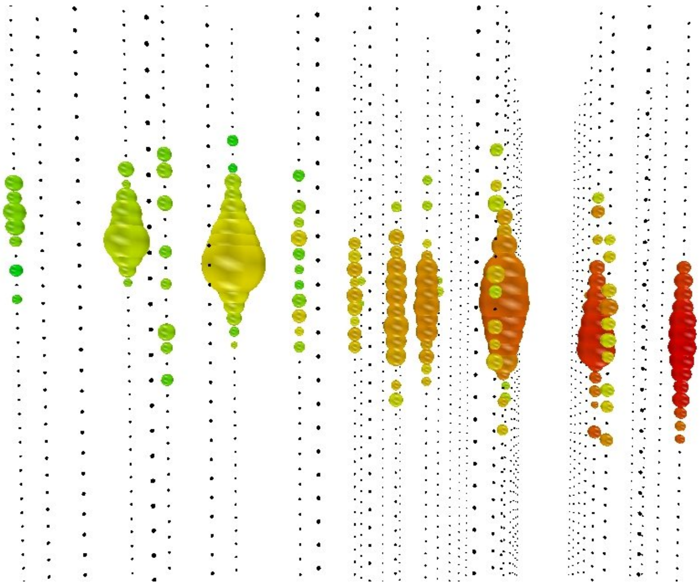

Figure A.1: A view of the event observed in the LLD branch.

A.2 HLD Events

The two events observed in the HLD branch have come under particular scrutiny since they represent a factor of ~ 10 deviation from the expected number of background events. Visual inspection of the events (see Figure A.3) reveals that for both most of the light is received by DOMs in the outskirts of the detector. This strongly indicates that the events are only partially contained. The second event (ID 17684691) also features several neighboring DOMs that recorded significantly more light than average, which could be explained with a bright cascade occurring in the immediate vicinity.

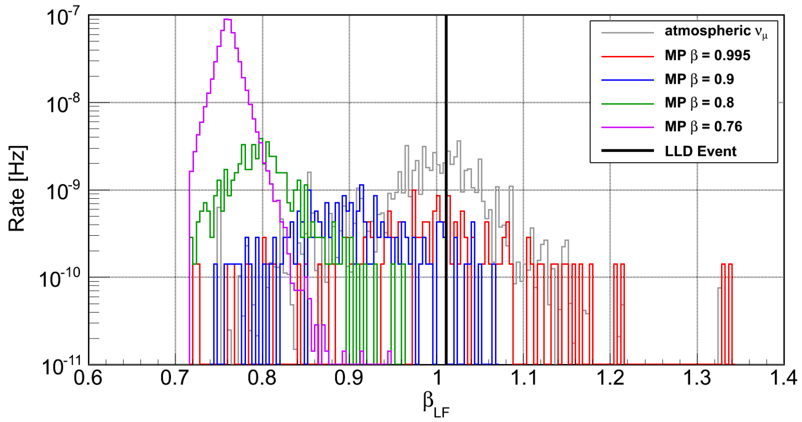

Figure A.2: Reconstructed velocity of the event observed in the LLD branch. Also shown are the velocity distributions of the signal simulations and (neutrino) background in this branch.

The reconstruction using LineFit places arrival direction of both events slightly below the horizon, where effectively no cut is applied in the final level. However, due to their location and the applied hit selection the lever arm may have been to small for an accurate reconstruction. As an alternative, the standard likelihood reconstruction for muon is applied to the events. This reconstruction consists of several consecutive likelihood fit, where each fit is used as seed for the next. The chain of fits starts with a LineFit and ends with the so-called *MPEFit*. The reason these fits were not applied during the actual analysis is because they are computationally intensive and do not yield a better result for a monopole event than the LineFit if they converge to a solution at all. However, if the two events are background, the likelihood fits are expected to perform better than the LineFit. For the two events the final MPEFit finds arrival directions above the horizon. The actual zenith angles from both reconstructions are listed in Table A.1.

The different direction reconstruction alone does not provide enough information in order to decide whether the two events are signal or background. To do that, additional monopole datasets were generated, where the monopoles were seeded with one of the reconstructed directions and made to intersect the detector in the same location as the observed events. Since this location may not be accurate, the final monopole tracks are ran-

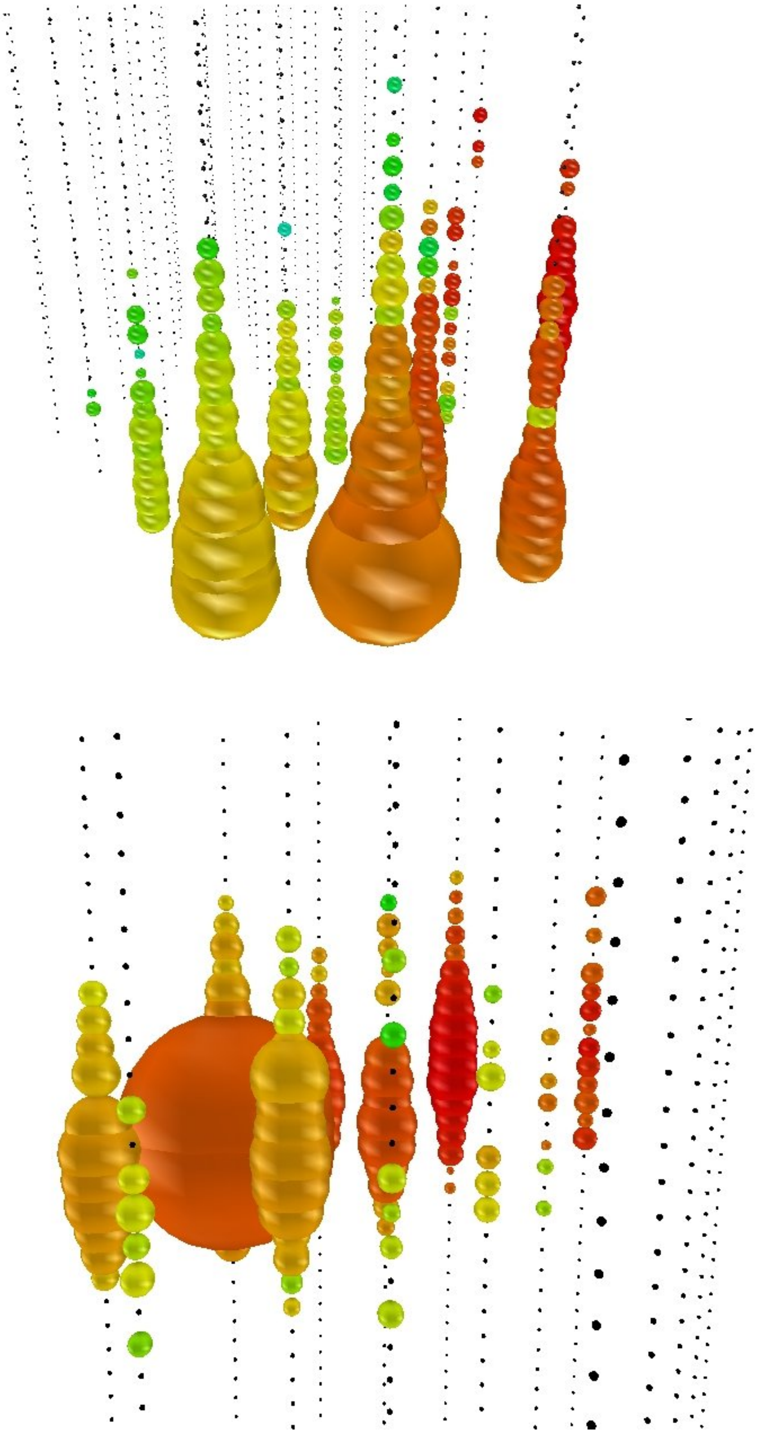

Figure A.3: Views of the two events observed in the HLD branch.

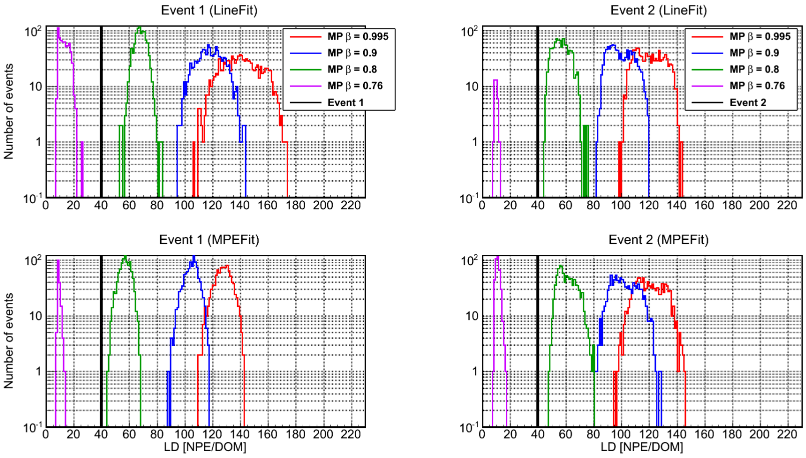

Figure A.4: Comparison of the LD parameter of the two events (left/right) observed in HLD branch and the additional monopole simulation based on the LineFit (top) and the MPEFit (bottom). The distribution from the simulation are shown at cut level 3.

domly shifted parallel to the original track up to a maximum of 50 m. The final data then consists of 16 datasets (4 velocities, 2 directions) for each of the two events, which are processed in the same way as the original data used for this analysis. In order to keep the simulation and processing time small, not more than 1000 monopoles are generated for each dataset.

Comparing the distribution of certain parameters from the new simulations with the parameter value of the corresponding event allows to classify said event under the assumption that it was caused by a monopole. Figures A.4 and A.5 show the distributions for LD and Δt variables. Considering the LD parameter, both events appear like a relatively slow monopole with a velocity somewhere between $0.76c$ and $0.8c$. The Δt parameter, on the other hand, suggests a rather fast monopole. Such inconsistencies can be found for other parameters as well, though to varying degrees. The signal hypothesis for the two events is therefore unlikely to hold true.

A combination of the LD and Δt parameter could potentially be used to remove the two events as is evident from Figure A.6. Such a cut would also reduce the remaining background of atmospheric neutrinos, though it is not certain that the two events have actually been caused by a neutrino. Another approach, that was tested, aims to identify events that are not well contained by the detector and thus can not be accurately

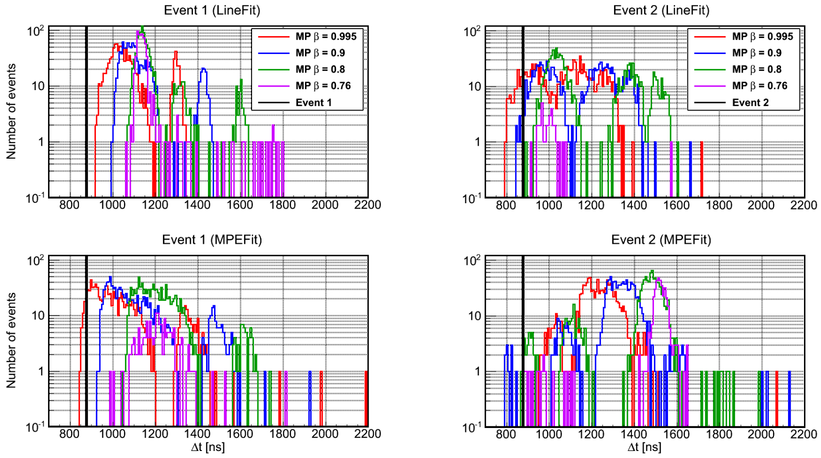

Figure A.5: Same as Figure A.4 for the Δt parameter.

reconstructed with current algorithms. A possible parameter to characterize such events is the charge recorded in the outer layer of the detector relative to the total charge. Here, the outer layer defined by all outer strings plus the top and bottom most DOM on any other string. For the two event very high values of 88% and 93% are observed. Unfortunately, for IC40 the outer layer comprises more than half of the actual detector, partly due to its irregular shape. The fractional charge on the outer layer is therefore not a good cut parameter here but may serve this purpose for the full detector.

Ultimately, it is unlikely that the two events observed in the HLD branch have been caused by magnetic monopoles since their characteristics do not match. However, they can not be conclusively classified as atmospheric muon bundles or atmospheric neutrinos, due to them being only partially contained. Still, the basic conclusion is that the simulation of the background at the final cut level is deficient to some degree. The question whether this is due to an imperfect model of the known atmospheric background or not simulated component like cosmic neutrinos can not be answered here.

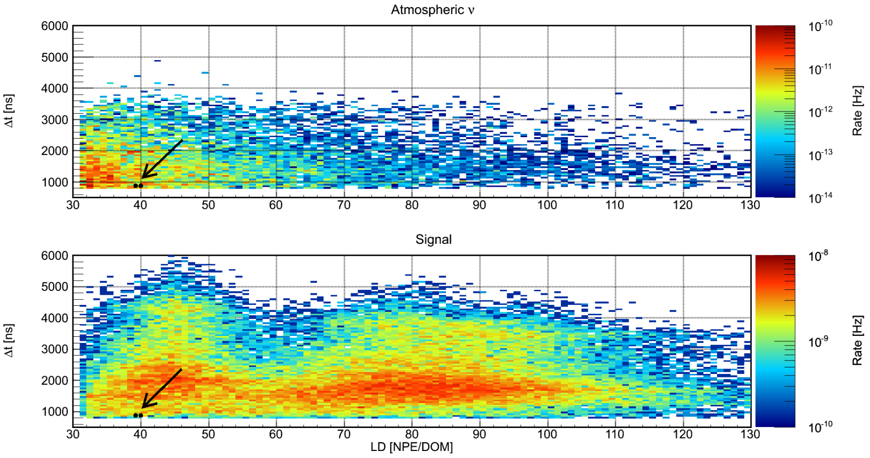

Figure A.6: Distribution of neutrino (top) and signal (bottom) events in the LD vs Δt plane after all HLD cuts. The positions of the two events observed in this branch are marked by black dots. Note that the signal data used here is the original data described in Section 5.2.

B Supplementary Plots

B.1 Level 2 Cut Parameters

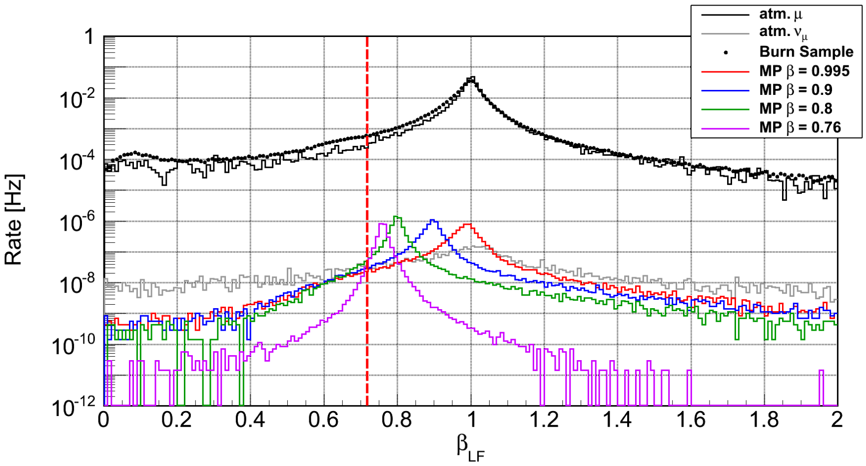

Figure B.1: Cut on the reconstructed velocity (in units of c).

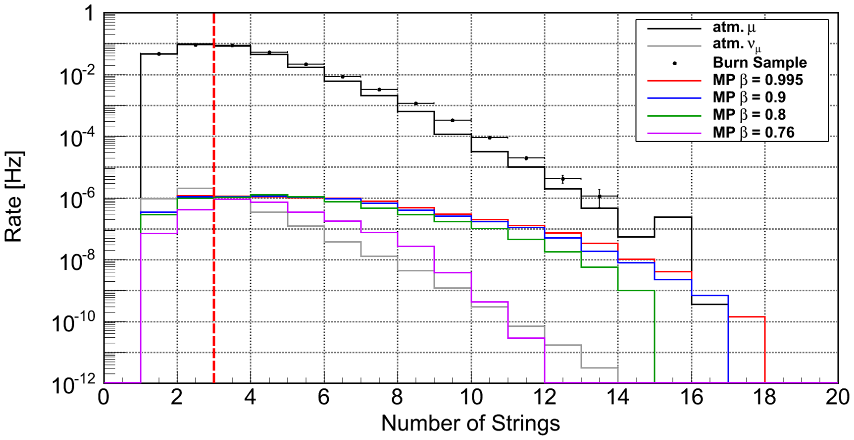

Figure B.2: Cut on the number of strings.

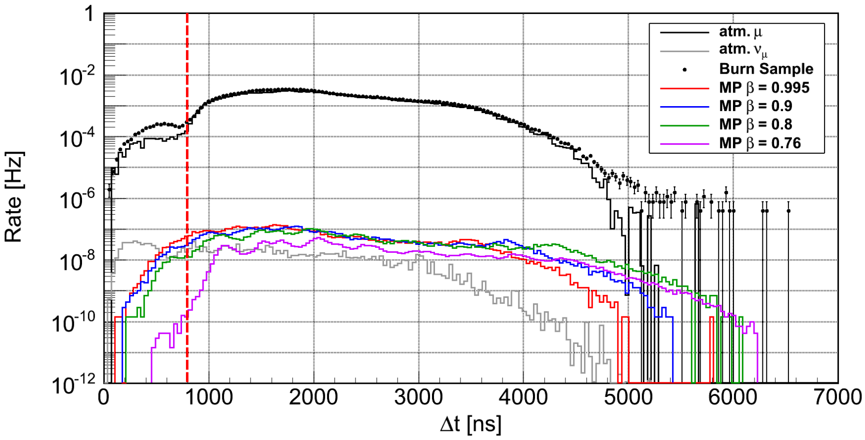

Figure B.3: Cut on the time range (Δt) of the event.

B.2 Level 3 Cut Parameters

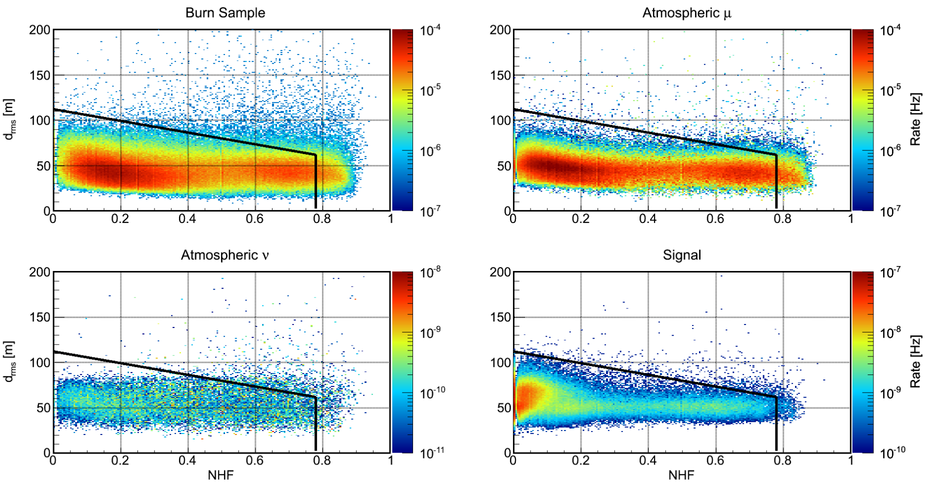

Figure B.4: Cut in the $d_\perp^{\mathsf{RMS}}$ vs NHF plane.

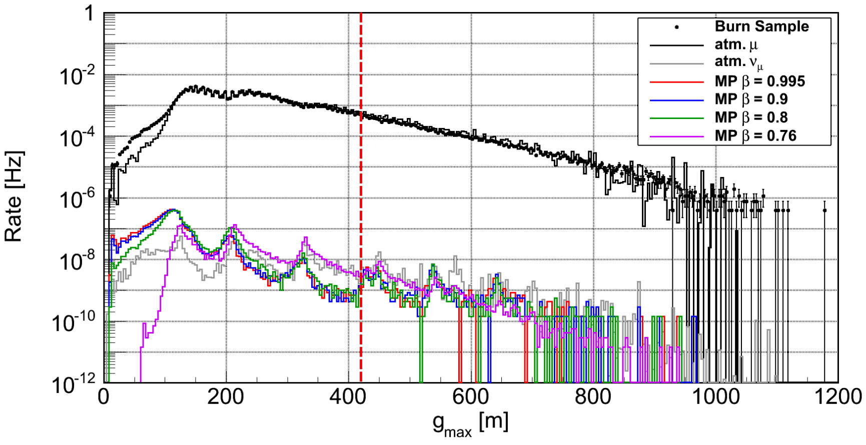

Figure B.5: Cut on the g_{max} variable.

B.3 Data Split

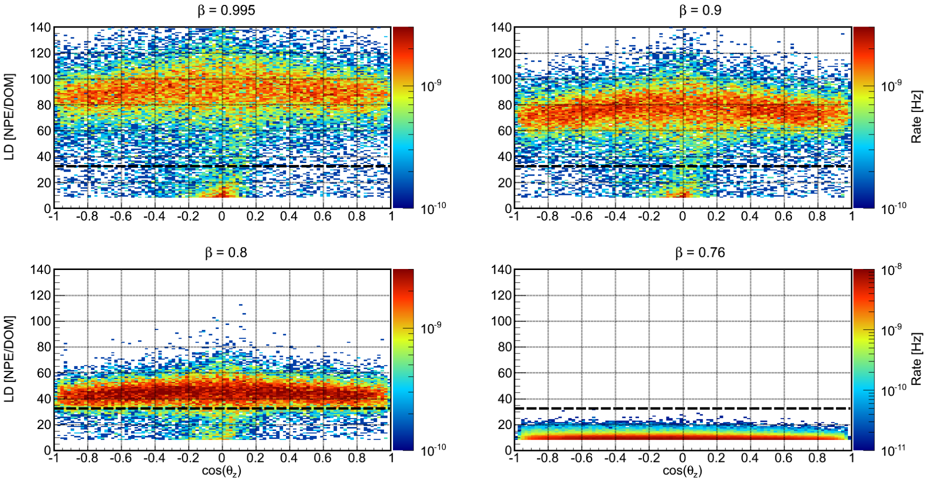

Figure B.6: Split of the data in the zenith angle vs LD plane for signal.

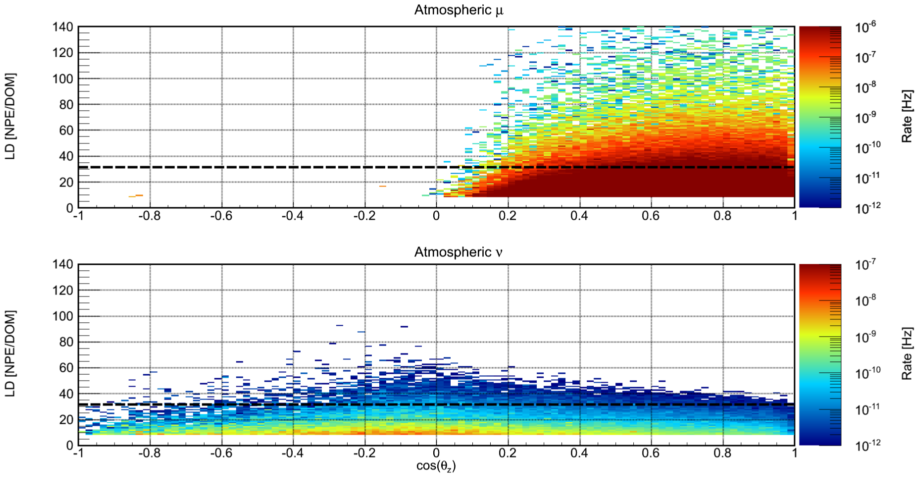

Figure B.7: Split of the data in the zenith angle vs LD plane for background.

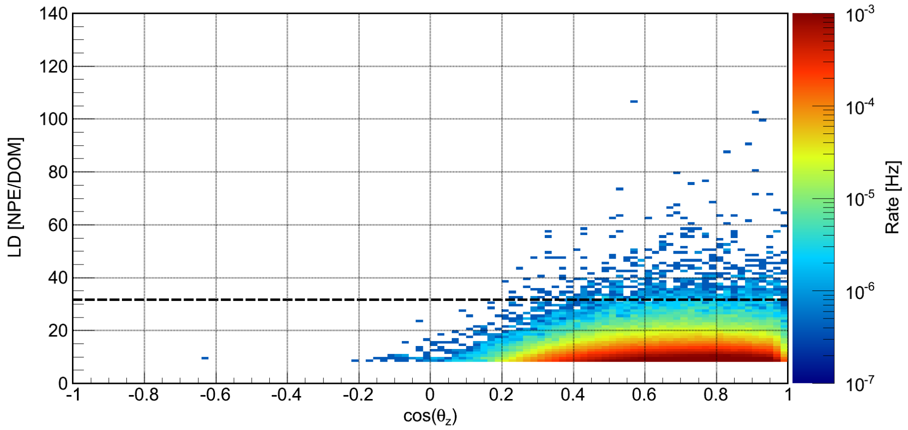

Figure B.8: Split of the data in the zenith angle vs LD plane for the burn sample.

B.4 Level 4 Cut Parameters

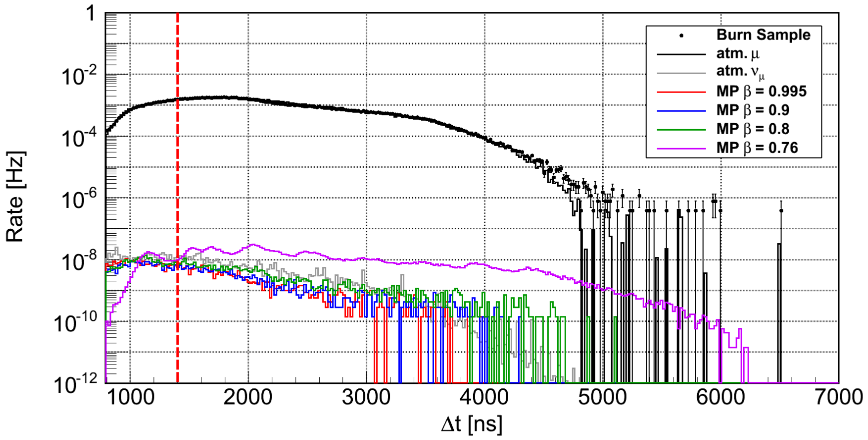

Figure B.9: Cut on the time range (Δt) in the LLD branch.

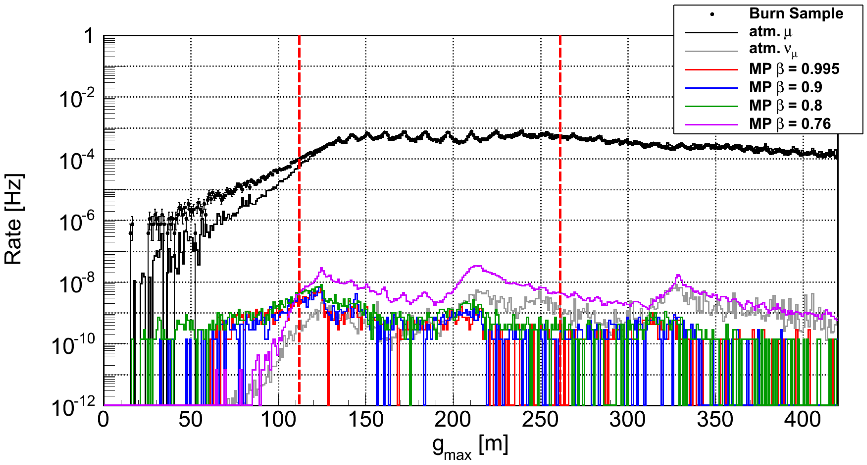

Figure B.10: Cut on the g_{max} variable in the LLD branch.

C Supplementary Tables

Interval	$\beta = 0.995$	$\beta = 0.9$	$\beta = 0.8$	$\beta = 0.76$
$-1.0 \leq \cos(\theta_z) < -0.9$	0.219803	0.203402	0.169802	0.014534
$-0.9 \leq \cos(\theta_z) < -0.8$	0.306004	0.308204	0.240003	0.056476
$-0.8 \leq \cos(\theta_z) < -0.7$	0.340005	0.338205	0.291004	0.076956
$-0.7 \leq \cos(\theta_z) < -0.6$	0.390405	0.372805	0.313204	0.118437
$-0.6 \leq \cos(\theta_z) < -0.5$	0.411006	0.385805	0.348605	0.133515
$-0.5 \leq \cos(\theta_z) < -0.4$	0.414606	0.405406	0.343605	0.131212
$-0.4 \leq \cos(\theta_z) < -0.3$	0.402406	0.416406	0.369405	0.136038
$-0.3 \leq \cos(\theta_z) < -0.2$	0.433006	0.419006	0.366405	0.123201
$-0.2 \leq \cos(\theta_z) < -0.1$	0.419006	0.429006	0.363205	0.010631
$-0.1 \leq \cos(\theta_z) < 0.0$	0.421806	0.409806	0.356205	0.000020
$0.0 \leq \cos(\theta_z) < 0.1$	0.384205	0.357805	0.204602	0.000000
$0.1 \leq \cos(\theta_z) < 0.2$	0.282404	0.212602	0.016400	0.000000
$0.2 \leq \cos(\theta_z) < 0.3$	0.096400	0.032000	0.000200	0.000000
$0.3 \leq \cos(\theta_z) < 0.4$	0.010200	0.001600	0.000000	0.000000
$0.4 \leq \cos(\theta_z) < 0.5$	0.000200	0.000200	0.000000	0.000000
$0.5 \leq \cos(\theta_z) < 0.6$	0.000000	0.000000	0.000000	0.000000
$0.6 \leq \cos(\theta_z) < 0.7$	0.000000	0.000000	0.000000	0.000000
$0.7 \leq \cos(\theta_z) < 0.8$	0.000000	0.000000	0.000000	0.000000
$0.8 \leq \cos(\theta_z) < 0.9$	0.000000	0.000000	0.000000	0.000000
$0.9 \leq \cos(\theta_z) < 1.0$	0.000000	0.000000	0.000000	0.000000

Table C.1: Detection efficiency for each $\cos\theta_z$ bin

Filter	Prescale	Rate (Hz)	Description
CascadeFilter	1	17.7	Electromagnetic showers
DownGoingContained	1	14.7	Down-going tracks fully- or partially-contained
EHEFilter	1	1.4	High energy events
FilterMinBias	3000	0.5	All events
ICDownStarting	1	1.9	Down-going tracks starting inside the detector
ICLowEnergyContainedFilter	1	6.3	Single string events with additional cuts
ICMuonFilter	1	23.0	Combined up-going track events
IceTopSTA3	5	2.5	All IceTop triggered events
IceTopSTA8	1	0.7	IceTop triggered events with ≥ 8 stations
IceTopSTA3_InIceSMT	1	2.2	Events with InIce and IceTop trigger
InIceSMT_IceTopCoincidence	20	1.6	Events with InIce trigger and IceTop activity
JAMSFilter	1	3.6	Low energy up-going tracks with hits in AMANDA
LECascadeFilter	1	8.4	Low energy electromagnetic showers
LowUpFilter	1	11.9	Low energy up-going tracks
MoonFilter	1	variable	Events from moon direction
PhysicsMinBiasTrigger	60	0.5	Randomly triggered events

Table C.2: Physics Filter Rates During IceCube 40-string Physics Run [175]. Prescale represents the fraction of events that are sent north over the satellite.

Bibliography

[1] M. Brand, S. Neaves, and E. Smith, "Loadstone." `http://www.magnet.fsu.edu/education/tutorials/museum/lodestone.html`, 1995. Accessed: 2013-02-28.

[2] W. Gilbert, *De Magnete.* 1600.

[3] J. C. Maxwell, "A dynamic theory of the electromagnetic field," *Philos. Trans. R. Soc. Lond.*, vol. 155, pp. 459–512, 1865.

[4] J. C. Maxwell, *A Treatise on Electricity and Magnetism.* Oxford, Clarendon Press, 1873.

[5] P. Curie, "Sur la possibilite d'existence de la conductibilite magnetique et du magnetisme libre," *Seances de la Societe Francaise de Physique*, pp. 76–77, 1894.

[6] P. A. M. Dirac, "Quantised singularities in the electromagnetic field," *Proc. R. Soc. London, Ser. A*, vol. 133, no. 821, pp. 60–72, 1931.

[7] T. J. Allen, C. J. Efthimiou, and D. Spector, "A mechanism for charge quantization." arXiv:hep-th/0209204, 2002.

[8] H. Georgi and S. L. Glashow, "Unity of all elementary-particle forces," *Phys. Rev. Lett.*, vol. 32, pp. 438–441, Feb 1974.

[9] J. L. Pinfold, "Searching for the magnetic monopole and other highly ionizing particles at accelerators using nuclear track detectors," *Radiat. Meas.*, vol. 44, no. 9–10, pp. 834–839, 2009. Proceedings of the 24th International Conferenceon Nuclear Tracks in Solids.

[10] J. P. Preskill, "Magnetic monopoles," *Ann. Rev. Nucl. Part. Sci.*, vol. 34, pp. 461–530, 1984.

[11] J. Polchinski, "Monopoles, duality, and string theory," *Int. J. Mod. Phys. A*, vol. 19, p. 145, 2004.

[12] R. Littlejohn, "Gaussian, si and other systems of units in electromagnetic theory." Lecture Notes, 2007. Retrieved 2013-02-28.

[13] J. D. Jackson, *Classical Electrodynamic Third Edition.* Wiley, 1998.

[14] F. Moulin, “Magnetic monopoles and lorentz force,” *Il Nuovo Cimento B*, vol. 116, pp. 869–877, Aug 2001.

[15] S. Errede, “Magnetic monopoles - fundamental / point-like magnetic charges.” Lecture Notes, 2007. Retrieved 2013-02-28.

[16] A. Rajantie, “Introduction to magnetic monopoles,” *Contemp. Phys.*, vol. 53, no. 3, pp. 195–211, 2012.

[17] R. P. Feynman, R. B. Leighton, and M. Sands, *The Feynman Lectures on Physics: Vol. 2.* Addison-Wesley, 1964.

[18] Y. Aharonov and D. Bohm, “Significance of electromagnetic potentials in the quantum theory,” *Phys. Rev.*, vol. 115, pp. 485–491, Aug 1959.

[19] P. A. M. Dirac, “The theory of magnetic poles,” *Phys. Rev.*, vol. 74, pp. 817–830, Oct 1948.

[20] T. T. Wu and C. N. Yang, “Concept of nonintegrable phase factors and global formulation of gauge fields,” *Phys. Rev. D*, vol. 12, pp. 3845–3857, Dec 1975.

[21] T. T. Wu and C. N. Yang, “Dirac monopole without strings: Monopole harmonics,” *Nucl. Phys. B*, vol. 107, no. 3, pp. 365–380, 1976.

[22] R. A. Brandt and J. R. Primack, “Dirac monopole theory with and without strings,” *Phys. Rev. D*, vol. 15, pp. 1175–1177, Feb 1977.

[23] G. ’t Hooft, “Magnetic monopoles in unified gauge theories,” *Nucl. Phys. B*, vol. 79, pp. 276–284, 1974.

[24] A. M. Polyakov, “Particle spectrum in quantum field theory,” *JETP Lett.*, vol. 20, p. 194, Sep 1974.

[25] A. Buras, J. Ellis, M. Gaillard, and D. Nanopoulos, “Aspects of the grand unification of strong, weak and electromagnetic interactions,” *Nucl. Phys. B*, vol. 135, no. 1, pp. 66–92, 1978.

[26] A. H. Guth and S. H. H. Tye, “Phase transitions and magnetic monopole production in the very early universe,” *Phys. Rev. Lett.*, vol. 44, no. 10, pp. 631–635, 1980.

[27] G. Börner, *The early universe.* Springer, 2004.

[28] M. E. Peskin and D. V. Schroeder, *An Introduction to Quantum Field Theory.* Westview Press, 1995.

[29] H. Georgi, H. R. Quinn, and S. Weinberg, “Hierarchy of interactions in unified gauge theories,” *Phys. Rev. Lett.*, vol. 33, pp. 451–454, Aug 1974.

[30] M. Daniel, G. Lazarides, and Q. Shafi, “Su(5) monopoles, magnetic symmetry and confinement,” *Nucl. Phys. B*, vol. 170, no. 1, pp. 156–164, 1980.

[31] E. J. Weinberg, “Monopoles and grand unification,” in *Monopole ’83* (J. L. Stone, ed.), vol. 111 of *NATO ASI Series*, pp. 1–16, Springer US, 1984.

[32] P. H. Frampton and T. W. Kephart, “Higgs sector and proton decay in su(15) grand unification,” *Phys. Rev. D*, vol. 42, pp. 3892–3894, Dec 1990.

[33] P. H. Frampton and B.-H. Lee, “Su(15) grand unification,” *Phys. Rev. Lett.*, vol. 64, pp. 619–621, Feb 1990.

[34] P. B. Pal, “Monopoles of su(15) grand unification,” *Phys. Rev. D*, vol. 44, pp. R1366–R1368, Sep 1991.

[35] G. Lazarides, C. Panagiotakopoulos, and Q. Shafi, “Magnetic monopoles from superstring models,” *Phys. Rev. Lett.*, vol. 58, pp. 1707–1710, Apr 1987.

[36] T. W. Kephart, C.-A. Lee, and Q. Shafi, “Family unification, exotic states and light magnetic monopoles,” *J. High Energy Phys.*, vol. 2007, no. 01, p. 088, 2007.

[37] S. King and Q. Shafi, “Minimal supersymmetric SU(4)×SU(2)L×SU(2)R,” *Phys. Lett. B*, vol. 422, no. 1–4, pp. 135–140, 1998.

[38] D. Kirzhnits, “Weinberg model and the ”hot” universe,” *JETP Lett.*, vol. 15, pp. 529–531, 1972.

[39] T. W. B. Kibble, “Topology of cosmic domains and strings,” *J. Phys. A: Math. Gen.*, vol. 9, no. 8, p. 1387, 1976.

[40] J. Schwinger, “A magnetic model of matter,” *Science*, vol. 165, pp. 757–761, Aug 1969.

[41] M. B. Hindmarsh and T. W. B. Kibble, "Cosmic strings," *Rep. Prog. Phys.*, vol. 58, no. 5, p. 477, 1995.

[42] M. S. Turner, "Monopoles and astrophysics," in *Magnetic Monopoles* (R. A. J. Carrigan and W. P. Trower, eds.), vol. 102 of *NATO ASI Series*, pp. 127–140, Plenum Pree, New York, 1983.

[43] J. P. Preskill, "Cosmological production of superheavy magnetic monopoles," *Phys. Rev. Lett.*, vol. 43, pp. 1365–1368, Nov 1979.

[44] P. Langacker, "Grand unified theories and proton decay," *Phys. Rep.*, vol. 72, no. 4, pp. 185–385, 1981.

[45] S. Dar, Q. Shafi, and A. Sil, "Flux of primordial monopoles," *Phys. Rev. D*, vol. 74, p. 035013, Aug 2006.

[46] Q. Shafi and V. N. Senoguz, "Coleman-weinberg potential in good agreement with wmap," *Phys. Rev. D*, vol. 73, p. 127301, Jun 2006.

[47] D. Nanopoulos, K. Olive, M. Srednicki, and K. Tamvakis, "Gauge hierarchy generation and cosmology in locally supersymmetric guts," *Phys. Lett. B*, vol. 124, no. 3–4, pp. 171–174, 1983.

[48] E. W. Kolb and M. S. Turner, *The Early Universe.* Addison-Wesley, 1990.

[49] S. D. Wick, T. W. Kephart, T. J. Weiler, and P. L. Biermann, "Signatures for a cosmic flux of magnetic monopoles," *Astropart. Phys.*, vol. 18, no. 6, pp. 663–687, 2003.

[50] R. Beck, A. Brandenburg, D. Moss, A. Shukurov, and D. Sokoloff, "Galactic magnetism: Recent developments and perspectives," *Annu. Rev. Astron. Astrophys.*, vol. 34, pp. 155–206, 1996.

[51] P. P. Kronberg, P. Biermann, and F. R. Schwab, "The nucleus of m82 at radio and x-ray bands - discovery of a new radio population of supernova candidates," *Astrophys. J.*, vol. 291, pp. 693–707, Apr 1985.

[52] K. I. Kellermann and I. I. K. Pauliny-Toth, "Compact radio sources," *Annu. Rev. Astron. Astrophys.*, vol. 19, pp. 373–410, 1981.

[53] T. A. Ensslin, P. L. Biermann, P. P. Kronberg, and X.-P. Wu, "Cosmic-ray protons and magnetic fields in clusters of galaxies and their cosmological consequences," *Astrophys. J.*, vol. 477, no. 2, p. 560, 1997.

[54] D. Ryu, H. Kang, and P. L. Biermann, "Cosmic magnetic fields in large scale filaments and sheets," *Astron. Astrophys.*, vol. 335, pp. 19–25, Jul 1998.

[55] E. Huguet and P. Peter, "Bound states in monopoles: sources for uhecr?," *Astropart. Phys.*, vol. 12, no. 4, pp. 277–289, 2000.

[56] G. Giacomelli and L. Patrizii, "Magnetic monopole searches." arXiv:hep-ex/0302011v2, Feb 2003.

[57] G. Giacomelli, "The experimental detection of magnetic monopoles," in *Theory and Detection of Magnetic Monopoles in Gauge Theories* (N. Craigie, ed.), ch. 7, pp. 407–499, World Scientific, 1986.

[58] S. P. Ahlen, "Theoretical and experimental aspects of the energy loss of relativistic heavily ionizing particles," *Rev. Mod. Phys.*, vol. 52, pp. 121–173, Jan 1980.

[59] S. P. Ahlen, "Monopole-track characteristics in plastic detectors," *Phys. Rev. D*, vol. 14, pp. 2935–2940, Dec 1976.

[60] S. P. Ahlen, "Stopping-power formula for magnetic monopoles," *Phys. Rev. D*, vol. 17, pp. 229–233, Jan 1978.

[61] R. M. Sternheimer, "General expression for the density effect for the ionization loss of charged particles," *Phys. Rev. B*, vol. 24, pp. 6288–6291, Dec 1981.

[62] Y. Kazama, C. N. Yang, and A. S. Goldhaber, "Scattering of a dirac particle with charge ze by a fixed magnetic monopole," *Phys. Rev. D*, vol. 15, pp. 2287–2299, Apr 1977.

[63] P. A. Cherenkov, "Visible emission of clean liquids by action of gamma radiation," *Doklady Akademii Nauk SSSR*, vol. 2, p. 451, 1934.

[64] L. Rädel, "Simulation studies of the cherenkov light yield from relativistic particles in high-energy neutrino telescopes with geant4," Master's thesis, RWTH Aachen, 2012.

[65] C. A. Mead, "Quantum theory of the refractive index," *Phys. Rev.*, vol. 110, pp. 359–369, Apr 1958.

[66] D. R. Tompkins, "Total energy loss and Čerenkov emission from monopoles," *Phys. Rev.*, vol. 138, pp. B248–B250, Apr 1965.

[67] J. Beringer *et al.*, “Review of particle physics,” *Phys. Rev. D*, vol. 86, p. 010001, Jul 2012.

[68] V. A. Rubakov, “Superheavy magnetic monopoles and decay of the proton,” *JETP Lett.*, vol. 33, pp. 644–646, Jun 1981.

[69] V. A. Rubakov, “Adler-bell-jackiw anomaly and fermion-number breaking in the presence of a magnetic monopole,” *Nucl. Phys. B*, vol. 203, no. 2, pp. 311–348, 1982.

[70] C. G. Callan, “Disappearing dyons,” *Phys. Rev. D*, vol. 25, pp. 2141–2146, Apr 1982.

[71] C. G. Callan, “Dyon-fermion dynamics,” *Phys. Rev. D*, vol. 26, pp. 2058–2068, Oct 1982.

[72] V. A. Rubakov, “Monopole catalysis of proton decay,” *Rep. Prog. Phys.*, vol. 51, no. 2, p. 189, 1988.

[73] S. M. Errede, “Experimental limits on monopole catalysis of nucleon decay,” in *Monopole ’83* (J. L. Stone, ed.), vol. 111 of *NATO ASI Series*, pp. 251–294, Springer US, 1984.

[74] J. Arafune and M. Fukugita, “Velocity-dependent factors for the rubakov process for slowly moving magnetic monopoles in matter,” *Phys. Rev. Lett.*, vol. 50, pp. 1901–1902, Jun 1983.

[75] S. Dawson and A. N. Schellekens, “Monopole catalysis of proton decay in so(10) grand unified models,” *Phys. Rev. D*, vol. 27, pp. 2119–2128, May 1983.

[76] A. N. Schellekens, “Boundary-condition independence of catalysis of proton decay by monopoles,” *Phys. Rev. D*, vol. 29, pp. 2378–2386, May 1984.

[77] T. Walsh, P. Weisz, and T. T. Wu, “Monopole catalysis of proton decay,” *Nucl. Phys. B*, vol. 232, no. 2, pp. 349 – 355, 1984.

[78] M. L. Benabderrahmane, E. Jacobi, and S. f. t. I. C. Schönen, “Results and future developments of the search for subrelativistic magnetic monopoles with icecube,” in *International Cosmic Ray Conference*, 2013.

[79] P. Ade *et al.*, “Planck 2013 results. xvi. cosmological parameters.” arXiv:1303.5076, Mar 2013.

[80] M. S. Turner, E. N. Parker, and T. J. Bogdan, "Magnetic monopoles and the survival of galactic magnetic fields," *Phys. Rev. D*, vol. 26, pp. 1296–1305, Sep 1982.

[81] E. W. Kolb, S. A. Colgate, and J. A. Harvey, "Monopole catalysis of nucleon decay in neutron stars," *Phys. Rev. Lett.*, vol. 49, pp. 1373–1375, Nov 1982.

[82] S. Dimopoulos, J. Preskill, and F. Wilczek, "Catalyzed nucleon decay in neutron stars," *Phys. Lett. B*, vol. 119, pp. 320–322, Dec 1982.

[83] B. Cabrera, "First results from a superconductive detector for moving magnetic monopoles," *Phys. Rev. Lett.*, vol. 48, pp. 1378–1381, May 1982.

[84] S. Orito *et al.*, "Search for supermassive relics with a 2000-m^2 array of plastic track detectors," *Phys. Rev. Lett.*, vol. 66, pp. 1951–1954, Apr 1991.

[85] Y. Novoseltsev, M. Boliev, A. Butkevich, S. Mikheev, and V. Petkov, "A search for massive magnetic monopoles at the baksan underground scintillation telescope (bust)," *Nucl. Phys. B, Proc. Suppl.*, vol. 151, no. 1, pp. 337–340, 2006.

[86] J. M. Kovalik and J. L. Kirschvink, "New superconducting-quantum-interference-device-based constraints on the abundance of magnetic monopoles trapped in matter: An investigation of deeply buried rocks," *Phys. Rev. A*, vol. 33, pp. 1183–1187, Feb 1986.

[87] H. Jeon and M. J. Longo, "Search for magnetic monopoles trapped in matter," *Phys. Rev. Lett.*, vol. 75, pp. 1443–1446, Aug 1995.

[88] P. B. Price and M. H. Salamon, "Search for supermassive magnetic monopoles using mica crystals," in *International Cosmic Ray Conference* (F. C. Jones, ed.), vol. 8, pp. 242–245, Aug 1985.

[89] G. Giacomelli and A. Margiotta, "The macro experiment at gran sasso," 2007.

[90] R. Abbasi *et al.*, "Search for relativistic magnetic monopoles withătheăamanda-iiăneutrino telescope," *Eur. Phys. J. C*, vol. 69, no. 3-4, pp. 361–378, 2010.

[91] V. Aynutdinov *et al.*, "Search for relativistic magnetic monopoles with the baikal neutrino telescope," *Astropart. Phys.*, vol. 29, no. 6, pp. 366–372, 2008.

[92] S. Adrian-Martinez *et al.*, "Search for relativistic magnetic monopoles with the antares neutrino telescope," *Astropart. Phys.*, vol. 35, no. 10, pp. 634–640, 2012.

[93] R. Abbasi *et al.*, "Search for relativistic magnetic monopoles with icecube," *Phys. Rev. D*, vol. 87, p. 022001, Jan 2013.

[94] D. P. Hogan, D. Z. Besson, J. P. Ralston, I. Kravchenko, and D. Seckel, "Relativistic magnetic monopole flux constraints from rice," *Phys. Rev. D*, vol. 78, p. 075031, Oct 2008.

[95] M. Detrixhe *et al.*, "Ultrarelativistic magnetic monopole search with the anita-ii balloon-borne radio interferometer," *Phys. Rev. D*, vol. 83, p. 023513, Jan 2011.

[96] J. Bartelt *et al.*, "Monopole-flux and proton-decay limits from the soudan 1 detector," *Phys. Rev. D*, vol. 36, pp. 1990–2000, Oct 1987.

[97] M. Ambrosio *et al.*, "Search for nucleon decays induced by gut magnetic monopoles with the macro experiment," *Eur. Phys. J. C*, vol. 26, no. 2, pp. 163–172, 2002.

[98] V. Balkanov *et al.*, "The baikal deep underwater neutrino experiment: Results, status, future," *Prog. Part. Nucl. Phys.*, vol. 40, pp. 391–401, 1998.

[99] F. Halzen and S. R. Klein, "Icecube: An instrument for neutrino astronomy," *Rev. Sci. Instrum.*, vol. 81, p. 081101, 2010.

[100] F. Halzen and D. Hooper, "High-energy neutrino astronomy: the cosmic ray connection," *Rep. Prog. Phys.*, vol. 65, p. 1025, 7 2002.

[101] J. Blümer, R. Engel, and J. R. Hörandel, "Cosmic rays from the knee to the highest energies," *Prog. Part. Nucl. Phys.*, vol. 63, no. 2, pp. 293–338, 2009.

[102] C. H. Wiebusch, *The Detection of Faint Light in Deep Underwater Neutrino Telescopes.* PhD thesis, RWTH Aachen, 1995.

[103] R. Gandhi, C. Quigg, M. H. Reno, and I. Sarcevic, "Ultrahigh-energy neutrino interactions," *Astropart. Phys.*, vol. 5, no. 2, pp. 81–110, 1996.

[104] M. Wallraff, "Design, implementation and test of a new feature extractor for the icecube neutrino observatory," Master's thesis, RWTH Aachen, 2010.

[105] B. A. P. van Rens, *Detection of magnetic monopoles below the Cherenkov limit.* PhD thesis, Amsterdam U., 2006.

[106] H. Yepes-Ramirez, "The antares neutrino telescope: Current status and first results," *Nucl. Phys. B*, vol. 215, no. 1, pp. 59–62, 2011.

[107] M. Spurio and KM3NeT Consortium, "Km3net: An underwater multi-km^3 neutrino detector," *Nucl. Instrum. Meth. A*, vol. 692, pp. 53–57, Nov 2012.

[108] R. Abbasi *et al.*, "The design and performance of icecube deepcore," *Astropart. Phys.*, vol. 35, no. 10, pp. 615–624, 2012.

[109] R. Abbasi *et al.*, "Icetop: The surface component of icecube," *Nucl. Instrum. Meth. A*, vol. 700, no. 0, pp. 188–220, 2013.

[110] A. Achterberg *et al.*, "First year performance of the icecube neutrino telescope," *Astropart. Phys.*, vol. 26, no. 3, pp. 155–173, 2006.

[111] R. Abbasi *et al.*, "The icecube data acquisition system: Signal capture, digitization, and timestamping," *Nucl. Instrum. Meth. A*, vol. 601, pp. 294–316, Apr 2009.

[112] R. Abbasi *et al.*, "Calibration and characterization of the icecube photomultiplier tube," *Nucl. Instrum. Meth. A*, vol. 618, no. 1–3, pp. 139–152, 2010.

[113] `https://wiki.icecube.wisc.edu/index.php/HLC`. Accessed: 2013-09-08.

[114] S. Kleinfelder, "Gigahertz waveform sampling and digitization circuit design and implementation," *IEEE Trans. Nucl. Sci.*, vol. 50, no. 4, pp. 955–962, 2003.

[115] `https://wiki.icecube.wisc.edu/index.php/ATWD`. Accessed: 2013-06-17.

[116] M. Ackermann *et al.*, "Optical properties of deep glacial ice at the south pole," *J. Geophys. Res.*, vol. 111, no. D13203, 2006.

[117] T. Glüsenkamp, “On the detection of subrelativistic magnetic monopoles with the icecube neutrino observatory,” Master’s thesis, RWTH Aachen, 2010.

[118] `https://docushare.icecube.wisc.edu/dsweb/Get/Document-45193/2008_TFT_StringTriggerProposal.pdf`. Accessed: 2013-06-17.

[119] `https://docushare.icecube.wisc.edu/dsweb/Get/Document-45185/2008_TFT_ULEE_trigger_proposal.pdf`. Accessed: 2013-06-17.

[120] `https://wiki.icecube.wisc.edu/index.php/Stage_1_geometry`. Accessed: 2013-06-14.

[121] `https://wiki.icecube.wisc.edu/index.php/Stage_2_geometry`. Accessed: 2013-06-14.

[122] `https://wiki.icecube.wisc.edu/index.php/Stage_3_geometry`. Accessed: 2013-06-14.

[123] A. Obertacke, “Search for relativistic magnetic monopoles below the cherenkov threshold with icecube-86,” Master’s thesis, Bergischen Universität Wuppertal, 2012.

[124] B. J. Christy, *A Search for Relativistic Magnetic Monopoles with the IceCube 22-String Detector*. PhD thesis, University of Maryland, 2011.

[125] J. Derkaoui, G. Giacomelli, T. Lari, A. Margiotta, M. Ouchrif, L. Patrizii, V. Popa, and V. Togo, “Energy losses of magnetic monopoles and of dyons in the earth,” *Astropart. Phys.*, vol. 9, no. 2, pp. 173–183, 1998.

[126] V. Hess *Phys. Zeitschr.*, vol. 13, p. 1084, 1912.

[127] T. K. Gaisser, F. Halzen, and T. Stanev, “Particle astrophysics with high energy neutrinos,” *Phys. Rep.*, vol. 258, pp. 173–236, Jul 1995.

[128] D. R. Bergman and J. W. Belz, “Cosmic rays: The second knee and beyond,” *J. Phys. G: Nucl. Part. Phys.*, vol. 34, no. 10, p. R359, 2007.

[129] M. Nagano, “Search for the end of the energy spectrum of primary cosmic rays,” *New J. Phys.*, vol. 11, p. 065012, Jun 2009.

[130] K. Nakamura and P. D. Group, “Review of particle physics,” *J. Phys. G: Nucl. Part. Phys.*, vol. 37, no. 7A, p. 075021, 2010.

[131] E. Fermi, “On the origin of the cosmic radiation,” *Phys. Rev.*, vol. 75, pp. 1169–1174, Apr 1949.

[132] W. I. Axford, E. Leer, and J. F. McKenzie, “The structure of cosmic ray shocks,” *Astron. Astrophys.*, vol. 111, pp. 317–325, Jul 1982.

[133] R. Hörandel, J, “On the knee in the energy spectrum of cosmic rays,” *Astropart. Phys.*, vol. 19, no. 2, pp. 193–220, 2003.

[134] K. Greisen, “End to the cosmic-ray spectrum?,” *Phys. Rev. Lett.*, vol. 16, pp. 748–750, Apr 1966.

[135] G. T. Zatsepin and V. A. Kuz’min, “Upper limit of the spectrum of cosmic rays,” *JETP Lett.*, vol. 4, p. 78, Aug 1966.

[136] T. Kajita, “Atmospheric neutrinos,” *Advances in High Energy Physics*, vol. 12, p. 504715, 2012.

[137] P. Gondolo, G. Ingelman, and M. Thunman, “Charm production and high-energy atmospheric muon and neutrino fluxes,” *Astropart. Phys.*, vol. 5, pp. 309–332, 1996.

[138] `https://wiki.icecube.wisc.edu/index.php/TFT_2008_Season_Planning`. Accessed: 2013-06-17.

[139] T. Gaisser, *Cosmic Rays and Particles Physics*. Cambridge University Press, 1990.

[140] X. Bai *et al.*, “Icetop/icecube coincidences,” in *Proceedings of the 30th International Cosmic Ray Conference* (R. Caballero, J. C. D’Olivo, G. Medina-Tanco, L. Nellen, F. A. Sánchez, and J. F. Valdés-Galicia, eds.), vol. 5, pp. 1209–1212, 2007.

[141] E. Aslanides *et al.*, “A deep sea telescope for high-energy neutrinos.” arXiv:astro-ph/9907432, 1999.

[142] T. Gaisser and M. Honda, “Flux of atmospheric neutrinos,” *Ann. Rev. Nucl. Part. Sci.*, vol. 52, pp. 153–199, 2002.

[143] G. W. Sullivan, “Results from the icecube experiment,” *Nucl. Phys. B, Proc. Suppl.*, vol. 235, pp. 346–351, Feb 2013.

[144] R. Abbasi *et al.*, “First neutrino point-source results from the 22-string icecube detector,” *Astrophys. J.*, vol. 701, pp. L47–L51, 2009.

[145] D. Chirkin and W. Rhode, "Muon monte carlo: a new high-precision tool for tracking of muons in medium," in *International Cosmic Ray Conference*, vol. 3, p. 1017, 2001.

[146] A. Roodman, "Blind analysis in particle physics," in *Statistical Problems in Particle Physics, Astrophysics, and Cosmology* (L. Lyons, R. Mount, and R. Reitmeyer, eds.), p. 166, 2003.

[147] T. DeYoung, "Icetray: A software framework for icecube," in *International Conference on Computing in High-Energy Physics and Nuclear Physics (CHEP2004)*, 2004. available from `http://www.chep2004.org/`.

[148] C. H. Wiebusch, *GEN 3.0 Generators for Events in Neutrino telescopes*, 1998.

[149] D. Heck, J. Knapp, J. N. Capdevielle, G. Schatz, and T. Thouw, *CORSIKA: A Monte Carlo Code to Simulate Extensive Air Showers*. Feb 1998.

[150] T. Antoni *et al.*, "KASCADE measurements of energy spectra for elemental groups of cosmic rays: Results and open problems," *Astropart. Phys.*, vol. 24, no. 1–2, pp. 1–25, 2005.

[151] R. Engel, "Test of hadronic interaction models with data from the pierre auger observatory," in *International Cosmic Ray Conference*, vol. 4 of *International Cosmic Ray Conference*, 2008.

[152] R. S. Fletcher, T. K. Gaisser, P. Lipari, and T. Stanev, "Siibyll: An event generator for simulation of high energy cosmic ray cascades," *Phys. Rev. D*, vol. 50, pp. 5710–5731, Nov 1994.

[153] J. Knapp, D. Heck, and G. Schatz, "Comparison of hadronic interaction models used in air shower simulations and of their influence on shower development and observables," Report 5828, FZKA, 1996.

[154] R. Glasstetter, "Analysis of electron and muon size spectra of eas," in *International Cosmic Ray Conference*, vol. 1, p. 222, 1999.

[155] T. Antoni *et al.*, "The cosmic-ray experiment KASCADE," *Nucl. Instrum. Meth. A*, vol. 513, no. 3, pp. 490–510, 2003.

[156] M. Honda, T. Kajita, K. Kasahara, S. Midorikawa, and T. Sanuki, “Calculation of atmospheric neutrino flux using the interaction model calibrated with atmospheric muon data,” *Phys. Rev. D*, vol. 75, p. 043006, Feb 2007.

[157] R. Enberg, M. Reno, and I. Sarcevic, “Prompt neutrino fluxes from atmospheric charm,” *Phys. Rev. D*, vol. 78, p. 043005, Aug 2008.

[158] `https://wiki.icecube.wisc.edu/index.php/Diplopia`. Accessed: 2013-06-17.

[159] J. Lundberg, P. Miocinovic, T. Burgess, J. Adams, S. Hundertmark, *et al.*, “Light tracking for glaciers and oceans: Scattering and absorption in heterogeneous media with photonics,” *Nucl. Instrum. Meth. A*, vol. 581, pp. 619–631, 2007.

[160] `https://wiki.icecube.wisc.edu/index.php/New_ice_model`. Accessed: 2013-06-17.

[161] D. Chirkin, “Study of south pole ice transparency with icecube flashers,” in *International Cosmic Ray Conference*, vol. 4 of *International Cosmic Ray Conference*, p. 161, 2011.

[162] `https://wiki.icecube.wisc.edu/index.php/Generating_Monopole_Photonics_Tables`. Accessed: 2013-06-17.

[163] `https://wiki.icecube.wisc.edu/index.php/Goodrunlist`. Accessed: 2013-06-14.

[164] D. Chirkin, “Feature extraction of icecube waveforms.” Internal Document.

[165] G. D’Agostini, “A multidimensional unfolding method based on bayes’ theorem,” *Nucl. Instrum. Meth. A*, vol. 362, no. 2-3, pp. 487–498, 1995.

[166] G. Cowan, “A survey of unfolding methods for particle physics,” in *Proc. Conf. on Advanced Statistical Techniques in Particle Physics* (M. Whalley and L. Lyons, eds.), pp. 248–257, 2002.

[167] `https://wiki.icecube.wisc.edu/index.php/Problem_DOMs`. Accessed: 2013-06-14.

[168] L. Gonick and W. Smith, *The Cartoon Guide to Statistics*. HarperCollins, 1993.

[169] G. C. Hill and K. Rawlins, “Unbiased cut selection for optimal upper limits in neutrino detectors: The model rejection potential technique,” *Astropart. Phys.*, vol. 19, no. 3, pp. 393–402, 2003.

[170] G. J. Feldman and R. D. Cousins, “Unified approach to the classical statistical analysis of small signals,” *Phys. Rev. D*, vol. 57, pp. 3873–3889, Apr 1998.

[171] G. D. Barr, T. K. Gaisser, P. Lipari, S. Robbins, and T. Stanev, “Three-dimensional calculation of atmospheric neutrinos,” *Phys. Rev. D*, vol. 70, p. 023006, Jul 2004.

[172] `https://wiki.icecube.wisc.edu/index.php/IC40_UHE_Diffuse_Analysis/Systematics`. Accessed: 2013-06-17.

[173] A. Schukraft and S. Schönen. Private Communication.

[174] M. G. Aartsen and oters, “First observation of pev-energy neutrinos with icecube,” *Phys. Rev. Lett.*, vol. 111, p. 021103, Jul 2013.

[175] `https://docushare.icecube.wisc.edu/dsweb/Get/Document-45978/IC40_BandwidthReport_April15.txt`. Accessed: 2013-06-17.

Acknowledgment

I would like to acknowledge the members of the astroparticle physics group at the Wuppertal University as well as the IceCube collaboration around the world. Their support and assistance has made this thesis possible. Of course, I can not mention all of them by name here. To those I forgot, I apologize in advance.

First and foremost, I want to thank my advisor Prof. Klaus Helbing, for giving me the opportunity to work for IceCube. He was also always open for my questions and offered many constructive hints and suggestions. Special thanks go to Timo Karg, who taught me the ropes of IceTray and always helped me with my physics or computer related troubles.

Among the members of the work group in Wuppertal I have to mention Anna Obertacke, Dennis Soldin and Sandro Kopper, with whom I shared an office. They made the working hours much more enjoyable and we had many fruitful discussions. Additionally, they read and corrected this thesis. Ms. Schaarwächter, our secretary, solved all organizational problems and was always a friendly help. I also have to thank those colleagues, past and present, who made Wuppertal more than a working place: Benjamin Semburg, Jan Auffenberg, Daniel Bindig, Tobias Fischer-Wasels and many more people I learned to know these past years.

Outside of Wuppertal, I particularly want to thank Henrike Wissing and Brian Christy from the IceCube collaboration. These two veterans of monopole searches helped to created the foundation for this work and their knowledge was a tremendous help. Henrike and Carlos de los Heros also review my analysis. Their critical questions helped to shape this work into its final form.

Last but not least, I would like to thank my parents, Franz and Marianne Posselt as well as my sisters Julia and Jennifer for their love and support. This thesis would not have been possible without them.

Selbständigkeitserklärung

Hiermit bestätige ich, diese Arbeit selbständig und nur unter Verwendung der angegebenen Quellen erstellt zu haben.

Wuppertal, im Oktober 2013 Jonas Posselt